UC Santa Barbara
UC Santa Barbara Previously Published Works

Title

Structural Evolution and Photoluminescence Quenching across the FASnI$_{1-x}$Br$_x$ (x = 0—3) Perovskites

Permalink

https://escholarship.org/uc/item/1qs920ph

Journal

Journal of the American Chemical Society, 146(23)

ISSN

0002-7863 1520-5126

Authors

Balvanz, Adam

Safdari, Majid

Zacharias, Marios

et al.

Publication Date

2024-05-30

DOI

10.1021/jacs.4c03669

Peer reviewed

Structural Evolution and Photoluminescence Quenching across the FASnI$_{3-x}$Br$_x$ (x = 0−3) Perovskites

Adam Balvanz, Majid Safdari,* Marios Zacharias, Daehan Kim, Claire Welton, Evan H. Oriel, Mikaël Kepenekian, Claudine Katan, Christos D. Malliakas, Jacky Even, Vladislav Klepov, G. N. Manjunatha Reddy, Richard D. Schaller, Lin X. Chen, Ram Seshadri, and Mercouri G. Kanatzidis*

ABSTRACT: One of the primary methods for band gap tuning in metal halide perovskites has been halide (I/Br) mixing. Despite widespread usage of this type of chemical substitution in perovskite photovoltaics, there is still little understanding of the structural impacts of halide alloying, with the assumption being the formation of ideal solid solutions. The FASnI$_{3-x}$Br$_x$ (x = 0−3) family of compounds provides the first example where the assumption breaks down, as the composition space is broken into two unique regimes (x = 0−2.9; x = 2.9−3) based on their average structure with the former having a 3D and the latter having an extended 3D (pseudo 0D) structure. Pair distribution function (PDF) analyses further suggest a dynamic $5s^2$ lone pair expression resulting in increasing levels of off-

centering of the central Sn as the Br concentration is increased. These antiferroelectric distortions indicate that even the x = 0−2.9 phase space behaves as a nonideal solid-solution on a more local scale. Solid-state NMR confirms the difference in local structure yielding greater insight into the chemical nature and local distributions of the FA$^+$ cation. In contrast to the FAPbI$_{3-x}$Br$_x$ series, a drastic photoluminescence (PL) quenching is observed with $x \geq 1.9$ compounds having no observable PL. Our detailed studies attribute this quenching to structural transitions induced by the distortions of the [SnBr$_6$] octahedra in response to stereochemically expressed lone pairs of electrons. This is confirmed through density functional theory, having a direct impact on the electronic structure.
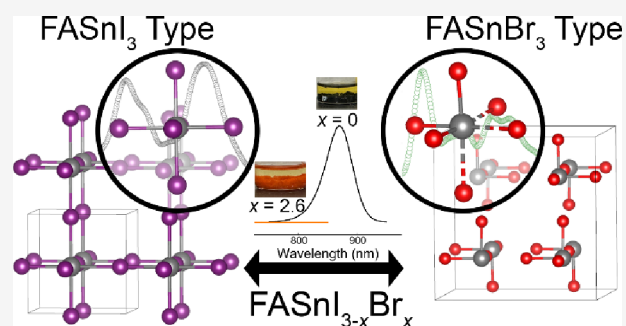
1. INTRODUCTION

Three-dimensional metal halide perovskites (MHPs) have been a major focus of ongoing research in the realm of photovoltaics (PV) due to their superior optoelectronic properties. These compounds are direct-gap, strong light-absorbing semiconductors with high carrier mobilities and high tolerance to defect states.[1−7] These favorable properties have allowed for a rapid improvement of perovskite-based PV, exceeding traditional Si-based devices in more recent years. Single junction perovskite solar cells (PSCs) first showed viability, achieving a power conversion efficiency (PCE) of ~11%[8,9] and has since rapidly improved,[10] achieving closer to the theoretical Shockley-Queisser limit (33.7%) with recent examples of single junction devices having >25% PCE.[11−14] Tuning the bandgap for Pb perovskites was successfully performed through the variation of the chemical composition, i.e., by I/Br and/or Pb/Sn mixing.[15−17] These new compositions across the mixed iodide-bromide phase space possess a well-behaved three-dimensional network leading to improved phase stability[18] and monumental efficiency improvements for related solar cells. This includes the mixed cation/halide perovskite used in 31.2% of perovskite/silicon

tandem devices.[19] Although there has been success with these phases, there are serious issues with the perovskite layer in a functional solar cell as the perovskite undergoes phase segregation under illumination due to halide migration.[20−22]

While the highest performing devices use lead (Pb) based halide perovskites and tandem cells use the mixed halide (I/Br) variant,[23−25] considerable effort has been made to create Pb-free PSCs due to Pb's toxicity.[26] One way of addressing these concerns is by using the ASnX$_3$ compositions. Sn^{2+} based materials have also shown success as light-absorbing layers, but the PCE lags behind only reaching ~14% for a single junction device: a considerable compromise in performance.[27] This can be attributed to a number of factors, including the instability of the Sn^{2+} oxidation state, making it more difficult to suppress the creation of performance-killing Sn^{4+} defect states. None-

theless, due to their structural versatility for compositional management and the existing knowledge of their Pb counterparts, Sn-based PSC are expected to improve in terms of stability and device performance as active research continues.[28−30]

In this vein, we need a holistic understanding of the structural complexities of hybrid mixed halide perovskites. We chose the representative family of compounds called $FASnI_{3−x}Br_x$ (where $x = 0−3$) because they have a remarkably broad range of band gap energies and exhibit structural complexity due to the diverse room temperature structures of $FASnI_3$ and $FASnBr_3$.[31,32] $FASnI_3$ crystallizes with a typical 3D perovskite framework with SnI_6 octahedra corner sharing in all directions and the FA^+ cation filling the central voids, counterbalancing the overall negative charge. $FASnBr_3$, on the other hand, has a structure that is atypical of MHPs based on increased expression of the Sn $5s^2$ lone pair, leading to significant off-centering. The compound deviates from the ideal 3D perovskite framework by lengthening three Sn − Br bonds and shortening the other three in the $SnBr_6$ octahedra in a coherent fashion, forming what can be thought of as more discrete pyramidal 0D $[SnBr_3]^−$ units. Since the orientation and arrangement of these molecular units in space retains the original undistorted architecture, the structure can still be thought of as a 3D perovskite type. The FA^+ cations then occupy positions within this "distorted cage" to balance the charge (Figure 1).
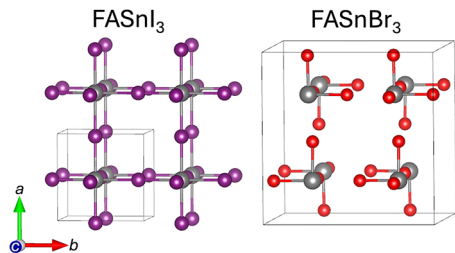
Figure 1. 3D inorganic framework of $FASnI_3$ (left) and the extended 3D framework of $FASnBr_3$ (right). The atoms are presented as gray, purple, and red for Sn, I, and Br, respectively. The FA^+ cations are omitted for simplicity. $FASnI_3$ and $FASnBr_3$ are modeled in $Pm\bar{3}m$ and $Pa\bar{3}$, respectively.

Here, we study the $FASnI_{3−x}Br_x$ ($x = 0−3$) chemical substitution range. Analysis of the average crystal structures shows a composition-dependence splitting the space into two unique regimes, apparently indicating nonidealistic behavior expected for a solid-solution. The $x = 0−2.9$ range adopts an average structure in line with the $FASnI_3$ structure type, and the $x = 2.9−3$ range takes on the $FASnBr_3$ room temperature structure with lower symmetry. However, inspection of the thermal displacement and lattice parameters suggests that the structure modification is already present at the local scale for $x < 2.9$. Single crystal X-ray diffraction analysis, thus, provides evidence for a more gradual structural evolution from the $FASnI_3$ to the $FASnBr_3$ structure type, initially exhibiting antiferroelectric distortions at the local scale that finally exhibits long-range ordering. We also find that careful control of the synthetic conditions is necessary to produce bulk crystallites with the desired I/Br ratio in the final product, as the typical synthetic procedures in hydrohalic acid solutions show a nonlinear behavior. Furthermore, halide substitution drastically impacts the photoluminescence (PL) as there is a

significant decrease in PL intensity with the introduction of Br. PL intensity decreases between $x = 0−1.1$, finally falling below the background with no observable emission present for $x \geq 1.9$. Further investigation revealed the above-mentioned systematic structural distortions as the most dominant source for PL quenching in high bromide compositions. The distortions provide a rationale for quenching of the photoluminescence with Br incorporation as the structure distorts and the $5s^2$ lone pair becomes more stereochemically expressed. This suggested mechanism is bolstered by room temperature Raman spectroscopy and pair distribution function (PDF) measurements which show unique scattering signatures and distance vectors for predominantly Br-rich molecular $[SnBr_{3−x}I_x]^−$ type units, and DFT calculations focusing on the activity of the Sn $5s^2$ lone pair of electrons. Solid state NMR also supports the difference in framework closely associated with the $Br^−$ concentration. Specifically, the FA^+ cation shows sharper signatures in the ^1H spectrum of Br-rich samples, meaning its motion has more fluidity. These findings are in contrast to PL behavior for the $APbI_{3−x}Br_x$ ($x = 0−3$; A = MA, FA) analogues, which show consistent PL response across the substitution range.[33,34] This study serves as a reminder that structural considerations in compositionally complex MHPs are paramount in understanding the behavior of the materials' performance for optoelectronic applications.

2. MATERIALS AND METHODS

2.1. General Synthetic Approach. Each of the compounds presented in this study was synthesized using solution-based crystal growth techniques in hydrohalic acid, which is a methodology that has been used on countless occasions by our research team to grow hybrid 3D and 2D phases alike.[7,31,35−37] The variant of the precipitation reaction used to synthesize materials in the $FASnI_{3−x}Br_x$ ($x = 0−3$) family was as follows: desired quantities of $SnCl_2 \cdot 2H_2O$ (Sima-Aldrich; 98 wt %) were dissolved in a solution comprised of hydroiodic (Sigma-Aldrich 57 wt % in H_2O), hydrobromic (Sigma-Aldrich; 48 wt % in H_2O), and hypophosphorous acids (Sigma-Aldrich; 50 wt % in H_2O) under constant stirring while on a hot plate set to ~120 °C (Table 1). The hypophosphorous acid was added as a

**Table 1. Experimental Conditions Used for Synthesis of the $FASnI_{3−x}Br_x$ Compounds[a]**

Compound	HI (vol.%)	HBr (vol.%)	Mol Fraction χ_{HBr}
$FASnI_3$	100	0	0
$FASnI_{2.6}Br_{0.4}$	66	34	0.38
$FASnI_{2.3}Br_{0.7}$	34	66	0.69
$FASnI_{2.1}Br_{0.9}$	25	75	0.78
$FASnI_{1.9}Br_{1.1}$	33	67	0.70
$FASnI_{1.1}Br_{1.9}$	17	83	0.85
$FASnI_{0.7}Br_{2.3}$	8	92	0.93
$FASnI_{0.4}Br_{2.6}$	7	93	0.94
$FASnI_{0.1}Br_{2.9}$	3	97	0.97
$FASnBr_3$	0	100	1

[a]The volume percentages are based on the ratio of the two hydrohalic acids added to the reaction solution not considering contributions from the hypophosphorous acid.

necessary reducing reagent utilized to suppress the oxidation of Sn^{2+} to Sn^{4+} as well as to prevent the conversion of $I^−$ to $[I_3]^{3−}$.[35] Once the solid was dissolved, desired amounts of formamidine acetate ($FACH_3COO$; TCI; > 98 wt %) were added to the hot reaction, followed immediately by the rapid crystallization of the desired perovskite phase, the persistence of which was dependent on the ratio of the hydrohalic acids (I-rich generally persisted longer than Br-rich).

The temperature of the hot plate was then increased to ∼210 °C while stirring continued until the solid dissolved and a clear solution was achieved. The reaction was then allowed to cool to room temperature, where the perovskite phase precipitated from the solution and could be extracted for further measurements.

In our experience, the perovskite phase needed to be extracted once the reaction reached room temperature. As the solid continued to remain in solution, halide exchange was observed with a darkening of the crystals over time. The color of the perovskite phase varied from black (iodide rich) to yellow (bromide rich) depending on the overall ratio of I/Br incorporation (Figure 2b). For more specific
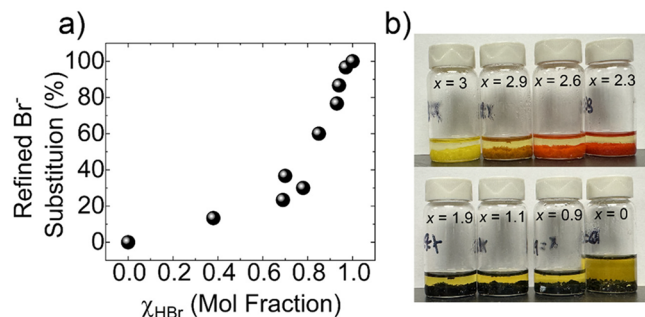
Figure 2. (a) Plot of the refined Br^- stoichiometry based on single crystal X-ray diffraction refinements against the mole fraction (χ_{Br}) of HBr present during the synthesis. Note that the mole fraction only relates the molar ratios of HI and HBr in the reaction solution. (b) Image of the bulk material for selected compositions.

synthetic details, the reader is referred to the Supporting Information for the synthesis conditions for each of the products. Since the samples were all susceptible to oxidation when removed from the mother liquor, the crystals were dried inside a nitrogen-filled glovebox or under a vacuum. Air-free powder diffraction patterns were collected to confirm the identity of the bulk material (Figure S1), and semiquantitative scanning electron microscopy coupled with energy dispersive X-ray spectroscopy (SEM-EDS) then confirmed the elemental composition (Table S5).

2.2. Powder X-ray Diffraction (PXRD). Dry crystallites were ground inside a N_2-filled glovebox with a mortar and pestle until a powder-like consistency was achieved. The powder was then packed into an 8 mm metallic mask with the usage of two polyimide layers of tape (one on both sides of the mask). The PXRD data were then collected at room temperature on a STOE-STADI-P powder diffractometer equipped with an asymmetric curved Germanium monochromator which uses Cu $K_{\alpha1}$ ($\lambda = 1.54056$ Å) radiation for diffraction and a MYTHEN2 1K DECTRIS one-dimensional silicon strip detector. The intensity data were collected within the range 5–60° 2θ. The instrument was first calibrated against a NIST Silicon standard (640d) prior to diffraction.

2.2.1. Single Crystal X-ray Diffraction Data for FASnI$_{3-x}$Br$_x$ (x = 0–3) Phases at Room Temperature. Single crystals within the FASnI$_{3-x}$Br$_x$ (x = 0–3) range were extracted from the mother liquor and immediately placed under Paratone-N oil on a glass slide to protect the surface from oxidation. The crystals were then transported to an optical microscope where suitable crystals were selected, cut to size, and mounted onto the goniometer head of a single crystal diffractometer for collection. An inert environment was maintained throughout the collections through the usage of a nitrogen blanket, which was sourced from the liquid, through an Oxford Cryosystems cryostat. This proved to be necessary in order to preserve the desired perovskite phase during diffraction as each of the samples was susceptible to oxidation with exposure to ambient conditions. Intensity data was then collected on either a STOE Stadi Vari diffractometer, which uses an AXO Ag K_α microfocus sealed X-ray A-MiXS source for diffraction ($\lambda = 0.560834$ Å) and a Dectris Platus3 R CdTe 300 K Hybrid Photon Counting Detector, or a XtaLAB Synergy diffractometer, equipped with a microfocus sealed X-ray tube

PhotonJet (Mo K_α: $\lambda = 0.71073$ Å) for diffraction and a Hybrid Pixel Array Detector (HyPix). The data collected on the Stadi Vari diffractometer was then reduced using the X-area software package (STOE). LANA[38] was used to perform a semiempirical absorption correction through outlier rejection and scaling of the reflections. The reduction for the data collected on the Synergy diffractometer was done within the CrysAlisPro software package (Rigaku) using an empirical absorption correction. For all of the room temperature data sets, the reflections were then imported into Olex2[39] where the data was solved using the intrinsic phrasing method as implemented in ShelXT[40] and further refined using least-squares on F^2 with ShelXL.[41] Selected crystallographic information and refinement statistics are presented in Table 2.

2.2.2. Low Temperature Single Crystal X-ray Diffraction. Low temperature diffraction experiments were conducted on freshly synthesized FASnI$_{1.9}$Br$_{1.1}$ and FASnI$_{0.4}$Br$_{2.6}$ crystals using the STOE Stadi Vari diffractometer discussed in the previous section. Measurements were conducted at various temperatures which were maintained through a flow of N_2 gas, obtained from the liquid, sustained by an Oxford Cryostream 700 plus cryostat. Data reduction was accomplished in the X-area software (STOE), using a semiempirical absorption correction, outlier rejection, and frame scaling as applied in LANA.[38] FASnI$_{0.4}$Br$_{2.6}$ showed a phase transition at 260 K and the low temperature structure was elucidated in Jana2006[42] due to increased disorder where a structural solution was achieved through SUPERFLIP[43] and refined using a least-squares method on F^2, as implemented in Jana2006.[42]

2.3. Modeling of Disorder in FASnI$_{0.1}$Br$_{2.9}$. In the refinement of FASnI$_{0.1}$Br$_{2.9}$ it was first apparent that a small fraction of iodide was introduced into the structure based on the color of the bulk material with respect to pure FASnBr$_3$ (Figure 2b/S2). Further evidence in support of iodide substitution came from both the small increase in the unit cell parameters with respect to FASnBr$_3$ and a measured redshift in the band gap of the material (Figure 9). When introducing I^- into the single crystal refinement, it became necessary to disorder the halide site. This was achieved by relaxing the positional constraints initially present which forced the Br^- and I^- to occupy the same atomic coordinates within the structure. With this applied constraint, the crystallographic refinement was unstable. However, after refining the two positions separately, the two halides were found to occupy different positions, stabilizing the refinement with a small fraction of I^-. Based on the observed shift in the band gap of the material as well as elemental confirmation of the presence of I^- from SEM-EDS, the disorder was kept in the final refinement.

2.4. Modeling of Disorder in FASnI$_{0.4}$Br$_{2.6}$ (260 K). During the refinement of the 260 K structure of FASnI$_{0.4}$Br$_{2.6}$, it became necessary to disorder the halide positions. The disorder was first realized with a non-negligible residual electron density in the vicinity of the initial halide position. Mixing the halide site (I/Br) and relaxing the constraints on the coordinates showed that I^- and Br^- occupied different average positions in the crystal lattice and proved to resolve the residual electron density near the halide site. Despite achieving a reasonable refinement with the above disorder, the model could prove to be inadequate to describe the true average structure of the material. Since the phase transition involves the elongation of 3 bonds in octahedra and a shortening of the remaining 3, induced twinning via different local variations of the transition could yield an average crystal structure with multiple disordered mixed I/Br positions. There can also be a convolution of the antiferroelectric (off-centering) and antiferrodistortive (tilting) distortions, adding additional complexity to the refinement and making a fully detailed refinement difficult. This type of disorder was further confirmed through room temperature pair distribution function (PDF) measurements.

2.5. Steady-State and Time-Resolved Photoluminescence (PL, TRPL). PL and TRPL spectra of the film samples were measured using an Edinburgh Instruments FS5 Spectrofluorometer. The samples were excited by ps pulsed diode laser. (375 nm excitation wavelength, pulse width of less than 100 ps and repetition rate 5 MHz). The spectra were corrected for the monochromator wavelength dependence and photomultiplier response functions provided

Table 2. Selected Crystallographic Information and Refinement Statistics for Representative FASnI$_{3-x}$Br$_x$ (x = 0–3) Compositions[a]

Formula	FASnI$_3$	FASnI$_{2.6}$Br$_{0.4}$	FASnI$_{2.3}$Br$_{0.7}$	FASnI$_{2.1}$Br$_{0.9}$	FASnI$_{1.9}$Br$_{1.1}$	FASnI$_{1.1}$Br$_{1.9}$	FASnI$_{0.7}$Br$_{2.3}$	FASnI$_{0.4}$Br$_{2.6}$	FASnI$_{0.1}$Br$_{2.9}$	FASnBr$_3$
Formula weight	525.41	518.74	508.41	495.72	488.67	452.02	432.28	418.19	402.62	398.45
Space group	$Pm\bar{3}m$	$Pm\bar{3}m$	$Pm\bar{3}m$	$Pm\bar{3}m$	$Pm\bar{3}m$	$Pm\bar{3}m$	$Pm\bar{3}m$	$Pm\bar{3}m$	$Pa\bar{3}$	$Pa\bar{3}$
a/b/c (Å)	6.3064(3)	6.3099(2)	6.2824(2)	6.2525(5)	6.2449(1)	6.1354(2)	6.0915(2)	6.0443(2)	12.0637(15)	12.0303(5)
Volume (Å^3)	250.81(4)	251.23(3)	247.96(2)	244.43(6)	243.54(1)	230.96(6)	226.03(2)	220.82(2)	1755.7(7)	1741.1(2)
Z	1	1	1	1	1	1	1	1	8	8
ρ_{calc} (g/cm^3)	3.479	3.429	3.405	3.368	3.332	3.250	3.176	3.145	3.046	3.040
Absorption coefficient (mm^{-1})	11.695	12.080	12.441	12.871	13.058	14.537	15.275	15.944	8.707	16.615
Independent reflections	91 [R$_{int}$ = 0.0375]	172 [R$_{int}$ = 0.0117]	166 [R$_{int}$ = 0.0087]	103 [R$_{int}$ = 0.0314]	160 [R$_{int}$ = 0.0183]	68 [R$_{int}$ = 0.0136]	95 [R$_{int}$ = 0.0136]	113 [R$_{int}$ = 0.0132]	688 [R$_{int}$ = 0.0487]	641 [R$_{int}$ = 0.0716]
Data/restraints/parameters	91/1/8	172/1/10	166/1/10	103/1/9	160/1/10	68/1/9	95/1/10	113/1/10	688/2/25	641/2/24
Final R indices [I > 2σ(I)]	R$_{obs}$ = 0.0435, wR$_{obs}$ = 0.01248	R$_{obs}$ = 0.0231, wR$_{obs}$ = 0.0766	R$_{obs}$ = 0.0239, wR$_{obs}$ = 0.0877	R$_{obs}$ = 0.0429, wR$_{obs}$ = 0.1006	R$_{obs}$ = 0.0292, wR$_{obs}$ = 0.0950	R$_{obs}$ = 0.0231, wR$_{obs}$ = 0.0846	R$_{obs}$ = 0.0317, wR$_{obs}$ = 0.1092	R$_{obs}$ = 0.0479, wR$_{obs}$ = 0.1540	R$_{obs}$ = 0.0585, wR$_{obs}$ = 0.1451	R$_{obs}$ = 0.0419, wR$_{obs}$ = 0.1011
Largest diff. peak/hole (e·Å^{-3})	0.869/−1.372	0.680/−0.836	1.229/−1.299	0.656/−0.944	0.814/−0.828	0.716/−0.4	0.636/−0.610	0.747/−1.260	0.952/−0.695	0.799/−0.643

[a]FASnI$_3$ and FASnBr$_3$ were synthesized and measured independently of previous research efforts. The full table can be found in Supporting Information Table S1.

by the manufacturer. Measurements were performed using dried polycrystalline powder samples and films. The measured TRPL decay ($I(t)$) of each sample was fitted by a three-exponent function, convoluted with the measured instrument response function. $(t) = \times e{-t/\tau i} + b$, τi and ai are the lifetime and amplitude of the different decay components, and b is the background level. The ratio of photons emitted by each component (Phi) can be calculated by $Phi = (ai \times \tau i)/(a1 \times \tau 1 + a2 \times \tau 2 + a3 \times \tau 3)$, $(i = 1,2,3)$, The average lifetime of each sample τavg is defined by $\tau avg = \sum Phi \times \tau i$.

2.6. Perovskite Film Preparation. The perovskite stock solutions were prepared by dissolving FAI, FABr, SnI$_2$ and SnBr$_2$ precursors with the target composition to form stoichiometric 0.8 M FASn(I$_{1-x}$Br$_x$)$_3$ in dimethylformamide (DMF)/dimethyl sulfoxide (DMSO) (3:2 volume ratio) mixed solvent. After the precursor was completely dissolved, the prepared solution was spin-coated on the substrate at 1000 rpm for 10 s and 4000 rpm for 30 s. Chlorobenzene was added as an antisolvent 25 s in the second step. Subsequently, the film was annealed at 100 °C for 10 min. To mitigate the effect of exposure to ambient conditions, PMMA was spin-coated on thin films to form the final encapsulation layer. All film preparation procedures were conducted in a N$_2$-filled glovebox. The light illumination study was conducted in the glovebox (Figure S11). The thin films were taken out of the glovebox for measurements after each period of illumination under 1sun.

2.7. Pair Distribution Function (PDF) of FASnI$_{3-x}$Br$_x$ (x = 0, 1.1, 2.6, 3). Freshly synthesized material was dried under vacuum and transferred to a nitrogen-filled glovebox. The dried crystallites were then ground in an agate mortar and pestle until a powder-like consistency was achieved. The powder was sieved to 53 μm particle sizes to ensure dense packing and then transferred to either a quartz or borosilicate capillary with outer diameter dimensions of 0.5 mm (purchased from Charles supper Co.) that was sealed at one end. Once packed, the capillary was sealed and transported to the diffractometer for measurement. Intensity data was collected using a STOE StadiVari diffractometer (detailed in the SXRD section) using 2-h exposure time per frame, collecting data from 1 to 160° 2θ (Ag K$_\alpha$) over five frames. Data was also collected for an empty capillary and air-scattering to establish a background effectively subtracting their scattering contributions. The images were imported into GSAS-II[44] where instrument parameters were calibrated against a LaB$_6$ standard collection at the same detector distance. Each frame was integrated as implemented in GSAS-II. The resulting diffraction pattern was exported and manually scaled. The 1D diffraction patterns were reduced to the $G(r)$ in PDFgetX3.[45] Further details are described in the Supporting Information.

2.8. Solid-State NMR spectroscopy. All NMR spectra were acquired on polycrystalline materials. Samples were separately packed into airtight zirconia rotors with an outer diameter of 1.3 mm fitted with VESPEL caps. Magic-Angle Spinning (MAS) NMR experiments were carried out at 18.8 T on a Bruker Avance Neo NMR spectrometer (the Larmor frequencies were ^{1}H = 800.1 MHz, and ^{119}Sn = 298.4 MHz, respectively) equipped with a 1.3 mm H-X double resonance probe head tuned to ^{1}H and ^{119}Sn configuration. Unless otherwise specified, all the samples were spun at a MAS frequency of 50 kHz using N$_2$ gas to prevent the moisture-induced degradation during the data acquisition. The 1D ^{119}Sn MAS NMR spectra were acquired using spin−echo pulse sequence, in which the echo delay was set to 20 μs corresponding to one rotor period. For pure FASnI$_3$ and FASnBr$_3$ compounds, the ^{119}Sn MAS NMR spectra were acquired by coadding 2048 transients. For FASnI$_{1.1}$Br$_{1.9}$ and FASnI$_{0.4}$Br$_{2.6}$ alloys, the 1D ^{119}Sn MAS NMR spectra were acquired by coadding 2048, using a recycle delay of 3 s ($T_1 \sim 1.4$ s). All 1D ^{1}H MAS NMR spectra were acquired by 32 coadded transients, whereby the recycle delay was set to 50 s, as determined from saturation recovery measurements and analyses. 2D ^{1}H−^{1}H spin diffusion NMR experiments were acquired using three-pulse noesy-like sequence with different mixing times (50, 200, and 500 ms) under fast MAS (55 kHz). A rotor-synchronized increment of 18.2 μs was applied to detect the indirect dimension using 400 t_1 increments, with 2 coadded transients, leading to an experimental time of ~11 h each. The ^{1}H

experimental shift was calibrated with respect to neat TMS using adamantane as an external reference (^{1}H resonance, 1.82 ppm). The experimental ^{119}Sn shifts were calibrated using liquid $SnCl_2$ as an external standard, according to IUPAC recommendation.[46] Data were processed from Bruker Topspin 4.1.4 inbuilt package.

2.9. FASnI$_{3-x}$Br$_x$ (x = 0, 1.1, 2.6, 3) Raman Spectroscopy. Selected materials were freshly synthesized using the experimental procedures detailed above and in the Supporting Information. The synthesized material was then removed from the solution, placed on a piece of filter paper to allow most of the solution to be absorbed and then quickly placed into a 9/7 mm (outer diameter/inner diameter) fused silica tube. The tube was placed under dynamic vacuum for ~24−48 h, allowing the remainder of the solution to evaporate off. These tubes were then sealed with an O_2/CH_4 torch (vacuum reaching ~10^{-2} mbar) and transported to a N_2 filled glovebox. The ampules were opened, and the material was extracted. The compounds were mechanically ground with an agate mortar and pestle and inserted into a quartz cuvette. The powder was more densely packed by adding glass wool, which was added to the cuvette on top of the powder. The top of the cuvette was sealed with epoxy to maintain an inert environment during the measurement. Once the epoxy was cured, the cuvettes were transferred into a plastic bag and vacuum sealed for transportation to the instrument. An example of the sample holders is shown in Figure S12. Raman scattering was collected on these samples using a 660 nm laser on low power settings to avoid laser-induced degradation. Raster scans were also utilized for the same purpose. Contributions from the background were then subtracted through a third-order polynomial fit function.

2.10. Computational Methods. All density functional theory (DFT) calculations were performed using the plane wave code Quantum ESPRESSO.[47,48] We employed optimized norm-conserving Vanderbilt pseudopotentials[49] and the Perdew−Burke−Ernzerhof revised for solids (PBEsol) functional.[50] We set the kinetic energy cutoff to 120 Ry and fixed the lattice constants of FASnI$_{3-x}$Br$_x$ for various x to the experimental values. To accommodate the Sn lone pairs in FASnI$_{3-x}$Br$_x$ we employed a $2 \times 2 \times 2$ supercell (96 atoms) of the idealized cubic unit cell consisting of 12 atoms [i.e., one formula unit (f.u.)]. This choice of supercell also allowed us to account for local disorder (or polymorphism)[51] in FASnI$_{3-x}$Br$_x$, both for the inorganic network and the FA molecules. We stress that employing a random distribution of locally distorted cells in static DFT calculations for halide perovskites has been shown to represent an accurate physical approach to describe the ultraslow structural dynamics, not captured by standard X-ray diffraction.[51,52] Here, accounting for structural disorder in FASnI$_3$ leads to a band gap opening at the R point of 0.38 eV (Figure S13b), alleviating the spurious semimetallic behavior calculated for its high-symmetry counterpart.[52] We further achieved randomly disordered structures of all FASnI$_{3-x}$Br$_x$ compositions via optimization of the nuclear coordinates, following the strategy described by *Zhao* et al.[52] In our simulations of FASnBr$_3$, we initially utilized the experimental crystal structure at room temperature, which exhibits the P$a\bar{3}$ space group. Notably, our DFT optimization of the FASnBr$_3$ structure to mimic structural disorder preserves the Sn lone pair expression, namely the initial average distortion as obtained from X-ray diffraction. For comparison purposes, we also generated idealized structures of FASnI$_3$ and FASnBr$_3$ by fixing the atoms of the inorganic network to their high symmetry P$m\bar{3}m$ positions and allow the FA$^+$ ions to relax. All geometry optimizations were performed using scalar relativistic pseudopotentials.

We employed the band structure unfolding technique to investigate the effect of electronic properties, computed with the inclusion of spin−orbit coupling, of the various compositions in the same Brillouin zone: the fundamental Brillouin zone of an idealized cubic unit cell. Band structure unfolding[53] was performed as implemented for plane waves and norm-conserving, fully relativistic pseudopotentials in the ZG module of the EPW code.[54,55] Fully relativistic electron spectral functions of FASnI$_{3-x}$Br$_x$ compounds were calculated for 300 **k**-points to ensure a correct mapping and dense sampling of the X-R-M-Γ path in the fundamental Brillouin zone of the idealized unit cell. Hole and electron effective masses at the R point were determined by finite differences.

3. RESULTS AND DISCUSSION

3.1. Synthetic Aspects. Each of the compounds was synthesized from hydrohalic acid mixtures (HI/HBr) by dissolving desired amounts of $SnCl_2 \bullet 2H_2O$ with FACH$_3$COO followed by cooling the reaction to promote crystallite growth, where the acids were intended to serve as a halide anion source for the perovskite formation. Based on these synthetic conditions necessary to sweep across the FASnI$_{3-x}$Br$_x$ (x = 0−3) composition space, it became clear that there was a strong preference for the incorporation of I$^-$ into the structure even with higher relative concentrations of Br$^-$ in the starting reaction solution.

This is most evident in the synthesis of FASnI$_{1.1}$Br$_{1.9}$, where the refined formula achieved a rough ratio of 2/1 (Br/I). However, during the synthesis, there was an overwhelming excess of Br$^-$ in the reaction solution (with a mole fraction χ_{HBr} = 0.85). Through experimental findings, it was discovered that only small volumes of hydroiodic acid solution were necessary to isolate materials with high Br$^-$ concentrations. This fact is supported by the difference in synthetic conditions between FASnI$_{0.4}$Br$_{2.6}$ and FASnI$_{0.1}$Br$_{2.9}$, which were synthesized with only a 0.03 difference in the HBr mole fraction. This relationship is seen when plotting the refined Br$^-$ stoichiometry against the mole fraction of HBr present during the synthesis (Figure 2a). At low HBr mole fractions χ_{HBr} (0−0.7), there is little change in the refined Br$^-$ stoichiometry, leading to a maximum of ~1/3 Br$^-$ substitution with a 0.7 HBr mole fraction. Within the range of 0.7−0.9 HBr, the Br$^-$ substitution increases an additional 1/3. The final 1/3 substitution is then achieved within a 0.1 HBr mole fraction window, making precise control over the acid volumes paramount to receiving the desired phases. Despite these limited concentration windows, homogeneous material with respect to composition was still obtained with single crystal measurements confirming a consistent composition and SEM-EDS providing a composition consistent with refined stoichiometries (Table S5) within the bounds of the semiquantitative nature of EDS measurements. 2D ^{1}H−^{1}H spin diffusion NMR further confirms I/Br intermixing in the bulk sample suggesting a consistent composition and a lack of phase separation.

During the crystallization process, two additional components play a significant role: the oxidation of Sn^{2+} to Sn^{4+} and the decomposition of formamidine to ammonia. These byproducts were observed in excessive amounts during longer crystallization times lasting for 6 h, with the crystals being cooled down at a rate of 7−10 °C/h. We detected the presence of two Sn^{4+} phases: SnI$_4$ and (NH$_4$)$_2$SnBr$_6$. These phases indicate the instability of the Sn^{2+} oxidation state as well as the FA$^+$ cation, which converted to NH$_4^+$ ions. For detailed information on the single crystal structure refinement parameters for these secondary phases, please refer to the Supporting Information (Table S6).

The level of halide mixing also impacted the crystal habit as seen in scanning electron microscopy images of the isolated crystals (Figure 3). FASnI$_3$ takes on a rhombic dodecahedral shape, typical of 3D hybrid halide perovskite materials. This morphology also agrees with the findings of previous studies of the material.[31] FASnBr$_3$, on the other hand, is a rod-like shape that can be generated by elongating the rhombic dodecahedron in a singular direction, creating a crystal shape with a
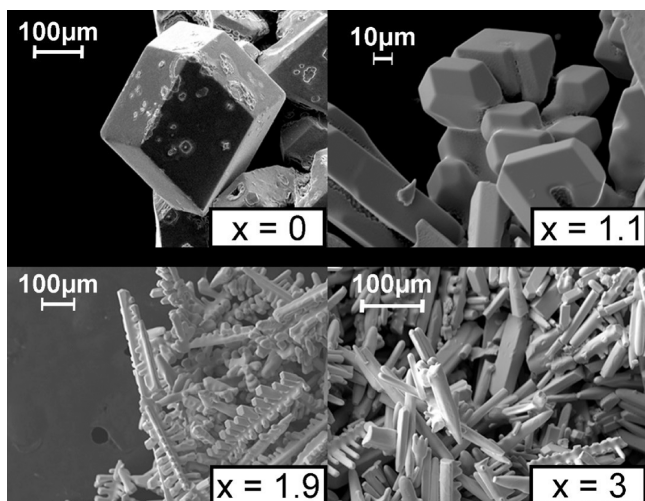
Figure 3. Scanning electron microscopy images of crystallites for selected compositions in the $FASnI_{3-x}Br_x$ ($x = 0-3$) substitution range, showing the typical crystal habit of the materials and their related morphology transition from iodide-rich composition to bromide-rich composition.

pyramidal-like cap at the end. Noticeably, the crystal habit of the $FASnI_{3-x}Br_x$ phases shows deviation along these lines with $FASnI_{1.9}Br_{1.1}$ having a morphology more closely resembling $FASnI_3$ whereas $FASnI_{1.1}Br_{1.9}$ crystallizes with an extended rhombic dodecahedral shape, more closely resembling $FASnBr_3$. SEM images on the remainder of the compositions confirm the trend in crystal morphology (Figure S3).

3.1.1. Structural Description and Phase Transitions. The end members of the present series $FASnI_3$ and $FASnBr_3$, have previously been structurally characterized through single crystal and Rietveld refinement in previous research efforts.[31,32] However, we revisit these two structures as they pertain to their solid solutions.

3.1.2. Structural Description of $FASnI_3$. When considering only the crystallographic aspects of $FASnI_3$, the compound is best described by a cubic structure (space group $Pm\overline{3}m$) adopting the ideal perovskite architecture with SnI_6 octahedra corner sharing in all three crystallographic directions, forming a cage with $180°$ Sn — I — Sn angles. The FA^+ cation then sits in the center of the cage to balance the overall negative charge of the framework. This organic cation, though, is heavily disordered, intended to represent the dynamic nature of the position of the cation (tumbling). Based on the symmetrical constraints of the space group, the disorder generates a pseudo carbon-centered "octahedra" where the caps are 1/3 occupied N atoms. This type of model is an approximation to the rotation where the molecule which creates a "sphere" of electron density surrounding the central carbon atom. This model, however, does not abide by traditional chemical understanding since the structure of the organic FA^+ cation is not considered. Alternatively, since FA^+ has a net dipole moment that cannot be canceled out (as might be suggested by the $Pm\overline{3}m$ model) the symmetry can be reduced to noncentrosymmetric ($Amm2$), allowing for ordering the FA^+ cations. This symmetry setting is artificial, however, so the cubic model ($Pm\overline{3}m$) will be considered in further discussions.

It should be noted that $FASnI_3$ (as well as $MASnI_3$) undergoes a smooth phase transition at low temperatures characterized in calorimetric measurements by weak endother-

mic peaks and a long tail at the lower temperature.[32] This behavior in Pb-based compounds is commonly associated with antiferrodistortive instabilities on cooling from elevated temperatures, which result in the transition to tetragonal or orthorhombic structures at lower temperatures. From the symmetry viewpoint, these antiferrodistortive and nonpolar instabilities are characterized by the M_3^+ and R_4^+ irreducible representations of the $Pm\overline{3}m$ parent phase.[56] These order parameters are attributed by symmetry to octahedra rotations at the microscopic level. They are indeed associated experimentally to anisotropic thermal motions with large amplitudes of the halide atoms perpendicular to the metal halide bonds,[57] and diffuse scattering rods along the M-R lines in reciprocal space.[58] The slow dynamics related to these strongly anharmonic octahedra rotations is difficult to capture precisely by diffraction techniques. It led to the proposition of the polymorphous picture for the high temperature $Pm\overline{3}m$ cubic phase, leading to some improvement for the refinement of pair distribution functions (PDF).[51]

3.1.3. Structural Description of $FASnBr_3$. The structure of $FASnBr_3$ has been resolved from high quality Rietveld refinement previously.[32] However, since our work presents the first single crystal study, we shall endeavor to describe its structure in this section as it is key to understanding structural alterations in $FASnI_{3-x}Br_x$ ($x = 0-3$) phases and drastic deviations in optical properties of these materials. Unlike $FASnI_3$ the bromide analogue shows increased stereochemical expression of its $5s^2$ loan pair of electrons, which "breaks" the cage framework in an ordered fashion (Figure 4a). Three of
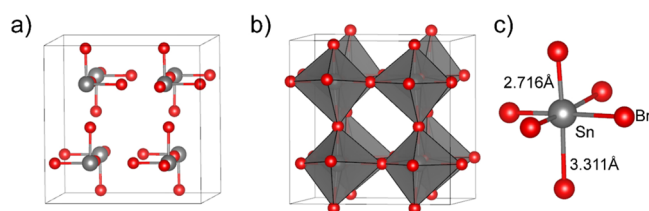
Figure 4. Depiction of the $FASnBr_3$ structure ($Pa\overline{3}$) in three panels. (a) Overall structure with FA^+ cations omitted for simplicity and (b) same view with polyhedra and elongated bonds included to show how the perovskite framework is retained. (c) Sn center with the unique bond distances highlighted. The atoms are presented as gray and red for Sn and Br, respectively.

the 6 bonds in the $SnBr_6$ octahedra extend, creating a set of 3 short 2.716(1) Å bonds and 3 long 3.311(1) Å distances (Figure 4c). This perturbation in the perovskite structure creates what can be thought of as $[SnBr_3]^-$ molecular units (pyramidal geometry) that are charged balanced with FA^+ cations. However, this view is a simplification used here for clarity as the 3.311(1) Å Sn — Br bonds undoubtedly retain bonding-type interactions. The geometric constraints placed on the framework by the size of FA^+ are of equal consideration. Being the largest A-site cage cation typically seen in MHP materials, the Sn−Br framework presents the geometric limit for the FA^+ cation before the perovskite cage becomes unstable.[59] This $[MX_3]^-$ type unit is not unprecedented in the perovskite ABX_3 stoichiometry as the compounds $RbGeBr_3$,[60] $CsGeX_3$ (X = Cl, Br, I),[61] $MAGeI_3$,[62,63] $FAGeI_3$,[63] $FAGe_{0.5}Sn_{0.5}Br_3$,[64] $MAGeBr_3$,[64] $FA_{0.5}MA_{0.5}GeBr_3$,[64] $FAGeBr_3$,[64] $N(CH_3)_4GeCl_3$,[65] $(CH_3)_2NH_2SnBr_3$,[66] $(CH_3)_3NH_2SnBr_3$,[67] $NH(CH_3)_3SnBr_3$,[68] $NH(CH_3)_3SnCl_3$,[68] $C(NH_2)_3SnCl_3$[69] and $MASnCl_3$[70] display the same "pyramidal"

Table 3. List of Compounds That Have $[MX_3]^-$ 0D Molecular Units with an AMX_3 Perovskite Stoichiometry and an Extended 3D Architecture[a]

Formula	Temperature (K)	Band Gap (eV)	Photoluminescence[b]	Reference
$CsGeI_3$	293	1.6	N/A	61
$MAGeI_3$	293	1.9	N	62, 63
$FAGeI_3$	293	2.2	N	63
$CsGeBr_3$	293	2.42	Y	61, 64
$RbGeBr_3$	293	N/A	N/A	60
$MAGeBr_3$	298	2.91	N	64
$FA_{0.5}MA_{0.5}GeBr_3$	298	3.02	N	64
$FAGeBr_3$	298	3.13	N	64
$CsGeCl_3$	293	3.69	N/A	61
$N(CH_3)_4GeCl_3$	293	N/A	N/A	65
$FAGe_{0.5}Sn_{0.5}Br_3$	298	2.75	N	64
$FASnI_{0.4}Br_{2.6}$	260	N/A	N/A	This Work
$FASnBr_{2.9}I_{0.1}$	300	2.05	N	This Work
$FASnBr_3$	290	2.24	N	This Work, 74
$(CH_3)_2NH_2SnBr_3$	293	N/A	N/A	66
$(CH_3)_3NH_2SnBr_3$	293	N/A	N/A	67
$NH(CH_3)_3SnBr_3$	296	2.76	N/A	68
$NH(CH_3)_3SnCl_3$	296	3.59	N/A	68
$C(NH_2)_3SnCl_3$	295	N/A	N/A	69
$MASnCl_3$	297	3.46	N/A	70, 75

[a]Relevant optical properties of each material are also listed. [b]Photoluminescence is given a Y if the property was observed, a N if it was not, and a N/A if not reported.

geometry (Table 3). Therefore, $FASnBr_3$ is more accurately described as an extended 3D framework (pseudo 0D) at room temperature by considering 0D pyramidal $[SnBr_3]^-$ units more weakly interacting and arranging in the 3D perovskite architecture (Figure 4b). The lone pair-induced structural distortion, which can also be viewed as a second-order antiferroelectric Jahn−Teller distortion reduces the dimensionality of the 3D network, moving it closer to 0D. Furthermore, this is supported by theoretical studies which probed the limit of the perovskite framework in the $FAPb_{1-x}Sn_xBr_3$ composition space suggesting the dynamic presence of these distortions.[59] The pseudodimensional reduction also has a direct impact on the symmetry of the compounds, as it crystallizes in the lower symmetry space group $Pa\bar{3}$ resulting in a 2-fold expansion of the unit cell parameters which can easily be seen in the precession images of reciprocal space (Figure S4). The distortion showed by $FASnBr_3$ can be alleviated by increasing the temperature whereby the typical 3D perovskite framework is obtained above 312 K,[32] which in agreement with an analogous phase transition exhibited by the $CsGeX_3$ (X = Cl, Br, I) compositions.

From the symmetry viewpoint, the structural phase transition from the high-temperature $Pm\bar{3}m$ structure to the room-temperature $Pa\bar{3}$ structure is completely different from the nonpolar and antiferrodistortive instabilities attributed to M_3^+ and R_4^+ order parameters seen for the low temperature transitions of $FASnI_3$. The symmetry analysis of the $Pm\bar{3}m/Pa\bar{3}$ group-subgroup relationship reveals that the structural instability is mainly driven by an X_5^- order parameter. Group symmetry thus predicts a polar instability related to the creation of an antiferroelectric array at room temperature. The antiferroelectric pattern is expected to exhibit phase factors for the atomic motions related to the wavevector $\vec{k}_X$. Among the three atomic sites (A,B,X) usually defining the regular ABX_3 cubic perovskite lattice at high temperature, the A site (FA^+) is not affected by the X_5^- structural instability. In contrast, both

the B site (Sn) and the X site (Br) are expected to undergo atomic axial displacement patterns. This feature is in perfect agreement with the reported experimental structure. The condensation at T = 312 K of the X_5^- structural instability in $FASnBr_3$ has a calorimetric signature, which is also completely different from the signature of the antiferrodistortive instability in $FASnI_3$.[32] As expected, the thermal motions obtained from X-ray diffraction also exhibit new features for $FASnBr_3$ (*vide infra*). Therefore, a competition between polar and nonpolar structural instabilities is expected, something commonly observed in perovskite lattices.[71] Experimentally, a complex superposition of structural signatures of different origins is indeed observed (*vide infra*).

3.1.4. Discrepancy between $CsSnBr_3$ and $FASnBr_3$. Besides being fully inorganic and hybrid, respectively, $CsSnBr_3$ and $FASnBr_3$ structurally vary from one another at room temperature. $CsSnBr_3$ retains a 3D perovskite framework and expected $Pm\bar{3}m$ space group symmetry, while $FASnBr_3$ distorts reducing the symmetry to $Pa\bar{3}$. This difference can be attributed to the difference in "pressure" exerted by the A-site cation on the inorganic framework. Based on the geometric size, FA^+ within a Sn − Br perovskite framework represents the limit with respect to the tolerance of the perovskite lattice, i.e., the FA^+ cation is too large at room temperature (253 pm).[72] This is reconciled with $FASnBr_3$ generating a perovskite framework at higher temperatures whereby the basic cell and cage can expand to more easily accommodate the larger organic. Cs^+, on the other hand, typically represents the other end of the tolerance spectrum for halide perovskite templating A-site cations (184 pm).[73] Therefore, it can more comfortably template a Sn − Br based perovskite. These structural variations highlight the strict size limitations for perovskite forming compositions.

3.1.5. Synthetic Insights Garnered from Structure. The structural differences between the two end-member materials might also give insight into the synthetic conditions necessary
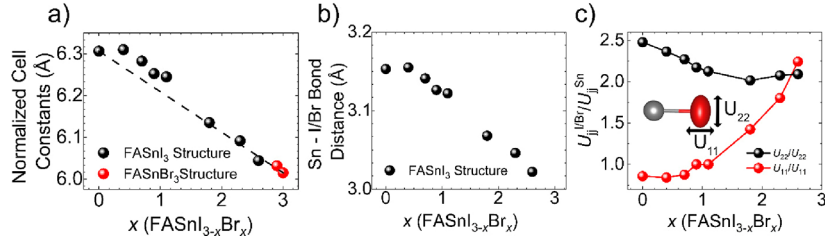
Figure 5. (a) Normalized unit cell constants, based on single crystal X-ray diffraction data, for each compound synthesized in the $FASnI_{3-x}Br_x$ ($x = 0-3$) system. Compounds are labeled by their structure type in black and red for the $FASnI_3$ ($Pm\overline{3}m$) and $FASnBr_3$ ($Pa\overline{3}$) structure type, respectively. The dashed line displays the ideal behavior based on Vegard's Law analysis. (b) Bond distances for each compound with the $FASnI_3$ structure plotted against composition. (c) Plot of the U_{11} (red) and U_{22} (black) anisotropic displacement parameters as a function of composition normalized to the displacement parameters of the central Sn considering the same direction for all $FASnI_{3-x}Br_x$ compounds that retain the $FASnI_3$ cubic structure. Note that the U_{22} and the U_{33} parameters are equivalent for both the halide and metal atoms.

for synthesizing the $FASnI_{3-x}Br_x$ ($x = 0-3$). As mentioned in the synthetic portion of the discussion, to achieve a material with 2/3 Br^- substitution or greater ($x = 2-3$) the mole fraction of hydrobromic acid (χ_{HBr}) must be >0.9. The pronounced inclination toward I^- during the synthesis process aligns well with the underlying structure. Given that $FASnBr_3$ possesses more "discrete" $[SnBr_3]^-$ pyramidal units, it essentially functions more like a molecular salt, represented as $(FA^+)([SnBr_3]^-)$, and is associated with a comparatively weaker lattice structure. This makes $FASnBr_3$ more soluble in the polar acidic media employed during the synthesis. In contrast, $FASnI_3$ features a 3D network of robustly interconnected corner-sharing SnI_6 octahedra, resulting in diminished solubility in polar solvents when compared to $FASnBr_3$. Therefore, bromide-rich compositions tend to have higher solubility than their iodide-rich counterparts. Such differential solubilities cause compositions with a higher iodide content to precipitate more easily from the solution. It also supports the idea of halide exchange (iodide for bromide) if exposure to the mother liquor is prolonged since, from a solubility perspective, precipitation of I-rich phases is more favorable.

3.1.6. Structural Description of the FASnBr₃ (x = 0−3) Compositions. Upon the introduction of Br^- into the structure, there is a corresponding decrease in the unit cell parameters of the cubic structure (denoted as $FASnI_3$ structure type) following Vegard's Law (Figure 5a). The variations of the standard lattice parameters do not exhibit discontinuities that might attributed to a sudden crossover from a lattice dominated by fluctuations of the octahedra tilts (M_3^+/R_4^+, $FASnI_{3-}$ like) to a lattice dominated by atomic translations related to antiferroelectric fluctuations (X_5^-, $FASnBr_{3-}$ like). The average $FASnI_3$ structure type was retained for the refinements of the $FASnI_{3-x}Br_x$ ($x = 0-2.9$) structures leading to Br^- substituted on the I^- site and having the same atomic coordinates. Therefore, for these intermediate compositions, the distribution of local static disorder is artificially represented in the refined crystallographic structures through the thermal displacement tensor U_{ij} and is entangled with contributions related to thermal (phonon) displacements.

The inspection of the anisotropic displacement parameters nevertheless allows for the characterization of the interplay between the various (M_3^+/R_4^+ versus X_5^-) structural fluctuations. From Figure 5c, we first observe that the U_{22} and U_{33} anisotropic displacement parameters are very strong in $FASnI_3$ and mainly reflect antiferrodistortive fluctuations related to octahedra rotations. The thermal displacement

parameter U_{11} related to axial displacements (stretching of the Sn−I bonds) is smaller by comparison. When the Br content increases, the most noticeable difference is the elongation of the U_{11} thermal displacement parameters from 36(1) to 148(4) Å²x10³ for $FASnI_3$ and $FASnI_{0.4}Br_{2.6}$ respectively. A very strong increase of the U_{11} parameter is observed for $x > 1$ leading to a maximum value for $FASnI_{0.4}Br_{2.6}$. The steep increase for intermediate compositions can be partially attributed to the difference in average bond length between Sn − Br and Sn − I and the structural differences between $FASnI_3$ and $FASnBr_3$. As the Br^- increases, the number of $[SnBr_3]^-$ and $[SnIBr_2]^-$ units also increase. This leads to a shortening in the bond lengths for regions with this motif and respective lengthening of interunit distances. In contrast, the $[SnBr_3]^-$ and $[SnI_2Br]^-$ units present in the structure prefer shorter interunit distances with small or negligible differences between intraunit Sn−I and interunit Sn−I bonds, thereby forming the connected 3D framework, requiring much longer interatomic distances. This then leads to the apparent elongation of the anisotropic displacement parameter of the halide sites for the Br^- rich compositions in the cases where the two different halide positions cannot be resolved. This hypothesis is confirmed through low temperature single crystal X-ray diffraction, and room temperature pair distribution function (PDF)/Raman spectroscopy *vide infra*. The suggestion is also in line with theoretical findings in the $FAPb_{1-x}Sn_xBr_3$ composition space, which suggest that the off-centering through the lengthening and shortening of bonds is expected to be present up until reaching the Pb-rich regime at which point equalization occurs at $FAPb_{0.5}Sn_{0.5}Br_3$.[59] The distribution of local static disorder in intermediate compositions is entangled in U_{11} with the contributions related to thermal (phonon) displacements. Both reflect the propensity of the perovskite lattice to undergo locally X_5^- structural distortions. It should be noted that the refinements of the average crystallographic structures lead to a clear $Pa\overline{3}$ space group only for very high Br^- contents. This is expected when the correlation lengths related to the X_5^- fluctuations diverge and when the associated diffuse scattering contributions merge into new Bragg-like contributions that can be included in a structure refinement within the $Pa\overline{3}$ space group. It may be further noticed (Figure 5c) that the values of the U_{22} and U_{33} anisotropic displacement parameters are only slightly reduced when increasing the Br content by comparison to pure $FASnI_3$. It suggests that antiferrodistorsive fluctuations are still present whatever the Br content, even when antiferroelectric fluctuations start to dominate.

While most of the $FASnI_{3-x}Br_x$ ($x = 0-3$) series retains, on average, the structure of $FASnI_3$ when $x = 2.9$ the structure more clearly shifts toward the $FASnBr_3$ motif but with noticeable differences. $FASnI_{0.1}Br_{2.9}$ crystallizes in the same $Pa\overline{3}$ space group as $FASnBr_3$ with a 2-fold enlargement of the cell in all three directions; however, the halides are positionally disordered with respect to one another, with the Br and I having independent atomic coordinates (Figure 6a). The
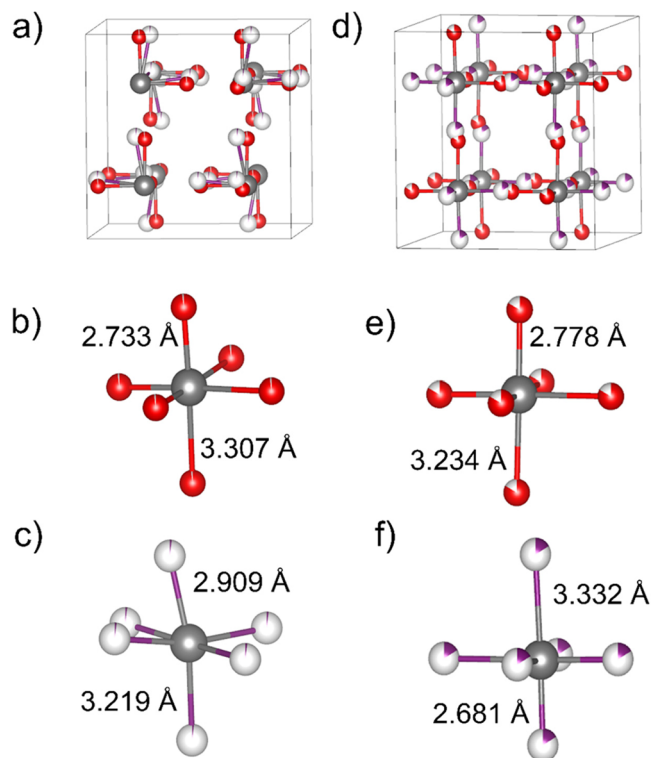
Figure 6. (a) Depiction of the overall structure of $FASnI_{0.1}Br_{2.9}$ with the organic FA^+ cations omitted. (b,c) Closer look at the Sn coordination sphere to (b) Br^- and (c) I^- for $FASnI_{0.1}Br_{2.9}$. (d) Overall structure of $FASnI_{0.4}Br_{2.6}$ at 260 K with the organic cations omitted. (e,f) Closer view of the (e) short and (f) long Sn−X distances in $FASnI_{0.4}Br_{2.6}$ at 260 K. Both are molded in the $Pa\overline{3}$ space group.

disorder allows the small amounts of I^- present to modulate its distance from the Sn center. The covalently bonded I atoms obtain a longer bond (2.91(6) Å) compared to an equivalent Br atom (2.733(2) Å) whereas the more noncovalent I atom achieves a shorter distance (3.22(5) Å) than the equivalent Br atom (3.307(3) Å) which is consistent with the I atoms attempting to establish a more stable 3D framework compared to the Br atoms, which are stabilized in an extended coordination environment (Figure 6b and 6c).

3.1.7. Temperature-Dependent Phase Transitions. To further investigate the presence of a 3D-0D phase transition, low temperature single crystal X-ray diffraction experiments were conducted on two members of the $FASnI_{3-x}Br_x$ ($x = 0-3$) substitution range, specifically focusing on I-rich and Br-rich compounds that retained the $FASnI_3$ 3D structure at room temperature. Therefore, $FASnI_{1.9}Br_{1.1}$ and $FASnI_{0.4}Br_{2.6}$, were selected as representative candidates. Upon cooling, FAS-nI_{1.9}Br_{1.1} did not display the anticipated phase change; however, at ~260 K the hypothesized 3D-0D transition was observed for $FASnI_{0.4}Br_{2.6}$, marked by additional reflections in

reciprocal space (Figure S10). The resolved structure resembles the room temperature structure $FASnI_{0.1}Br_{2.9}$ with disordered halide positions, but with unique differences (Figure 6d). The best crystallographic model was obtained by relaxing the constraints on the coordinates of I and Br, refining them independently. As a result, the I and Br occupy different positions with two unique interatomic distances to each Sn center each: one bonding (Figure 6e) and one nonbonding distance (Figure 6f). The "bonding" distances are 2.681 and 2.778 Å for Sn − I and Sn − Br, respectively and the "non-bonding" distances are 3.332 and 3.234 Å for Sn − I and Sn − Br, respectively. This places the iodide atoms within bonding distance closer than the bromide and on the opposite side of the octahedra. Note that while these distances are referred to as "bonding" and "non-bonding," the longer distances are expected to have a bonding character, albeit they are much weaker.

While this model achieves reasonable agreement statistics, increased levels of disorder could be present that is not accounted for (see section 2.4). Nonetheless, the presence of the $Pm\overline{3}m/Pa\overline{3}$ structural transition at low temperatures is related to the condensation of the X_5^- structure fluctuations observed at room temperature through the U_{11} parameter (Figure 5c). It confirms that the trend in the room temperature thermal parameters can be attributed to an increased presence of off-centering locally while retaining a 3D framework on average and provides a rationale for observed PL quenching, *vide infra*, as these distortions have already been shown to drastically decrease PL intensity in $MAGeI_3$.[62] Further information on 260 K structure of $FASnI_{0.4}Br_{2.6}$ can be found in the Supporting Information. By conducting additional experiments using temperature-dependent UV−vis spectroscopy, we can further validate the existence of the phase transition. This confirmation would be evident through the sudden widening of the band gap once the transition temperature is reached on cooling.

3.2. Analyses of the Local Structures for $FASnI_{3-x}Br_x$ ($x = 0, 1.1, 2.6, 3$) Compositions: Pair Distribution Function (PDF). To garner a more in-depth understanding of the local structural distortions of the inorganic framework within the mixed halide phases, experimental PDF curves were generated from high-resolution X-ray powder diffraction patterns using equations S1 − S4. Four compositions were selected: $FASnI_3$ and $FASnBr_3$, to obtain a baseline PDF curve for the two unique structure types, as well as $FASnI_{1.9}Br_{1.1}$ and $FASnI_{0.4}Br_{2.6}$ since these compositions were tested for temperature-dependent phase transitions through single crystal X-ray diffraction.

Experimental PDF curves provide information on the density of atoms present at a distance r (Å) away from an arbitrary center. Based on the average crystal structure for $FASnI_3$ the local structure of 3D Sn MHP inorganic framework contains two main components consisting of primary distance vectors of ~3 and 4.5 Å for Sn − I bonding and I − I nearest neighbors. On the other hand, due to the distortions of the perovskite lattice at room temperature, $FASnBr_3$ contains two unique Sn − Br distances at 2.7 and 3.3 Å and a broader distribution of nearest neighbor Br − Br vectors providing contrast between the two structure types that can be identified in the $G(r)$. Therefore, examination of the low r regions (2−5 Å) of the PDF curves indicates a distribution of distortions with short coherence lengths. A more extended range of the calculated $G(r)$, however, can be seen in Figure S5

As expected, the experimental PDF of FASnI$_3$ (Figure 7a) has a strong feature centered at ~3 Å. This vector corresponds
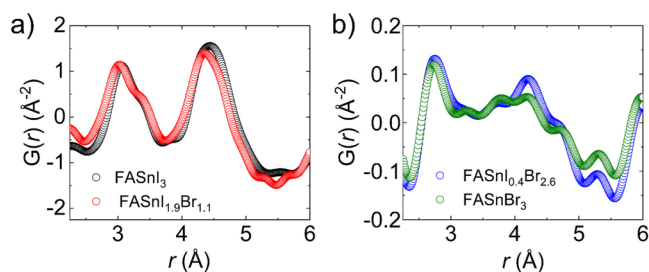

Figure 7. Experimental pair distribution function curves ($G(r)$) for a) FASnI$_3$ (black) and FASnI$_{1.9}$Br$_{1.1}$ (red) and b) FASnI$_{0.4}$Br$_{2.6}$ (blue) and FASnBr$_3$ (green) with the range of 2–6 Å.

to the Sn − I bond in the FASnI$_3$ structure, which deviates ~0.1 Å from the distance obtained from the average crystal structure (3.15 Å). However, the position of the peak is consistent with the previous experimental PDF conducted on the same phase.[76] There is, however, identifiable shouldering toward higher r, which could provide evidence for emphanitic behavior: a phenomenon previously identified in the MHP literature[77] despite having roots in chalcogenide chemistry.[78−80] The experimental PDF also contains a feature centered at 4.5 Å, in line with I − I nearest neighbor distance vectors. Refining the local structure of FASnI$_3$ by fitting the

experimental PDF within the 2–5 Å range shows a reasonable agreement as well as small distortions of the SnI$_6$ octahedra: off-centering the Sn atom presumably due to activity of the $5s^2$ lone pair (Figure S6). Thus, weak structural fluctuations of the X$_5^-$ type are probably already present in pure FASnI$_3$ structure.

FASnBr$_3$, on the other hand, shows a much broader distribution of distance vectors within the 2.5–5 Å region (Figure 7b), suggesting higher degrees of local dynamicity in the Sn − Br bond length as well as other vectors. A sharp feature centering at ~2.7 Å is in excellent agreement with the short, bonding Sn − Br distance. Additionally, broader features at 3.18 and 3.42 Å can be attributed to the long Sn − Br distances in the 0D unit because the average between the two is 3.3 Å. The presence of a split distance vector indicates a higher degree of dynamicity in the 3.311 Å. Broad features in the $G(r)$ between 4 and 5 Å reflect the fluidity in the nearest neighbor Br − Br distance vectors. The fitting of the experimental PDF curve at low r shows that the average crystal structure aligns with the local structure (Figure S7). The curve is also consistent with previous experimental data collected for FASnBr$_3$, though our local structure explanation differs significantly since here P$a\bar{3}$ model was used as the basis structure instead of P$m\bar{3}m$.[81]

Comparisons of the mixed halide PDF curves with the end members show a remarkable trend in the short-range structure of these mixed halide phases. The PDF of FASnI$_{1.9}$Br$_{1.1}$ resembles that of FASnI$_3$ with a well-resolved peak in the
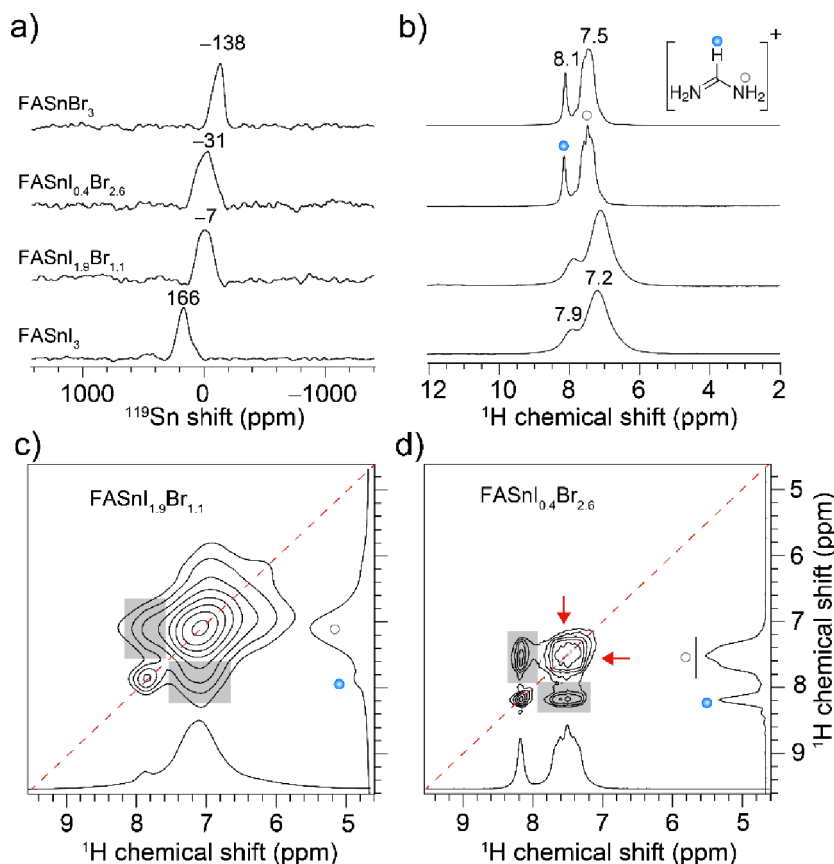
Figure 8. Solid-state 1D (a) ^{119}Sn and (b) ^{1}H magic-angle spinning NMR spectra of FASnX$_3$ alloys as indicated. Solid-state 2D ^{1}H−^{1}H spin-diffusion (SD) NMR spectra of (c) FASnI$_{1.9}$Br$_{1.1}$ and (d) FASnI$_{0.4}$Br$_{2.6}$ phases plotted with the sky-line projections presented on horizontal and vertical axes in the insets. All spectra were acquired at 18.8 T (^{1}H = 800.1 MHz and ^{119}Sn = 298.4 MHz), 50 kHz (a,b) or 55 kHz (c,d) MAS and at room temperature.

curve at ~3 Å (Figure 7a). Splitting of both the bonding and nearest neighbor halide peaks indicates local discrepancy of these distances, likely associated with mixed I/Br on the halide position. On the other end of the substitution range, $FASnI_{0.4}Br_{2.6}$ displays a curve most similar to that of $FASnBr_3$ despite the average crystal structure being consistent with $FASnI_3$. Furthermore, the PDF of this Br-rich phase shows a prominent distance vector at the same 2.7 Å corresponding to the short distance in a $[SnBr_3]$ 0D unit (Figure 7b). The presence of this distance vector indicates a dynamic competition between the concealment and expression of the $5s^2$ lone pair of electrons a local level that is not captured in the average crystal structure, with the exception of the elongation of the displacement parameters. Attempts to model the experimental PDF curves for these mixed halide phases using supercell approximations to the halide substitutions and Reverse Monte Carlo simulations could yield a more in-depth understanding of this competition. Such modeling, however, is outside the scope of the current work. The definitive presence of significant Sn off-centering in the short-range does explain the trends in the optical properties of the bulk materials.

3.3. Solid State ^{119}Sn and ^{1}H NMR Studies on $FASnI_{3-x}Br_x$ (x = 0, 1.1, 2.6 3).
Solid-state NMR spectroscopy can analyze local chemical environments of organic cations in the cuboctahedral cages and organic–inorganic interfaces, which does not require long-range order.[82−85] Figure 8 presents ^{119}Sn and ^{1}H spectra of pure phases and alloys. For example, ^{119}Sn shifts are sensitive to the oxidation state of the Sn atoms, Sn − X bond distances, Sn−X−Sn bond angles and octahedral distortions. The octahedral Sn atoms in the (II) oxidation state produce ^{119}Sn NMR peaks in the range of −1000 to 500 ppm.[86−92] For the 3D $FASnI_3$ (Figure 8a), the peak centered at 166 ppm is attributed to the Sn atoms in an octahedral coordinated tin iodide network. By comparison, the 3D $FASnBr_3$ materials produced a peak at −138 ppm due to the Sn atoms coordinated to Br atoms. For the $FASnI_{1.9}Br_{1.1}$ and $FASnI_{0.4}Br_{2.6}$ alloys, the peaks centered at −7 and −31 ppm, respectively, indicate the different local chemical environments of the Sn atoms, which are coordinated to both I and Br sites. The full-width-at-half-maximum (fwhm) values associated with the $FASnI_{1.9}Br_{1.1}$ (fwhm: 178 ppm, ~53 kHz) and $FASnI_{0.4}Br_{2.6}$ (322 ppm, ~96 kHz) compounds, as compared to the pure phases: $FASnI_3$ (121 ppm, ~36 kHz) and $FASnBr_3$ (131 ppm, ~36 kHz), further corroborate these results. Specifically, the fwhm of ~322 ppm (96 kHz) in the Br-rich phase, which is identical to the chemical shift difference $\Delta\delta(^{119}Sn) = 304$ ppm (~91 kHz) between $FASnI_3$ and $FASnBr_3$. The different lineshapes associated with the $FASnI_{1.9}Br_{1.1}$ and $FASnI_{0.4}Br_{2.6}$ compounds by means of both chemical shifts and fwhm values suggests halide mixing. It is noteworthy that halide hopping may occur in such species, and degradation products may also form upon exposure to ambient conditions, as previously studied by ssNMR spectroscopy.[86,88−90] Additionally, the ^{1}H NMR spectra of $FASnI_3$ and $FASnI_{1.9}Br_{1.1}$ phases (Figure 8b) exhibited peaks associated with FA cations corresponding to NH_2 (7.2 ppm) and CH (7.9 ppm) sites. For the $FASnI_3$ and $FASnI_{1.9}Br_{1.1}$ phases, the relatively narrow features appeared for NH_2 (7.5 ppm) and CH (8.1 ppm) sites. These narrow features indicate the faster reorientational dynamics of FA^+ cations in the bromine-rich phases than the iodine-rich phases, due to the different tolerance factors. In addition, the relative difference in the ^{1}H

chemical shifts $\Delta\delta$ ^{1}H (NH_2) = 0.3 ppm, and $\Delta\delta$ ^{1}H (NH) = 0.2 ppm between the bromine-rich and iodine-rich phases indicate the different noncovalent interactions at the organic–inorganic interface. It is noteworthy that the ^{1}H chemical shifts of the FA^+ cations $FASnI_3$ phases (7.2 and 7.9 ppm) are different than the $FAPbI_3$ phases (7.5 and 8.1 ppm), further indicating the different local structures and dynamics of cage cations.[93] The solid-state NMR data reinforces the different local environments for the Sn centers, specifically being well aligned with the distribution of distance vectors in the PDF. The unique ability to probe the organic cation, which is not easily seen through X-ray scattering techniques, adds additional evidence for the above-mentioned structural distortions that increase on a local scale with $Br^−$ concentration as the FA^+ cations due to different local chemical environments, with an extended pseudo-0D framework as opposed to the more rigid SnI_6 cage structure. The different local chemical environments of FA^+ and their intermixing nature is further corroborated by analyzing 2D ^{1}H−^{1}H spin-diffusion NMR spectra of $FASnI_{1.9}Br_{1.1}$ and $FASnI_{0.4}Br_{2.6}$ compounds. A beneficial feature of 2D ^{1}H spin diffusion experiment is that it allows spin magnetization to exchange between dipole−dipole coupled ^{1}H−^{1}H sites, enabling the through-space proximities between them to be probed and distinguished. Close proximities are manifested as off-diagonal peaks, while the on-diagonal peaks are characteristic to chemical shifts. For the I-rich $FASnI_{1.9}Br_{1.1}$, the SD spectrum acquired with 200 ms showed broad on-diagonal features for NH_2 and CH sites, and the off-diagonal features (gray bands) indicate the strong dipolar interactions between them. By comparison, the Br-rich $FASnI_{0.4}Br_{2.6}$ compound displays narrow features for NH_2 with up to five partially resolved contributions (Figure S8a) due to the different local chemical environments of these sites and CH sites. The well-resolved off-diagonal features between these sites suggest stronger dipolar interactions due to the close inter- and intramolecular proximity. More importantly, the peaks depicted in the red arrows indicate the close proximities between the NH_2 groups in FA cations at different local chemical environments, indicating the intermixing of Br/I halide sites rather than a phase separation. This is further corroborated by acquiring and analyzing the ^{1}H SD spectra of this latter compound with different spin diffusion mixing times (Figure S8). Overall, the 2D solid-state NMR analysis confirms the different local chemical environments of FA cations and their proximities in I-rich and Br-rich alloys.

3.4. Optical Properties. 3.4.1. Diffuse Reflectance UV−Vis Spectroscopy.
The optical diffuse reflectance absorption edges for selected compositions (Figure 9a) shows a blue shifting (widening) of the band gap across the composition space from x = 0−3 based on movement of the linear onset of the absorption. The band gap can then be approximated through the linear extrapolation of the linear onset of the absorption with the observed background before the absorption edge.[94] Through this approximation, we estimate the band gap of $FASnI_3$ to be ~1.31 eV and $FASnBr_3$ to be ~2.24 eV which is within range of band gaps obtained for these materials in previous works[31,32] given that is has been shown that the band gap of hybrid perovskite materials can vary based on the preparation method.[31] These band gaps values can be compared to both end compositions of their lead counterparts, where $FAPbI_3$ (α-phase) and $FAPbBr_3$ have a band gap of 1.48 eV[31,34] and 2.30 eV,[95] respectively.
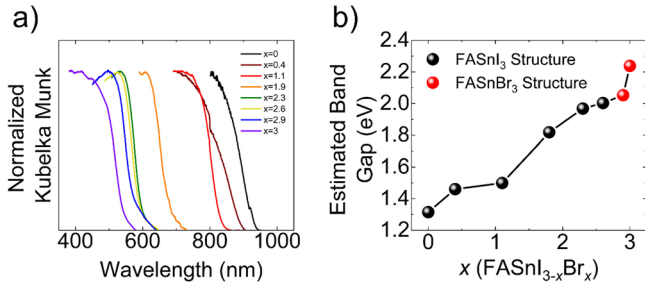
Figure 9. (a) Diffuse reflectance UV−vis spectra for selected compositions, highlighting the positions of the absorption edges and (b) estimated optical band gap for selected compositions in the $FASnI_{3-x}Br_x$ ($x = 0-3$) composition space. The compounds are labeled in black and red depending on if they adopt the $FASnI_3$ or $FASnBr_3$ structure type.

When plotting the estimated gap for the title compounds with respect to composition (Figure 9b), we find that for those compounds that adopt the $FASnI_3$, $Pm\bar{3}m$, structure there is a near linear behavior consistent with increasing concentrations of the smaller Br^- frontier orbitals. However, with the shift toward the $FASnBr_3$, $Pa\bar{3}$, structure, there is a sharp widening of the gap from 2.05 to 2.24 eV, which the disruption in the structure can explain. As 3 of the 6 bonds elongate, the overall orbital overlap of the material drastically decreases, leading to a sharp decrease in the band dispersion. Such an explanation is confirmed through the calculation of the band structures (*vide infra*). Therefore, the $FASnBr_3$ compositions can be considered the extreme example where the overlap is removed almost entirely for half of the Sn − X bonds. This idea can also be reconciled with other studies on "hollow" perovskites where substitution of $[MX_6]$ octahedra for an organic molecule leads to a blue shifting of the gap as the overall orbital overlap between the metal and halide reduces with increased substitution levels.[85,96]

These trends can also be compared with that of $CsSnBr_3$ with its 3D perovskite structure.[77] The observed difference in bandgap between both ends of halide members in our compounds is 0.93 eV: 1.31 eV for $FASnI_3$ compared to 2.24 eV for $FASnBr_3$. This can be compared to a 0.6 eV difference in the cesium lead halide perovskites: 1.68 eV band gap for black $CsPbI_3$[97] and 2.29 eV for $CsPbBr_3$.[98] Another relatively smaller difference in bandgap is 0.47 eV when comparing the bandgaps of $CsPbBr_3$ (2.29 eV) and $CsSnBr_3$ (1.82 eV).[77,99] We therefore attribute the higher bandgap difference in our compounds between the bromide and iodide compounds to the emerged structural changes leading to the disconnection of the proper 3D perovskite network.

3.4.2. Photoluminescence Spectroscopy. The Photoluminescence (PL) spectroscopy for selected compositions was performed using thin film samples (Figure 10a). A stock solution of 0.8 M was used for spin coating the tin perovskite thin films in the glovebox. Given the enhanced sensitivity of the PL measurement for thin films, our PL measurements on thin films gave stronger PL peaks compared to powder samples.

For the first three selected samples, the PL peak position increases in energy with respect to composition as the emission was detected at 869, 763, and 729 nm for $FASnI_3$, $FASnI_{2.3}Br_{0.7}$, and $FASnI_{1.9}Br_{1.1}$ respectively (Figure 10b, c). These results are in accordance with our optical band gap measurements on these samples. However, as the concentration of incorporated bromide into the crystalline structure increased, there was a drastic quenching of the PL intensity. Comparing the PL intensity of $FASnI_3$ vs $FASnI_{2.3}Br_{0.7}$ (Figure 10b) more than 90% of the observed intensity was lost. This quenching effect increased as PL emission fell below the background for $FASnI_{1.1}Br_{1.9}$ and $FASnBr_3$. (Figure 10d). Time-resolved photoluminescence (TRPL) spectra showed a significant drop in PL lifetime by increasing the bromide concentration. The $FASnI_{2.3}Br_{0.7}$, and $FASnI_{1.9}Br_{1.1}$ samples
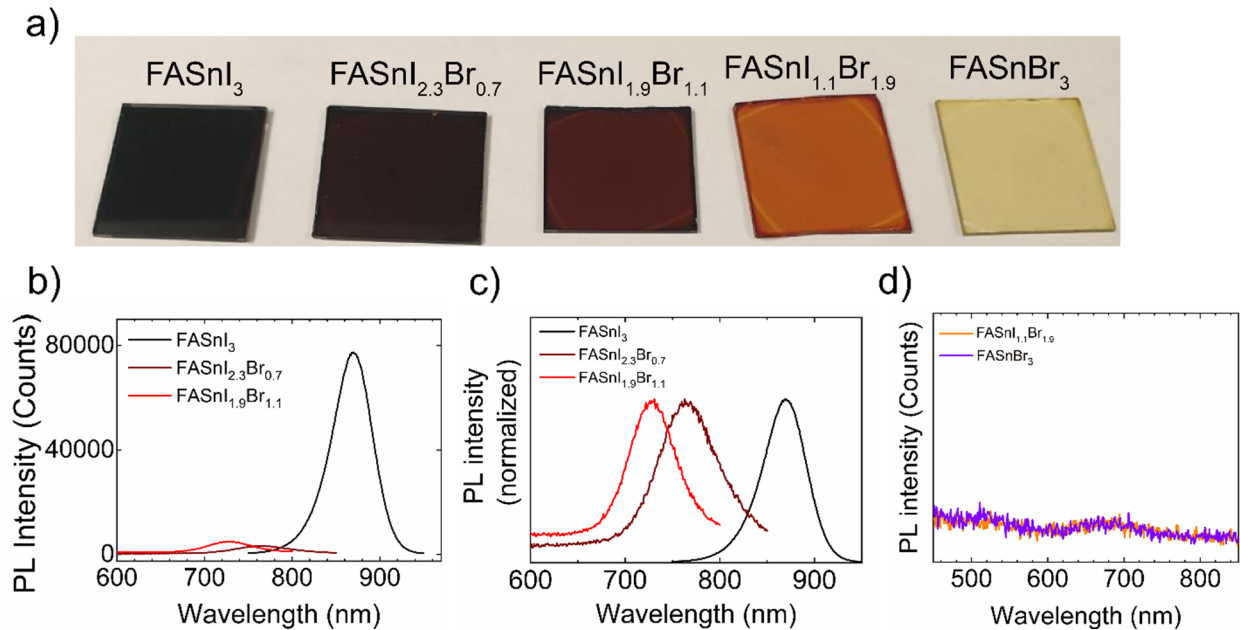
Figure 10. Photoluminescence (PL) of thin films for selected compositions to investigate the PL transition in $FASnI_{3-x}Br_x$ ($x = 0-3$) series. (a) Image of representative thin film samples, (b) PL absolute value spectra showing drastic decrease in intensity with Br incorporation, (c) normalized PL spectra of the first three selected composition from iodide rich region, and (d) no PL intensity for bromide rich compositions.
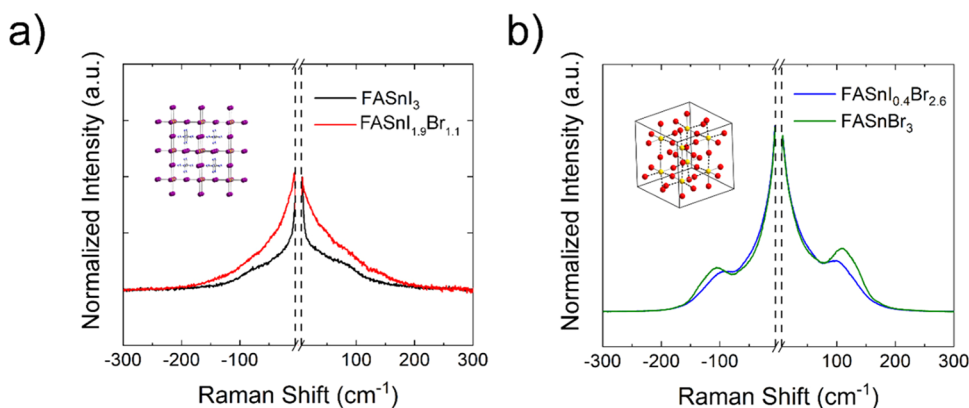
Figure 11. (a) Raman spectrum for $FASnI_3$ and $FASnI_{1.9}Br_{1.1}$ in black and red, respectively. The inset shows the 3D $FASnI_3$ perovskite structure. (b) Raman spectrum of $FASnI_{0.4}Br_{2.6}$ and $FASnBr_3$ in blue and green, respectively. The inset depicts the $FASnBr_3$ 0D structure. Both graphs have the -7 to 7 cm^{-1} range omitted to remove the intensity from the excitation laser.

have a lifetime shorter than 1 ns and their decay curve interferes with the width of our instrument response function (IRF). (Figure S9).

The strong structural transitions induced by increasing the concentration of bromide can be the origin of the observed PL quenching and reduced lifetime. Through the compositional changes from iodide rich phase to bromide rich phase, the dominance of the pseudo 0D $[SnBr_3]^-$ molecular units (antiferroelectric distortions) across the lattice was observed rather than corner-sharing $[SnBr_6]^{4-}$ octahedral units. As discussed in the structural section, these changes happen when 3 of the 6 bonds in the $SnBr_6$ octahedra extend to make room for the lone pair. Formation of these isolated $[SnBr_3]^-$ structural units limits the charge transfer across the lattice, increasing the nonradiative recombination and eventually leading to quenching of the PL intensity. In contrast, the perovskite structure of three-dimensional $CsSnBr_3$ possesses corner-sharing $SnBr_6$ units and shows photoluminescence.[77] The observed structural transition in $FASnBr_3$ and the evolution of more isolated $[SnBr_3]^-$ units can be attributed to the presence of the FA^+ cation, which is bulkier (with an effective radius of 258 pm)[72] compared to Cs (184 pm)[73] leading to deformation of $[SnX_6]^{4-}$ octahedral units by decreasing the size of halide and the cavity between the corner shared units.

These results are in accordance with pressure-induced structural changes that directly impact the optoelectronic properties of tin bromide compounds.[74] Moreover, the Ge off-centering observed in germanium iodide perovskites (with different cations, FA, MA or Cs) was observed leading to undetectable PL intensity for this material at ambient conditions while higher pressure-induced recovery of 3D structure and improving related PL intensity.[62] While similar pressure-induced phase transitions studies were performed on tin halide perovskites,[74] to our knowledge, no studies have been done on the mixed halide (specifically $FASnI_{3-x}Br_x$) compositions. We eagerly propose performing this study where our results indicate similar PL behavior will be observed. To investigate the mechanism of PL quenching further, low frequency Raman spectroscopy was conducted on select samples.

3.4.3. Raman Spectroscopy. Given the presence of structural differences between $FASnI_3$ and $FASnBr_3$, the observed temperature-dependent phase transition of $FASnI_{0.4}Br_{2.6}$, deviation in the local inorganic framework, and the

complete PL quenching for samples having Br^- fractions exceeding and including $x = 1.9$, room temperature low frequency Raman spectroscopy was conducted on 4 select samples to confirm further lattice distortions characteristic of the $Pa\bar{3}$ phase for compositions that retain an average 3D perovskite structure at room temperature. Presented in Figure 11, spectra for $FASnI_3$ and $FASnBr_3$ were collected to form a baseline for the two different structural variations as well as for $FASnI_{1.9}Br_{1.1}$ and $FASnI_{0.4}Br_{2.6}$ since these compositions were structurally studied at low temperatures through single crystal X-ray diffraction and retain an average 3D structure at room temperature.

The vibrational density of states of hybrid halide perovskites typically exhibit 3 different regions based on the shift, with the regions being well-defined for the Pb analogues: $10-50$ cm^{-1} (PbX_6 lattice modes mostly related to octahedra rotations), $50-500$ cm^{-1} (coupled lattice and organic modes, including $Pb - X$ stretching modes), and $500-3500$ cm^{-1} (individual molecular modes).[100] Here we present data within the two spectral ranges corresponding to the lattice and organic-lattice coupled vibrational modes within the $7-300$ cm^{-1} range. The Raman scattering selection rules for the $Pm\bar{3}m$ perovskite lattice indicates that in the harmonic approximation, no lattice optical modes should be Raman active.[101] These selection rules can be broken when anharmonic and relaxation processes are present, leading to quasi-elastic signatures in hybrid and inorganic perovskites.[101,102] The observed spectrum of $FASnI_3$ is consistent with this behavior (Figure 11a), were a small contribution appears around 88 cm^{-1} as a shoulder. It is attributed to the Raman activation of a lattice mode by anharmonic processes. This broadness at low frequencies highlights the dynamicity of the inorganic lattice and is similar to other hybrid halide perovskite materials that have been studied previously.[100,102,103] $FASnBr_3$ similarly to $FASnI_3$ is broad at very low energies, suggesting the same dynamicity for the inorganic framework, likely caused by relaxation processes related to local rotations. Additionally, there is a sharper, more intense higher energy feature centered around 110 cm^{-1}. Studies conducted on $MASnI_3$ would suggest that this stretch corresponds to a vibration mode of the organic coupled with $Sn - Br$ stretching..[104] However, studies conducted by Gao et al. on the $CsMBr_3$ family (M = Ge, Sn, Pb) suggest a more adequate assignment of this feature to structural distortions due to expression of $5s$-electron lone pairs of Sn. A similar, albeit higher energy, feature is experimentally observed in the

Raman scattering of CsGeBr$_3$ assigned to Ge off-centering.[105] The observation of the 110 cm^{-1} feature fits nicely with the assignment of the $Pa\bar{3}$ space group, where Raman scattering selection rules are different and optical lattice modes can be observed even in the harmonic approximation. It should also be noted that the components and irreducible representations of the Raman modes can be mapped using a similar methodology used to analyze the CsGeX$_3$ (X = I, Br, Cl) series,[106] but such analysis falls outside the scope of the presented work.

The I-rich and Br-rich compounds tested in the FASnI$_{3-x}$Br$_x$ ($x = 0-3$) mixed halide space showed identical behavior to the end member closest to in composition (Figure 11a and 11b). FASnI$_{1.9}$Br$_{1.1}$ has a broad spectrum with a slightly more intense peak at the lowest energies. This supports the idea that the structure does not locally distort with appreciable concentrations for the experiment since a high intensity feature around 90−110 cm^{-1} is not present. FASnI$_{0.4}$Br$_{2.6}$, on the other hand, displays nearly identical behavior to FASnBr$_3$ with a higher energy feature, which is slightly broadened and shifted to lower energies (peak center around 99 cm^{-1}). The shift and broadening of the peak are consistent with both the incorporation of increased I$^-$ fractions, as the Sn − I bond is weaker and longer than the Sn − Br bond, and the reduction of distortions. The presence of this feature does, however, support the presence of relatively isolated pyramidal-like structural units which get more numerous with higher bromide concentration (See the related peak in Raman spectra of FASnI$_{0.4}$Br$_{2.6}$ and FASnBr$_3$ in Figure 11b). The distribution of local low symmetry lattice distortions is leading to the breaking of the Raman selection rules despite the refinement of the average crystal structure in a $Pm\bar{3}m$ space group. Combining these findings with the conclusions drawn by the room temperature and low temperature single crystal diffraction experiments indicates that although the lattice is dynamic and maintains a 3D structure, the Sn lone pairs locally compete for their own space. Further theoretical studies into the vibrational modes of these mixed halide compositions could verify the assignments of these peaks.

3.5. Photostability of FASnI$_{3-x}$Br$_x$ Films. The photostability of mixed halide lead perovskite in operational conditions is an important research topic and has been investigated considerably.[107,108] A common practice for the synthesis of wide bandgap perovskites (>1.65 eV) is through the substitution of iodide with bromide (more than 20%).[109] These compositions, however, destabilize under prolonged illumination through phase segregation, i.e. under light illumination, Iodide-rich and Iodide-poor regions are formed. This phenomenon is called "halide segregation" and can be investigated by the photoluminescence (PL) study of related thin films upon exposure to light.

Here, we studied this phenomenon for the Sn-mixed halide films including FASnI$_3$, FASnI$_{2.6}$Br$_{0.4}$, FASnI$_{2.3}$Br$_{0.7}$, and FASnI$_{1.9}$Br$_{1.1}$. Since the primary method for observing this halide segregation is observing shifts in the PL peak position, only a limited scope of compositions was studied. The PL peak shift position is a measure of the quantity of iodide-rich phase formed. A detailed description of the film fabrication and the study is presented in the experimental section. The obtained PL spectra of each thin film as a function of illumination time are presented in Figure 12.

As a general reflection on the PL graphs for all the samples, we observed a decay in PL intensity for all samples after light
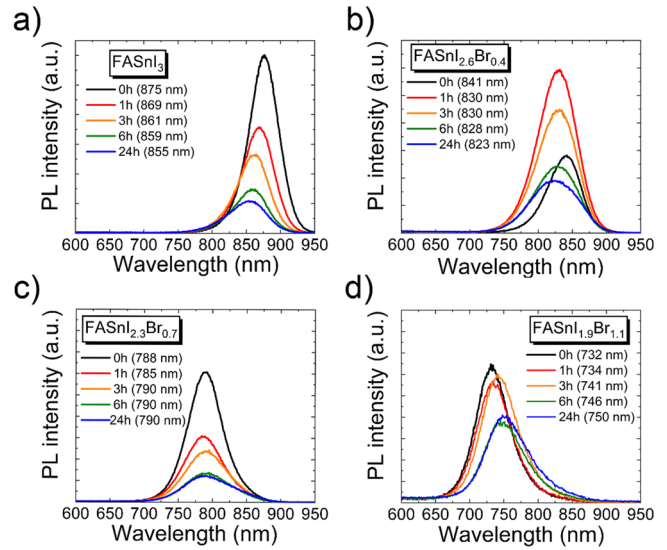

Figure 12. Steady-state PL emission spectra under continuous illumination: (a) FASnI$_3$, (b) FASnI$_{2.6}$Br$_{0.4}$, (c) FASnI$_{2.3}$Br$_{0.7}$, and (d) FASnI$_{1.9}$Br$_{1.1}$. Each graph presents the PL emission spectra of related films before illumination at 0 time and after 1, 3, 6, and 24 h of illumination under 1 sun. Detailed PL peak positions are listed in Table S8.

illumination. This process is typical for perovskite thin films and is often induced by ambient exposure, high temperature, and illumination. For the FASnI$_3$ film a blue shift of 20 nm was observed after 24 h of illumination, which is solely induced by film degradation under ambient conditions and to a lesser extent induced by high temperature due to light illumination. The ambient exposure in tin perovskites can induce tin(II) partial oxidations to tin(IV) causing such blue shifting.

For the mixed halide phases, peak shifts of 18, 2, and 18 nm were observed for FASnI$_{2.6}$Br$_{0.4}$, FASnI$_{2.3}$Br$_{0.7}$, and FASnI$_{1.9}$Br$_{1.1}$ respectively. The observed shift in FASnI$_{2.6}$Br$_{0.4}$ is toward higher wavelength (similar to that of FASnI$_3$ thin films) indicating the origin of the shift is degradation of the perovskite films due to ambient atmosphere and heat exposure (rather than halide segregation). Considering the energy difference between the valence band maximum position of iodide rich compositions (compared to that of bromide rich) they are more susceptible to oxidative degradation, hence a blue shift of the PL peak position was observed. A temporary increase in PL intensity is also observed after 1 and 3 h of illumination. The origins of this, though, would require further investigation but can be referred to light-induced passivation caused by a rapid increase of quasi-Fermi level splitting ($\Delta\mu$) which was observed in perovskite mixed halide compositions shortly after light illumination.[110,111] Enhanced PL intensity by increasing the quasi-Fermi level splitting is mostly effective in short light illumination times when a limited bandgap shift is detected. Our findings suggest that we observed the same phenomenon where enhanced PL intensity with limited PL peak position was observed after 1 and 3 h of light soaking.

FASnI$_{1.9}$Br$_{1.1}$ thin film showed a red shift of 18 nm after 24 h of illumination. This is indicative of a dominating halide segregation effect due to the formation of iodide-rich regions of the film, which have narrower band gaps and lower energy PL emissions. For FASnI$_{2.3}$Br$_{0.7}$, only a 2 nm shift was observed alongside decreased PL intensity, suggesting that both film degradation and halide segregation are occurring simulta-
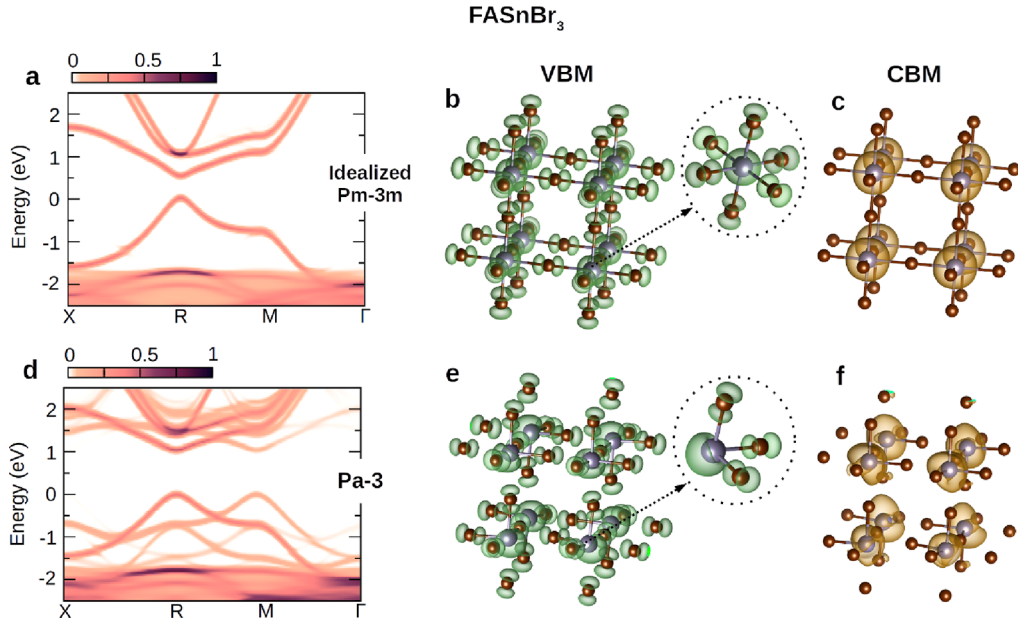
FASnBr$_3$

Figure 13. Electronic properties of idealized (P$m\bar{3}m$) and distorted (P$a\bar{3}$) FASnBr$_3$. Electron spectral functions (color maps) and charge densities of the idealized FASnBr$_3$ (a−c) and distorted FASnBr$_3$ (d−f). Electron spectral functions (a,d) are evaluated using band structure unfolding. The energy axes are adjusted so that the VBM is set at zero energy. Charge densities at the VBM (b,e) and CBM (c,f) are evaluated at the R-point of the fundamental Brillouin zone of the idealized FASnBr$_3$ P$m\bar{3}m$ unit cell. In the ball and stick models, the FA molecules are removed for clarity.

neously. This is clear when considering the shape of PL spectra of the FASnI$_{2.3}$Br$_{0.7}$ composition after illumination, where peak broadening happens for this specific composition more than others (Figure 12a−d). We detected a fwhm of 62 nm before illumination which gradually increased after light illumination to 86 nm after 24h (Table S9).

The degree of PL peak shifts for these Sn perovskites mimic their lead counterparts, suggesting that these phases may benefit from the same approaches used to control halide segregation investigated for the Pb-based materials such as dimensional control[112] or octahedral tilting distortions through structural modifications.[113,114]

3.6. Impact of Lone Pair Expression Studied with Density Functional Theory (DFT). Based on first-principles calculations (see computational details), we investigate the structural and electronic properties of FASnI$_{3-x}$Br$_x$, for x = 0, 0.417, 2.583, and 3. We include the effect of local disorder (polymorphism, see computational details) that has been demonstrated to be ubiquitous in perovskite physics to describe the distribution of local octahedra rotations in nominally P$m\bar{3}m$ structures.[52] In the case of FASnI$_3$ and FASnBr$_3$, accounting for local disorder leads to an energy stabilization of 87.3 meV/f.u. and 124.8 meV/f.u. respectively compared to their idealized P$m\bar{3}m$ structures. In addition, this computational protocol provides DFT-optimized structures consistent with the experimentally determined averaged structures, exhibiting very clear structural distortions characteristic of stereochemically expressed Sn-5s^2 lone-pair for FASnBr$_3$. In contrast, it is found to a lesser extent for FASnI$_3$ (Figure 13a). Let us note that larger supercells might lead to a better description of the effect in FASnI$_3$.

To ease comparison between the various compositions, we use the band structure unfolding technique, leading to representations of the distorted P$a\bar{3}$ electronic structure in the Brillouin zone of the parent P$m\bar{3}m$ structure (Figure 13d).[53] This representation also has the advantage of linking

the additional electronic contributions to structural lattice distortions concerning the parent cubic structure. All structures show a direct band gap at the R point. Consistently with experimental findings, increasing the bromine concentration sizably increases the computed fundamental band gap, from 0.38 eV for FASnI$_3$ to 1.04 eV for FASnBr$_3$ (Figure S13b-e). Such an increase is expected upon halide substitution. Concomitantly, band curvature at the band edges increases and bands undergo smearing across the Brillouin zone. In order to disentangle the respective effect of local antiferrodistorsive disorder and stereochemical expression of the Sn-5s^2 lone-pair, we further compare the electronic structure of FASnBr$_3$ to that of related model structures.

First, the comparison is carried between the momentum-resolved density of states (electron spectral function) computed for FASnBr$_3$ in the cubic P$a\bar{3}$ space group with and without taking into account local antiferrodistortive disorder. Both plots show no significant differences (Figure S14). This suggests this structural disorder does not play a predominant role in the new features observed with increasing bromine content (Figure 13d). Then, to inspect the specific effect of the structural distortion attributed to the lone-pair expression in the P$a\bar{3}$ structure, we compute the electronic properties of the idealized structure of FASnBr$_3$ where atoms of the inorganic network are fixed to the Wyckoff positions of the P$m\bar{3}m$ symmetry (Figure 13a), for which this structural feature is absent. The corresponding electronic structure exhibits a direct band gap of 0.52 eV and hole (electron) effective masses of m$_h$ = 0.086 m$_0$ (m$_e$ = 0.117 m$_0$), where m$_0$ is the free electron mass. The charge density plots of the valence band maximum (VBM) and conduction band minimum (CBM) at the R-point reveal that the VBM is determined by the antibonding coupling of the Sn-5s and Br-4p orbitals (Figure 13b), while the CBM mainly stems from Sn-5p orbitals (Figure 13c). Conversely, the corresponding charge densities computed for the P$a\bar{3}$ structure (Figures 13e

and f, respectively) provide clear evidence of asymmetric charge redistribution due to the lone pair-induced structural distortion. Specifically, the lone pair manifests as an off-center lobe of electron density around the Sn atom, which diminishes the antibonding interaction between the Sn-5s and Br-4p orbitals in the three shortest Sn − Br bonds. Consequently, the band gap increases markedly to 1.04 eV, alongside a significant change in the effective masses, with the hole mass $m_h = 0.167$ m_0 and $m_e = 0.240$ m_0. The observed energy smearing with the formation of new states at the X and M points (Figure 13d) can also be traced back to the stereochemical expression of the Sn $5s^2$ lone-pair. The formation of these new states at the X and M points can be understood as replicas of the states at the R point induced by lowering the symmetry due to the lone pair-induced lattice distortion. For completeness, we also report the projected density of states calculated for the two structures in Figure S15.

4. CONCLUSIONS

The FASnI$_{3-x}$Br$_x$ (x = 0−3) series represents a group of compounds that, on the surface, fulfills the role of a more environmentally sustainable alternative to Pb MHPs given their suitable band gaps for single and multijunction solar cell devices. However, an in-depth analysis of the structure−property relationships suggests that local structural dynamics leads to the degradation of the coveted optoelectronic properties, namely the photoluminescence and lifetime. The room temperature crystal structures are the first indication of such fluctuations with the phase space behaving as a nonideal "solid-solution" where the x = 0−2.9 compounds crystallize in P$m\overline{3}m$ while FASnI$_{0.1}$Br$_{2.9}$ and FASnBr$_3$ are of lower symmetry (P$a\overline{3}$) due to significant Sn off-centering from $5s^2$ loan pair expression. Probing the local perturbations of the lattice for the I-rich and Br-rich regions through Raman scattering and Pair Distribution Function (PDF) elucidates antiferroelectric distortions. The short-range PDF curve for FASnI$_{0.4}$Br$_{0.6}$ provides the most informative view of the inorganic framework as it is consistent with a FASnBr$_3$-type structure (P$a\overline{3}$) yet averages to a P$m\overline{3}m$ structure type. Solid-state ^{119}Sn and ^{1}H NMR bolster this claim with varying chemical shifts of the Sn and the interrogation of the local structure of the organic. The FA$^+$ cation shows sharper features for Br-rich samples as opposed to I-rich most likely due to a more loosely connected framework associated with a relatively weaker cage. Competition between the concealment and expression of the Sn lone pair then provides a rationale for the observed PL quenching upon adding Br$^-$ starting from FASnI$_3$. Theoretical calculations further support the complex dynamics and the origins of the dissipation of the typically robust PL and electronic properties where the calculated effective mass for both holes and electrons effectively doubles between a hypothetical pristine P$m\overline{3}m$ and the true distorted P$a\overline{3}$ structure of FASnBr$_3$. The phase space may prove to be even more problematic for adoption in photovoltaics given the observation of halide segregation upon light illumination, which was explored for those compounds that showed an observable PL emission above the background. FASnI$_{1.9}$Br$_{1.1}$ shows a gradual red-shifting of the peak position after 0 to 24 h of 1 sun light exposure, consistent with halide segregation. It remains to be seen, though, if these materials would benefit from the same methods used to mitigate halide segregation of the Pb-based counterparts. This research provides a fundamental guide to synthesizing and characterizing these compounds for further

study while simultaneously developing a cautionary stance toward blind assumptions regarding halide perovskite structure and application. To fully grasp the potential applications for these chemically substituted phases, a prior understanding of the fundamental chemical influences at play remains crucial.

■ ASSOCIATED CONTENT

Data Availability Statement

The DFT calculations (input and output files) employed for this study are available via the NOMAD repository [https://doi.org/10.17172/NOMAD/2024.05.09-1].

Ⓢ Supporting Information

The Supporting Information is available free of charge at https://pubs.acs.org/doi/10.1021/jacs.4c03669.

Additional synthetic procedures and experimental methods, bulk X-ray powder diffraction patterns, additional sample photo for FASnBr$_3$ and FASnI$_{0.1}$Br$_{2.9}$, additional SEM images, reciprocal space images, PDF curves considering an extended range of r, fitted PDF curves, 2D ^{1}H−^{1}H spin-diffusion (SD) NMR spectra, time-resolved photoluminescence spectra, photo of the light illumination setup, photo of sample holders used for Raman spectroscopy, additional band structure diagrams and density of states plots, additional crystallographic information tables for the title compounds, the low temperature refinement of FASnI$_{0.4}$Br$_{2.6}$, and identified impurity phases, average atomic percentages from SEM-EDS experiments, PL peak position table for light illumination studies, calculated fwhm values for FASnI$_{2.3}$Br$_{0.7}$ thin films after illumination, and additional references (PDF)

Accession Codes

CCDC 2335358−2335370 contain the supplementary crystallographic data for this paper. These data can be obtained free of charge via www.ccdc.cam.ac.uk/data_request/cif, or by emailing data_request@ccdc.cam.ac.uk, or by contacting The Cambridge Crystallographic Data Centre, 12 Union Road, Cambridge CB2 1EZ, UK; fax: +44 1223 336033.

■ AUTHOR INFORMATION

Corresponding Authors

Mercouri G. Kanatzidis − *Department of Chemistry, Northwestern University, Evanston, Illinois 60208, United States;* ◉ orcid.org/0000-0003-2037-4168; Email: m-kanatzidis@northwestern.edu

Majid Safdari − *Department of Chemistry, Northwestern University, Evanston, Illinois 60208, United States; Department of Chemistry, Division of Applied Physical Chemistry, KTH Royal Institute of Technology, SE-100 44 Stockholm, Sweden;* Email: majid.safdari@northwestern.edu

Authors

Adam Balvanz − *Department of Chemistry, Northwestern University, Evanston, Illinois 60208, United States;* ◉ orcid.org/0000-0001-5378-7327

Marios Zacharias − *Univ Rennes, INSA Rennes, CNRS, Institute FOTON − UMR 6082, Rennes F-35000, France;* ◉ orcid.org/0000-0002-7052-5684

Daehan Kim − *Department of Chemistry, Northwestern University, Evanston, Illinois 60208, United States;* ◉ orcid.org/0000-0003-2359-1862

Claire Welton − *University of Lille, CNRS, Centrale Lille, Univ. Artois, UMR 8181 − UCCS − Unité de Catalyse et Chimie du Solide, Lille F-59000, France*

Evan H. Oriel − *Department of Chemistry, Northwestern University, Evanston, Illinois 60208, United States;* orcid.org/0000-0003-2632-5447

Mikaël Kepenekian − *Univ Rennes, INSA Rennes, CNRS, ISCR − UMR 6226, Rennes F-35000, France;* orcid.org/0000-0001-5192-5896

Claudine Katan − *Univ Rennes, INSA Rennes, CNRS, ISCR − UMR 6226, Rennes F-35000, France;* orcid.org/0000-0002-2017-5823

Christos D. Malliakas − *Department of Chemistry, Northwestern University, Evanston, Illinois 60208, United States;* orcid.org/0000-0003-4416-638X

Jacky Even − *Univ Rennes, INSA Rennes, CNRS, Institute FOTON − UMR 6082, Rennes F-35000, France;* orcid.org/0000-0002-4607-3390

Vladislav Klepov − *Department of Chemistry, Northwestern University, Evanston, Illinois 60208, United States; Department of Chemistry, University of Georgia, Athens, Georgia 30602, United States;* orcid.org/0000-0002-2039-2457

G. N. Manjunatha Reddy − *University of Lille, CNRS, Centrale Lille, Univ. Artois, UMR 8181 − UCCS − Unité de Catalyse et Chimie du Solide, Lille F-59000, France*

Richard D. Schaller − *Department of Chemistry, Northwestern University, Evanston, Illinois 60208, United States; Center for Nanoscale Materials, Argonne National Laboratory, Lemont, Illinois 60439, United States;* orcid.org/0000-0001-9696-8830

Lin X. Chen − *Department of Chemistry, Northwestern University, Evanston, Illinois 60208, United States; Chemical Sciences and Engineering Division, Argonne National Laboratory, Lemont, Illinois 60439, United States;* orcid.org/0000-0002-8450-6687

Ram Seshadri − *Materials Department and Materials Research Laboratory, University of California, Santa Barbara, California 93106, United States;* orcid.org/0000-0001-5858-4027

Complete contact information is available at:
https://pubs.acs.org/10.1021/jacs.4c03669

Notes

The authors declare no competing financial interest.

■ REFERENCES

(1) Xing, G.; Mathews, N.; Sun, S.; Lim, S. S.; Lam, Y. M.; Grätzel, M.; Mhaisalkar, S.; Sum, T. C. Long-Range Balanced Electron- and Hole-Transport Lengths in Organic-Inorganic $CH_3NH_3PbI_3$. *Science* **2013**, *342* (6156), 344−347.

(2) Dong, Q.; Fang, Y.; Shao, Y.; Mulligan, P.; Qiu, J.; Cao, L.; Huang, J. Electron-hole diffusion lengths in solution-grown $CH_3NH_3PbI_3$ single crystals. *Science* **2015**, *347* (6225), 967−970.

(3) Yin, W.-J.; Shi, T.; Yan, Y. Unique Properties of Halide Perovskites as Possible Origins of the Superior Solar Cell Performance. *Adv. Mater.* **2014**, *26* (27), 4653−4658.

(4) Motta, C.; El-Mellouhi, F.; Sanvito, S. Charge carrier mobility in hybrid halide perovskites. *Sci. Rep.* **2015**, *5* (1), 12746.

(5) Roy, P.; Kumar Sinha, N.; Tiwari, S.; Khare, A. A review on perovskite solar cells: Evolution of architecture, fabrication techniques, commercialization issues and status. *Sol. Energy* **2020**, *198*, 665−688.

(6) Stoumpos, C. C.; Kanatzidis, M. G. Halide Perovskites: Poor Man's High-Performance Semiconductors. *Adv. Mater.* **2016**, *28* (28), 5778−5793.

(7) Stoumpos, C. C.; Kanatzidis, M. G. The Renaissance of Halide Perovskites and Their Evolution as Emerging Semiconductors. *Acc. Chem. Res.* **2015**, *48*, 2791−2802.

(8) Chung, I.; Lee, B.; He, J. Q.; Chang, R. P. H.; Kanatzidis, M. G. All-solid-state dye-sensitized solar cells with high efficiency. *Nature* **2012**, *485* (7399), 486−U494.

(9) Lee, M. M.; Teuscher, J.; Miyasaka, T.; Murakami, T. N.; Snaith, H. J. Efficient Hybrid Solar Cells Based on Meso-Superstructured Organometal Halide Perovskites. *Science* **2012**, *338* (6107), 643−647.

(10) Wang, R.; Mujahid, M.; Duan, Y.; Wang, Z. K.; Xue, J.; Yang, Y. A Review of Perovskites Solar Cell Stability. *Adv. Funct. Mater.* **2019**, *29* (47), 1808843.

(11) Peng, W.; Mao, K.; Cai, F.; Meng, H.; Zhu, Z.; Li, T.; Yuan, S.; Xu, Z.; Feng, X.; Xu, J.; et al. Reducing nonradiative recombination in perovskite solar cells with a porous insulator contact. *Science* **2023**, *379* (6633), 683−690.

(12) Park, J.; Kim, J.; Yun, H.-S.; Paik, M. J.; Noh, E.; Mun, H. J.; Kim, M. G.; Shin, T. J.; Seok, S. I. Controlled growth of perovskite layers with volatile alkylammonium chlorides. *Nature* **2023**, *616* (7958), 724−730.

(13) Zhao, Y.; Ma, F.; Qu, Z.; Yu, S.; Shen, T.; Deng, H.-X.; Chu, X.; Peng, X.; Yuan, Y.; Zhang, X.; et al. Inactive $(PbI_2)_2RbCl$ stabilizes perovskite films for efficient solar cells. *Science* **2022**, *377* (6605), 531−534.

(14) *Best Researhc-Cell Efficiency Chart*. The National Renewable Energy Labratory, 2024. https://www.nrel.gov/pv/cell-efficiency.html (accessed 2024 02/03/2024).

(15) Noh, J. H.; Im, S. H.; Heo, J. H.; Mandal, T. N.; Seok, S. I. Chemical Management for Colorful, Efficient, and Stable Inorganic-Organic Hybrid Nanostructured Solar Cells. *Nano Lett.* **2013**, *13* (4), 1764−1769.

(16) Gil-Escrig, L.; Dreessen, C.; Palazon, F.; Hawash, Z.; Moons, E.; Albrecht, S.; Sessolo, M.; Bolink, H. J. Efficient Wide-Bandgap Mixed-Cation and Mixed-Halide Perovskite Solar Cells by Vacuum Deposition. *ACS Energy Letters* **2021**, *6* (2), 827−836.

(17) Hao, F.; Stoumpos, C. C.; Chang, R. P. H.; Kanatzidis, M. G. Anomalous Band Gap Behavior in Mixed Sn and Pb Perovskites Enables Broadening of Absorption Spectrum in Solar Cells. *J. Am. Chem. Soc.* **2014**, *136* (22), 8094−8099.

(18) Masi, S.; Gualdrón-Reyes, A. F.; Mora-Seró, I. Stabilization of Black Perovskite Phase in $FAPbI_3$ and $CsPbI_3$. *ACS Energy Letters* **2020**, *5* (6), 1974−1985.

(19) Chin, X. Y.; Turkay, D.; Steele, J. A.; Tabean, S.; Eswara, S.; Mensi, M.; Fiala, P.; Wolff, C. M.; Paracchino, A.; Artuk, K.; et al. Interface passivation for 31.25%-efficient perovskite/silicon tandem solar cells. *Science* **2023**, *381* (6653), 59−63.

(20) Hoke, E. T.; Slotcavage, D. J.; Dohner, E. R.; Bowring, A. R.; Karunadasa, H. I.; McGehee, M. D. Reversible photo-induced trap formation in mixed-halide hybrid perovskites for photovoltaics. *Chemical Science* **2015**, *6* (1), 613−617.

(21) Slotcavage, D. J.; Karunadasa, H. I.; McGehee, M. D. Light-Induced Phase Segregation in Halide-Perovskite Absorbers. *ACS Energy Letters* **2016**, *1* (6), 1199−1205.

(22) DuBose, J. T.; Kamat, P. V. Hole Trapping in Halide Perovskites Induces Phase Segregation. *Accounts of Materials Research* **2022**, *3* (7), 761−771.

(23) McMeekin, D. P.; Sadoughi, G.; Rehman, W.; Eperon, G. E.; Saliba, M.; Hörantner, M. T.; Haghighirad, A.; Sakai, N.; Korte, L.; Rech, B.; et al. A mixed-cation lead mixed-halide perovskite absorber for tandem solar cells. *Science* **2016**, *351* (6269), 151−155.

(24) Tan, H. R.; Jain, A.; Voznyy, O.; Lan, X. Z.; de Arquer, F. P. G.; Fan, J. Z.; Quintero-Bermudez, R.; Yuan, M. J.; Zhang, B.; Zhao, Y. C.; et al. Efficient and stable solution-processed planar perovskite solar cells via contact passivation. *Science* **2017**, *355* (6326), 722−726.

(25) Chen, H.; Maxwell, A.; Li, C. W.; Teale, S.; Chen, B.; Zhu, T.; Ugur, E.; Harrison, G.; Grater, L.; Wang, J. K.; et al. Regulating surface potential maximizes voltage in all-perovskite tandems. *Nature* **2023**, *613* (7945), 676.

(26) Abate, A. Perovskite Solar Cells Go Lead Free. *Joule* **2017**, *1* (4), 659−664.

(27) Lye, Y.-E.; Chan, K.-Y.; Ng, Z.-N. A Review on the Progress, Challenges, and Performances of Tin-Based Perovskite Solar Cells. *Nanomaterials* **2023**, *13* (3), 585.

(28) Ke, W.; Stoumpos, C. C.; Kanatzidis, M. G. Unleaded" Perovskites: Status Quo and Future Prospects of Tin-Based Perovskite Solar Cells. *Adv. Mater.* **2019**, *31* (47), 1803230.

(29) Ke, W.; Kanatzidis, M. G. Prospects for low-toxicity lead-free perovskite solar cells. *Nat. Commun.* **2019**, *10* (1), 965.

(30) Abate, A. Stable Tin-Based Perovskite Solar Cells. *ACS Energy Letters* **2023**, *8* (4), 1896−1899.

(31) Stoumpos, C. C.; Malliakas, C. D.; Kanatzidis, M. G. Semiconducting Tin and Lead Iodide Perovskites with Organic Cations: Phase Transitions, High Mobilities, and Near-Infrared Photoluminescent Properties. *Inorg. Chem.* **2013**, *52*, 9019−9038.

(32) Yamada, K.; Fujise, K.; Hino, S.; Yamane, Y.; Nakagama, T. Characterization of Sn(II)-based Perovskites by XRD, DTA, NQR and ^{119}Sn NMR for Photovoltaic Applications. *Chem. Lett.* **2019**, *48* (7), 749.

(33) Sadhanala, A.; Deschler, F.; Thomas, T. H.; Dutton, S. E.; Goedel, K. C.; Hanusch, F. C.; Lai, M. L.; Steiner, U.; Bein, T.; Docampo, P.; et al. Preparation of Single-Phase Films of $CH_3NH_3Pb(I_{1-x}Br_{x)3}$ with Sharp Optical Band Edges. *J. Phys. Chem. Lett.* **2014**, *5* (15), 2501−2505.

(34) Eperon, G. E.; Stranks, S. D.; Menelaou, C.; Johnston, M. B.; Herz, L. M.; Snaith, H. J. Formamidinium lead trihalide: a broadly tunable perovskite for efficient planar heterojunction solar cells. *Energy Environ. Sci.* **2014**, *7* (3), 982−988.

(35) Li, X.; Hoffman, J. M.; Kanatzidis, M. G. The 2D Halide Perovskite Rulebook: How the Spacer Influences Everything from the Structure to Optoelectronic Device Efficiency. *Chem. Rev.* **2021**, *121* (4), 2230−2291.

(36) Stoumpos, C. C.; Cao, D. H.; Clark, D. J.; Young, J.; Rondinelli, J. M.; Jang, J. I.; Hupp, J. T.; Kanatzidis, M. G. Ruddlesden-Popper Hybrid Lead Iodide Perovskite 2D Homologous Semiconductors. *Chem. Mater.* **2016**, *28* (8), 2852−2867.

(37) Vasileiadou, E. S.; Hadar, I.; Kepenekian, M.; Even, J.; Tu, Q.; Malliakas, C. D.; Friedrich, D.; Spanopoulos, I.; Hoffman, J. M.; Dravid, V. P.; et al. Shedding Light on the Stability and Structure-Property Relationships of Two-Dimensional Hybrid Lead Bromide Perovskites. *Chem. Mater.* **2021**, *33* (13), 5085−5107.

(38) Koziskova, J.; Hahn, F.; Richter, J.; Kožíšek, J. Comparison of different absorption corrections on the model structure of tetrakis($\mu 2$-acetato)-diaqua-di-copper(II). *Acta Chimica Slovaca* **2016**, *9*, 136−140.

(39) Dolomanov, O. V.; Bourhis, L. J.; Gildea, R. J.; Howard, J. A. K.; Puschmann, H. OLEX2: a complete structure solution, refinement and analysis program. *J. Appl. Crystallogr.* **2009**, *42* (2), 339−341.

(40) Sheldrick, G. M. SHELXT - Integrated space-group and crystal-structure determination. *Acta Crystallographica A* **2015**, *A71*, 3−8.

(41) Sheldrick, G. M. Crystal structure refinement with SHELXL. *Acta Crystallographica C* **2015**, *C71* (1), 3−8.

(42) Petříček, V.; Dušek, M.; Palatinus, L. Crystallographic Computing System JANA2006: General features. *Zeitschrift für Kristallographie - Crystalline Materials* **2014**, *229*, 345−352.

(43) Palatinus, L.; Chapuis, G. SUPERFLIP - a computer program for the solution of crystal structures by charge flipping in arbitrary dimensions. *J. Appl. Crystallogr.* **2007**, *40*, 786−790.

(44) Andrews, R. H.; Clark, S. J.; Donaldson, J. D.; Dewan, J. C.; Silver, J. Solid-state properties of materials of the type Cs_4MX_6 (where M = Sn or Pb and X = Cl or Br). *J. Chem. Soc., Dalton Trans.* **1983**, No. 4, 767.

(45) Juhas, P.; Davis, T.; Farrow, C. L.; Billinge, S. J. L. PDFgetX3: a rapid and highly automatable program for processing powder diffraction data into total scattering pair distribution functions. *J. Appl. Crystallogr.* **2013**, *46* (2), 560−566.

(46) Harris, R. K.; Becker, E. D.; Cabral de Menezes, S. M.; Goodfellow, R.; Granger, P. NMR nomenclature. *Nuclear spin properties and conventions for chemical shifts(IUPAC Recommendations 2001)*. **2001**, *73* (11), 1795−1818.

(47) Giannozzi, P.; Baroni, S.; Bonini, N.; Calandra, M.; Car, R.; Cavazzoni, C.; Ceresoli, D.; Chiarotti, G. L.; Cococcioni, M.; Dabo, I.; et al. QUANTUM ESPRESSO: a modular and open-source software project for quantum simulations of materials. *J. Phys.: Condens. Matter* **2009**, *21* (39), 395502.

(48) Giannozzi, P.; Andreussi, O.; Brumme, T.; Bunau, O.; Buongiorno Nardelli, M.; Calandra, M.; Car, R.; Cavazzoni, C.; Ceresoli, D.; Cococcioni, M.; et al. Advanced capabilities for materials modelling with Quantum ESPRESSO. *J. Phys.: Condens. Matter* **2017**, *29* (46), 465901.

(49) Hamann, D. R. Optimized norm-conserving Vanderbilt pseudopotentials. *Phys. Rev. B* **2013**, *88* (8), 085117.

(50) Perdew, J. P.; Ruzsinszky, A.; Csonka, G. I.; Vydrov, O. A.; Scuseria, G. E.; Constantin, L. A.; Zhou, X.; Burke, K. Restoring the

Density-Gradient Expansion for Exchange in Solids and Surfaces. *Phys. Rev. Lett.* **2008**, *100* (13), 136406.

(51) Zhao, X.-G.; Dalpian, G. M.; Wang, Z.; Zunger, A. Polymorphous nature of cubic halide perovskites. *Phys. Rev. B* **2020**, *101* (15), 155137.

(52) Zacharias, M.; Volonakis, G.; Giustino, F.; Even, J. Anharmonic electron-phonon coupling in ultrasoft and locally disordered perovskites. *npj Computational Materials* **2023**, *9* (1), 153.

(53) Popescu, V.; Zunger, A. Extracting *E* versus *k* effective band structure from supercell calculations on alloys and impurities. *Phys. Rev. B* **2012**, *85* (8), 085201.

(54) Zacharias, M.; Giustino, F. Theory of the special displacement method for electronic structure calculations at finite temperature. *Physical Review Research* **2020**, *2* (1), 013357.

(55) Lee, H.; Poncé, S.; Bushick, K.; Hajinazar, S.; Lafuente-Bartolome, J.; Leveillee, J.; Lian, C.; Lihm, J.-M.; Macheda, F.; Mori, H.; et al. Electron-phonon physics from first principles using the EPW code. *npj Computational Materials* **2023**, *9* (1), 156.

(56) Howard, C. J.; Stokes, H. T. Group-Theoretical Analysis of Octahedral Tilting in Perovskites. *Acta Crystallographica Section B* **1998**, *54* (6), 782−789.

(57) Baikie, T.; Barrow, N. S.; Fang, Y.; Keenan, P. J.; Slater, P. R.; Piltz, R. O.; Gutmann, M.; Mhaisalkar, S. G.; White, T. J. A combined single crystal neutron/X-ray diffraction and solid-state nuclear magnetic resonance study of the hybrid perovskites $CH_3NH_3PbX_3$ (X = I, Br and Cl). *Journal of Materials Chemistry A* **2015**, *3* (17), 9298−9307.

(58) Lanigan-Atkins, T.; He, X.; Krogstad, M. J.; Pajerowski, D. M.; Abernathy, D. L.; Xu, G. N. M. N.; Xu, Z.; Chung, D. Y.; Kanatzidis, M. G.; Rosenkranz, S.; et al. Two-dimensional overdamped fluctuations of the soft perovskite lattice in $CsPbBr_3$. *Nat. Mater.* **2021**, *20* (7), 977−983.

(59) Pisanu, A.; Mahata, A.; Mosconi, E.; Patrini, M.; Quadrelli, P.; Milanese, C.; De Angelis, F.; Malavasi, L. Exploring the Limits of Three-Dimensional Perovskites: The Case of $FAPb_{1-x}Sn_xBr_3$. *ACS Energy Letters* **2018**, *3* (6), 1353−1359.

(60) Thiele, G.; Rotter, H. W.; Schmidt, K. D. Die Kristallstrukturen und Phasentransformationen von $RbGeBr_3$. *Zeitschrift für anorganische und allgemeine Chemie* **1988**, *559* (1), 7−16.

(61) Thiele, G.; Rotter, H. W.; Schmidt, K. D. Kristallstrukturen und Phasentransformationen von Caesiumtrihalogenogermanaten(II) $CsGeX_3$ (X = Cl, Br, I). *Zeitschrift fr anorganische und allgemeine Chemie* **1987**, *545* (2), 148−156.

(62) Lü, X.; Stoumpos, C.; Hu, Q.; Ma, X.; Zhang, D.; Guo, S.; Hoffman, J.; Bu, K.; Guo, X.; Wang, Y. Regulating off-centering distortion maximizes photoluminescence in halide perovskites. *National Science Review* **2021**, *8* (9), nwaa288.

(63) Stoumpos, C. C.; Frazer, L.; Clark, D. J.; Kim, Y. S.; Rhim, S. H.; Freeman, A. J.; Ketterson, J. B.; Jang, J. I.; Kanatzidis, M. G. Hybrid Germanium Iodide Perovskite Semiconductors: Active Lone Pairs, Structural Distortions, Direct and Indirect Energy Gaps, and Strong Nonlinear Optical Properties. *J. Am. Chem. Soc.* **2015**, *137* (21), 6804−6819.

(64) Liu, Y.; Gong, Y. P.; Geng, S.; Feng, M. L.; Manidaki, D.; Deng, Z.; Stoumpos, C. C.; Canepa, P.; Xiao, Z.; Zhang, W. X. Hybrid Germanium Bromide Perovskites with Tunable Second Harmonic Generation. *Angew. Chem., Int. Ed.* **2022**, *61* (43), e202208875.

(65) Depmeier, W.; Moller, A.; Klaska, K.-H. The structure of antiferroelectric tetramethylammonium trichlorogermanate(II) at room temperature. *Acta Crystallographica Section B* **1980**, *36* (4), 803−807.

(66) Thiele, G.; Serr, B. R. Crystal structure of dimethylammonium tribromostannate(II), $(CH_3)_2NH_2SnBr_3$. *Zeitschrift für Kristallographie - Crystalline Materials* **1996**, *211* (1), 47−47.

(67) Thiele, G.; Serr, B. R. Crystal structure of trimethylammonium tribromostannate(II), $(CH_3)_3NHSnBr_3$. *Z. Kristallogr.* **1996**, *211* (1), 46−46.

(68) Dang, Y.; Zhong, C.; Zhang, G.; Ju, D.; Wang, L.; Xia, S.; Xia, H.; Tao, X. Crystallographic Investigations into Properties of Acentric

(69) Szafrański, M.; Ståhl, K. Crystal structure and phase transitions in perovskite-like $C(NH_2)_3SnCl_3$. *J. Solid State Chem.* **2007**, *180* (8), 2209−2215.

(70) Yamada, K.; Kuranaga, Y.; Ueda, K.; Goto, S.; Okuda, T.; Furukawa, Y. Phase Transition and Electric Conductivity of ASnCl3 (A = Cs and CH3NH3). *Bull. Chem. Soc. Jpn.* **1998**, *71* (1), 127−134.

(71) Varignon, J.; Bristowe, N. C.; Bousquet, E.; Ghosez, P. Coupling and electrical control of structural, orbital and magnetic orders in perovskites. *Sci. Rep.* **2015**, *5* (1), 15364.

(72) Saparov, B.; Mitzi, D. B. Organic-Inorganic Perovskites: Structural Versatility for Functional Materials Design. *Chem. Rev.* **2016**, *116* (7), 4558−4596.

(73) Kieslich, G.; Sun, S.; Cheetham, A. K. Solid-state principles applied to organic-inorganic perovskites: new tricks for an old dog. *Chemical Science* **2014**, *5* (12), 4712−4715.

(74) Coduri, M.; Shiell, T. B.; Strobel, T. A.; Mahata, A.; Cova, F.; Mosconi, E.; De Angelis, F.; Malavasi, L. Origin of pressure-induced band gap tuning in tin halide perovskites. *Materials Advances* **2020**, *1* (8), 2840−2845.

(75) Yagyu, H.; Katagami, S. Effect of Cs partial substitution on crystal systems and bandgap values of MASnCl3. *Physica B: Condensed Matter* **2022**, *633*, 413784.

(76) Laurita, G.; Fabini, D. H.; Stoumpos, C. C.; Kanatzidis, M. G.; Seshadri, R. Chemical tuning of dynamic cation off-centering in the cubic phases of hybrid tin and lead halide perovskites. *Chemical Science* **2017**, *8* (8), 5628−5635.

(77) Fabini, D. H.; Laurita, G.; Bechtel, J. S.; Stoumpos, C. C.; Evans, H. A.; Kontos, A. G.; Raptis, Y. S.; Falaras, P.; Van der Ven, A.; Kanatzidis, M. G.; et al. Dynamic Stereochemical Activity of the Sn^{2+} Lone Pair in Perovskite $CsSnBr_3$. *J. Am. Chem. Soc.* **2016**, *138* (36), 11820−11832.

(78) Knox, K. R.; Bozin, E. S.; Malliakas, C. D.; Kanatzidis, M. G.; Billinge, S. J. L. Local off-centering symmetry breaking in the high-temperature regime of SnTe. *Phys. Rev. B* **2014**, *89* (1), 014102.

(79) Yu, R.; Bozin, E. S.; Abeykoon, M.; Sangiorgio, B.; Spaldin, N. A.; Malliakas, C. D.; Kanatzidis, M. G.; Billinge, S. J. L. Emphanitic anharmonicity in PbSe at high temperature and anomalous electronic properties in the PbQ (Q= S, Se, Te) system. *Phys. Rev. B* **2018**, *98* (14), 144108.

(80) Xie, H.; Bozin, E. S.; Li, Z.; Abeykoon, M.; Banerjee, S.; Male, J. P.; Snyder, G. J.; Wolverton, C.; Billinge, S. J. L.; Kanatzidis, M. G. Hidden Local Symmetry Breaking in Silver Diamondoid Compounds is Root Cause of Ultralow Thermal Conductivity. *Adv. Mater.* **2022**, *34* (24), 2202255.

(81) Morana, M.; Wiktor, J.; Coduri, M.; Chiara, R.; Giacobbe, C.; Bright, E. L.; Ambrosio, F.; De Angelis, F.; Malavasi, L. Cubic or Not Cubic? Combined Experimental and Computational Investigation of the Short-Range Order of Tin Halide Perovskites. *J. Phys. Chem. Lett.* **2023**, *14* (8), 2178−2186.

(82) Kubicki, D. J.; Stranks, S. D.; Grey, C. P.; Emsley, L. NMR spectroscopy probes microstructure, dynamics and doping of metal halide perovskites. *Nature Reviews Chemistry* **2021**, *5* (9), 624−645.

(83) Dahlman, C. J.; Kubicki, D. J.; Reddy, G. N. M. Interfaces in metal halide perovskites probed by solid-state NMR spectroscopy. *Journal of Materials Chemistry A* **2021**, *9* (35), 19206−19244.

(84) Raval, P.; Akhavan Kazemi, M. A.; Ruellou, J.; Trébosc, J.; Lafon, O.; Delevoye, L.; Sauvage, F.; Manjunatha Reddy, G. N. Examining a Year-Long Chemical Degradation Process and Reaction Kinetics in Pristine and Defect-Passivated Lead Halide Perovskites. *Chem. Mater.* **2023**, *35* (7), 2904−2917.

(85) Spanopoulos, I.; Hadar, I.; Ke, W.; Guo, P.; Mozur, E. M.; Morgan, E.; Wang, S.; Zheng, D.; Padgaonkar, S.; Manjunatha Reddy, G. N.; et al. Tunable Broad Light Emission from 3D "Hollow" Bromide Perovskites through Defect Engineering. *J. Am. Chem. Soc.* **2021**, *143* (18), 7069−7080.

(86) Kubicki, D. J.; Prochowicz, D.; Salager, E.; Rakhmatullin, A.; Grey, C. P.; Emsley, L.; Stranks, S. D. Local Structure and Dynamics

in Methylammonium, Formamidinium, and Cesium Tin(II) Mixed-Halide Perovskites from ^{119}Sn Solid-State NMR. *J. Am. Chem. Soc.* **2020**, *142* (17), 7813−7826.

(87) Fu, P.; Quintero, M. A.; Vasileiadou, E. S.; Raval, P.; Welton, C.; Kepenekian, M.; Volonakis, G.; Even, J.; Liu, Y.; Malliakas, C.; et al. Chemical Behavior and Local Structure of the Ruddlesden-Popper and Dion-Jacobson Alloyed Pb/Sn Bromide 2D Perovskites. *J. Am. Chem. Soc.* **2023**, *145* (29), 15997−16014.

(88) Karmakar, A.; Mukhopadhyay, S.; Gachod, P. G. B.; Mora-Gomez, V. A.; Bernard, G. M.; Brown, A.; Michaelis, V. K. Uncovering Halogen Mixing and Octahedral Dynamics in Cs$_2$SnX$_6$ by Multinuclear Magnetic Resonance Spectroscopy. *Chem. Mater.* **2021**, *33* (15), 6078−6090.

(89) Karmakar, A.; Bhattacharya, A.; Sarkar, D.; Bernard, G. M.; Mar, A.; Michaelis, V. K. Influence of hidden halogen mobility on local structure of CsSn(Cl$_{1-x}$Br$_x$)$_3$ mixed-halide perovskites by solid-state NMR. *Chemical Science* **2021**, *12* (9), 3253−3263.

(90) Ha, M.; Karmakar, A.; Bernard, G. M.; Basilio, E.; Krishnamurthy, A.; Askar, A. M.; Shankar, K.; Kroeker, S.; Michaelis, V. K. Phase Evolution in Methylammonium Tin Halide Perovskites with Variable Temperature Solid-State 119Sn NMR Spectroscopy. *J. Phys. Chem. C* **2020**, *124* (28), 15015−15027.

(91) Eichler, B. E.; Power, P. P. Characterization of the Sterically Encumbered Terphenyl-Substituted Species 2,6-Trip$_2$H$_3$C$_6$Sin-Sn-(Me)$_2$C$_6$H$_3$-2,6-Trip$_2$, an Unsymmetric, Group 14 Element, Methyl-methylene, Valence Isomer of an Alkene, Its Related Lithium Derivative 2,6-Trip$_2$H$_3$C$_6$(Me)$_2$Sn-Sn(Li)(Me)C$_6$H$_3$-2,6-Trip$_2$, and the Monomer Sn(*t*-Bu)C$_6$H$_3$-2,6-Trip$_2$ (Trip = C$_6$H$_2$-2,4,6-*i*-Pr$_3$). *Inorg. Chem.* **2000**, *39* (24), 5444−5449.

(92) Stückrath, J. B.; Gasevic, T.; Bursch, M.; Grimme, S. Benchmark Study on the Calculation of ^{119}Sn NMR Chemical Shifts. *Inorg. Chem.* **2022**, *61* (9), 3903−3917.

(93) Raval, P.; Kennard, R. M.; Vasileiadou, E. S.; Dahlman, C. J.; Spanopoulos, I.; Chabinyc, M. L.; Kanatzidis, M.; Manjunatha Reddy, G. N. Understanding Instability in Formamidinium Lead Halide Perovskites: Kinetics of Transformative Reactions at Grain and Subgrain Boundaries. *ACS Energy Letters* **2022**, *7* (4), 1534−1543.

(94) Kortüm, G.; Braun, W.; Herzog, G. Principles and Techniques of Diffuse-Reflectance Spectroscopy. *Angewandte Chemie International Edition in English* **1963**, *2*, 333−341.

(95) Liu, Y.; Cai, B.; Yang, H.; Boschloo, G.; Johansson, E. M. J. Solvent Engineering of Perovskite Crystallization for High Band Gap FAPbBr$_3$ Perovskite Solar Cells Prepared in Ambient Condition. *ACS Applied Energy Materials* **2023**, *6* (13), 7102−7108.

(96) Spanopoulos, I.; Ke, W.; Stoumpos, C. C.; Schueller, E. C.; Kontsevoi, O. Y.; Seshadri, R.; Kanatzidis, M. G. Unraveling the Chemical Nature of the 3D "Hollow" Hybrid Halide Perovskites. *J. Am. Chem. Soc.* **2018**, *140* (17), 5728−5742.

(97) Yu, Z.; Leilaeioun, M.; Holman, Z. Selecting tandem partners for silicon solar cells. *Nature Energy* **2016**, *1* (11), 16137.

(98) Straus, D. B.; Cava, R. J. Tuning the Band Gap in the Halide Perovskite CsPbBr$_3$ through Sr Substitution. *ACS Appl. Mater. Interfaces* **2022**, *14* (30), 34884−34890.

(99) Heo, J.-M.; Cho, H.; Lee, S.-C.; Park, M.-H.; Kim, J. S.; Kim, H.; Park, J.; Kim, Y.-H.; Yun, H. J.; Yoon, E.; et al. Bright Lead-Free Inorganic CsSnBr$_3$ Perovskite Light-Emitting Diodes. *ACS Energy Letters* **2022**, *7* (8), 2807−2815.

(100) Ibaceta-Jaña, J.; Muydinov, R.; Rosado, P.; Mirhosseini, H.; Chugh, M.; Nazarenko, O.; Dirin, D. N.; Heinrich, D.; Wagner, M. R.; Kühne, T. D.; et al. Vibrational dynamics in lead halide hybrid perovskites investigated by Raman spectroscopy. *Phys. Chem. Chem. Phys.* **2020**, *22* (10), 5604−5614.

(101) Létoublon, A.; Paofai, S.; Rufflé, B.; Bourges, P.; Hehlen, B.; Michel, T.; Ecolivet, C.; Durand, O.; Cordier, S.; Katan, C.; et al. Elastic Constants, Optical Phonons, and Molecular Relaxations in the High Temperature Plastic Phase of the CH3NH3PbBr3 Hybrid Perovskite. *J. Phys. Chem. Lett.* **2016**, *7* (19), 3776−3784.

(102) Yaffe, O.; Guo, Y.; Tan, L. Z.; Egger, D. A.; Hull, T.; Stoumpos, C. C.; Zheng, F.; Heinz, T. F.; Kronik, L.; Kanatzidis, M. G.; et al. Local Polar Fluctuations in Lead Halide Perovskite Crystals. *Phys. Rev. Lett.* **2017**, *118* (13), 136001.

(103) Damle, V. H.; Gouda, L.; Tirosh, S.; Tischler, Y. R. Structural Characterization and Room Temperature Low-Frequency Raman Scattering from MAPbI3 Halide Perovskite Films Rigidized by Cesium Incorporation. *ACS Applied Energy Materials* **2018**, *1* (12), 6707−6713.

(104) Badrooj, M.; Jamali-Sheini, F.; Torabi, N. Optoelectronic Properties of Mixed Sn/Pb Perovskite Solar Cells: The Study of Compressive Strain by Raman Modes. *J. Phys. Chem. C* **2020**, *124* (49), 27136−27147.

(105) Gao, L.; Yadgarov, L.; Sharma, R.; Korobko, R.; McCall, K. M.; Fabini, D. H.; Stoumpos, C. C.; Kanatzidis, M. G.; Rappe, A. M.; Yaffe, O. Metal cation s lone-pairs increase octahedral tilting instabilities in halide perovskites. *Materials Advances* **2021**, *2* (14), 4610−4616.

(106) Huang, L.-y.; Lambrecht, W. R. L. Vibrational spectra and nonlinear optical coefficients of rhombohedral CsGeX$_3$ halide compounds with X = I, Br, Cl. *Phys. Rev. B* **2016**, *94* (11), 115202.

(107) Motti, S. G.; Patel, J. B.; Oliver, R. D. J.; Snaith, H. J.; Johnston, M. B.; Herz, L. M. Phase segregation in mixed-halide perovskites affects charge-carrier dynamics while preserving mobility. *Nat. Commun.* **2021**, *12* (1), 6955.

(108) Lin, Y.; Chen, B.; Fang, Y.; Zhao, J.; Bao, C.; Yu, Z.; Deng, Y.; Rudd, P. N.; Yan, Y.; Yuan, Y.; et al. Excess charge-carrier induced instability of hybrid perovskites. *Nat. Commun.* **2018**, *9* (1), 4981.

(109) Kim, D.; Jung, H. J.; Park, I. J.; Larson, B. W.; Dunfield, S. P.; Xiao, C.; Kim, J.; Tong, J.; Boonmongkolras, P.; Ji, S. G.; et al. Efficient, stable silicon tandem cells enabled by anion-engineered wide-bandgap perovskites. *Science* **2020**, *368* (6487), 155−160.

(110) Cacovich, S.; Messou, D.; Bercegol, A.; Béchu, S.; Yaiche, A.; Shafique, H.; Rousset, J.; Schulz, P.; Bouttemy, M.; Lombez, L. Light-Induced Passivation in Triple Cation Mixed Halide Perovskites: Interplay between Transport Properties and Surface Chemistry. *ACS Appl. Mater. Interfaces* **2020**, *12* (31), 34784−34794.

(111) Motti, S. G.; Gandini, M.; Barker, A. J.; Ball, J. M.; Srimath Kandada, A. R.; Petrozza, A. Photoinduced Emissive Trap States in Lead Halide Perovskite Semiconductors. *ACS Energy Letters* **2016**, *1* (4), 726−730.

(112) Wang, Z.; Lin, Q.; Chmiel, F. P.; Sakai, N.; Herz, L. M.; Snaith, H. J. Efficient ambient-air-stable solar cells with 2D-3D heterostructured butylammonium-caesium-formamidinium lead halide perovskites. *Nature Energy* **2017**, *2* (9), 17135.

(113) Wang, Z.; Zeng, L.; Zhu, T.; Chen, H.; Chen, B.; Kubicki, D. J.; Balvanz, A.; Li, C.; Maxwell, A.; Ugur, E.; et al. Suppressed phase segregation for triple-junction perovskite solar cells. *Nature* **2023**, *618* (7963), 74−79.

(114) Prasanna, R.; Gold-Parker, A.; Leijtens, T.; Conings, B.; Babayigit, A.; Boyen, H.-G.; Toney, M. F.; McGehee, M. D. Band Gap Tuning via Lattice Contraction and Octahedral Tilting in Perovskite Materials for Photovoltaics. *J. Am. Chem. Soc.* **2017**, *139* (32), 11117−11124.

Supporting Information

Structural Evolution and Photoluminescence Quenching Across the FASnI$_{3-x}$Br$_x$ ($x = 0 - 3$) Perovskites

Adam Balvanz,[1] Majid Safdari,[1,2*] Marios Zacharias,[3] Daehan Kim,[1] Claire Welton,[4] Evan H. Oriel,[1] Mikaël Kepenekian,[5] Claudine Katan,[5] Christos D. Malliakas,[1] Jacky Even,[3] Vladislav Klepov,[1,6] G.N. Manjunatha Reddy,[4] Richard D. Schaller,[1,7] Lin X. Chen,[1,8] Ram Seshadri,[9] and Mercouri G. Kanatzidis[1*]

[1]Northwestern University Department of Chemistry, Evanston, IL 60208 USA

[2]Department of Chemistry, Division of Applied Physical Chemistry, KTH Royal Institute of Technology, SE-100 44 Stockholm, Sweden

[3] Univ Rennes, INSA Rennes, CNRS, Institute FOTON – UMR 6082, Rennes F-35000, France

[4]University of Lille, CNRS, Centrale Lille, Univ. Artois, UMR 8181 – UCCS – Unité de Catalyse et Chimie du Solide, Lille F-59000, France

[5]Univ Rennes, INSA Rennes, CNRS, ISCR – UMR 6226, Rennes F-35000, France

[6]University of Georgia Department of Chemistry, Athens, GA 30602 USA

[7]Center for Nanoscale Materials, Argonne National Laboratory, Lemont, IL 60439 USA

[8]Materials Science Division, Argonne National Laboratory, Lemont, IL 60439 USA

[9]Materials Department and Materials Research Laboratory, University of California, Santa Barbara, CA 93106, USA

*Correspondence: m-kanatzidis@northwestern.edu; majid.safdari@northwestern.edu

Table of Contents:

Additional Experimental Methods (pg. 4-9)

Supplementary Figures (pg. 10 – 25)

Supplementary Tables: (pg. 26 – 34)

References (pg. 36)

Additional Synthetic Procedures for FASnI$_{3-x}$Br$_x$ (x= 0 – 3) Compounds:

Synthesis of FASnI$_3$: 677 mg (3 mmol) of SnCl$_2$·2H$_2$O (Sigma-Aldrich; 98 wt.%) was massed and placed into a 20 mL scintillation vial. 5 mL of HI (Sigma-Aldrich; 57 wt.% in H$_2$O) and 1.7 mL of H$_3$PO$_2$ (Sigma-Aldrich; 50 wt.% in H$_2$O) was added to the solid along with a magnetic stir bar. The vial was heated on a hotplate (~120°C) under constant stirring until all of the solids dissolved and a clear solution was achieved. 312 mg (3 mmol) of FACH$_3$COO (TCI; >98 wt.%) was then added to the hot reaction solution followed by immediate precipitation of a black solid. The temperature was then increased to ~210°C where the precipitate redissolved, creating a clear solution. The hotplate was then set to 110°C and cooled to room temperature at a rate of 10°C/hr. Crystals of FASnI$_3$ were then isolated as black crystals from the solution.

Synthesis of FASnI$_{2.6}$Br$_{0.4}$: 677 mg (3 mmol) of SnCl$_2$·2H$_2$O (Sigma-Aldrich; 98 wt.%) was massed and placed into a 20 mL scintillation vial. 3.3 mL of HI (Sigma-Aldrich; 57 wt.% in H$_2$O), 1.7 mL (Sigma-Aldrich; 48 wt% in H$_2$O), and 1.7 mL of H$_3$PO$_2$ (Sigma-Aldrich; 50 wt.% in H$_2$O) was added to the solid along with a magnetic stir bar. The vial was heated on a hotplate (~120°C) under constant stirring until all of the solids dissolved and a clear solution was achieved. 312 mg (3 mmol) of FACH$_3$COO (TCI; >98 wt.%) was then added to the hot reaction solution followed by immediate precipitation of a black solid. The temperature was then increased to ~210°C where the precipitate redissolved, creating a clear solution. The hotplate was then set to 110°C and cooled to room temperature at a rate of 10°C/hr. Crystals of FASnI$_{2.6}$Br$_{0.4}$ were then isolated as black crystals from the solution.

Synthesis of FASnI$_{2.3}$Br$_{0.7}$: 677 mg (3 mmol) of SnCl$_2$·2H$_2$O (Sigma-Aldrich; 98 wt.%) was massed and placed into a 20 mL scintillation vial. 1.7 mL of HI (Sigma-Aldrich; 57 wt.% in H$_2$O), 3.3 mL (Sigma-Aldrich; 48 wt% in H$_2$O), and 1.7 mL of H$_3$PO$_2$ (Sigma-Aldrich; 50 wt.% in H$_2$O) was added to the solid along with a magnetic stir bar. The vial was heated on a hotplate (~120°C) under constant stirring until all of the solids dissolved and a clear solution was achieved. 312 mg (3 mmol) of FACH$_3$COO (TCI; >98 wt.%) was then added to the hot reaction solution followed by immediate precipitation of a black solid. The temperature was then increased to ~210°C where the precipitate redissolved, creating a clear solution. The hotplate was then set to 110°C and cooled

to room temperature at a rate of 10°C/hr. Crystals of FASnI$_{2.3}$Br$_{0.7}$ were then isolated as black crystals from the solution.

Synthesis of FASnI$_{2.1}$Br$_{0.9}$: 451 mg (2 mmol) of SnCl$_2$·2H$_2$O (Sigma-Aldrich; 98 wt.%) was massed out and placed into a 20 mL scintillation vial. 2.25 mL of HBr (Sigma-Aldrich; 48 wt.% in H$_2$O), 0.75 mL of HI (Sigma-Aldrich 57 wt.% in H$_2$O), and 0.75 mL of H$_3$PO$_2$ (Sigma-Aldrich; 50 wt.% in H$_2$O) was added to the vial along with a magnetic stir bar. SnCl$_2$·2H$_2$O was intended to be the limiting reagent during the reaction. The vial was heated on a hotplate (~120°C) under constant stirring until all solids dissolved creating a clear solution. 312 mg (3 mmol) of FACH$_3$COO (TCI; >98 wt.%) was then added to the hot reaction solution followed by immediate precipitation of a black solid. The temperature was then increased to ~210°C where the precipitate redissolved, creating a clear solution. Stirring continued for ~5 minutes before the hotplate was shut off, the stir bar was removed, and the reaction was allowed to cool to room temperature on the hotplate. Crystals of FASnI$_{2.1}$Br$_{0.9}$were then isolated as black crystals from the solution.

Synthesis of FASnI$_{1.9}$Br$_{1.1}$: 451 mg (2 mmol) of SnCl$_2$·2H$_2$O (Sigma-Aldrich; 98 wt.%) was massed out and placed into a 20 mL scintillation vial. 2 mL of HBr (Sigma-Aldrich; 48 wt.% in H$_2$O), 1 mL of HI (Sigma-Aldrich 57 wt.% in H$_2$O), and 0.75 mL of H$_3$PO$_2$ (Sigma-Aldrich; 50 wt.% in H$_2$O) was added to the vial along with a magnetic stir bar. SnCl$_2$·2H$_2$O was intended to be the limiting reagent during the reaction. The vial was heated on a hotplate (~120°C) under constant stirring until all solids dissolved creating a clear solution. 312 mg (3 mmol) of FACH$_3$COO (TCI; >98 wt.%) was then added to the hot reaction solution followed by immediate precipitation of a black solid. The temperature was then increased to ~210°C where the precipitate redissolved, creating a clear solution. Stirring continued for ~5 minutes before the hotplate was shut off, the stir bar was removed, and the reaction was allowed to cool to room temperature on the hotplate. Crystals of FASnI$_{1.9}$Br$_{1.1}$were then isolated as black crystals from the solution.

Synthesis of FASnI$_{1.1}$Br$_{1.9}$: 451 mg (2 mmol) of SnCl$_2$·2H$_2$O (Sigma-Aldrich; 98 wt.%) was massed out and placed into a 20 mL scintillation vial. 2.5 mL of HBr (Sigma-Aldrich; 48 wt.% in H$_2$O), 0.5 mL of HI (Sigma-Aldrich 57 wt.% in H$_2$O), and 0.75 mL of H$_3$PO$_2$ (Sigma-Aldrich; 50 wt.% in H$_2$O) was added to the vial along with a magnetic stir bar. SnCl$_2$·2H$_2$O was intended to

be the limiting reagent during the reaction. The vial was heated on a hotplate (~120°C) under constant stirring until all solids dissolved creating a clear solution. 312 mg (3 mmol) of $FACH_3COO$ (TCI; >98 wt.%) was then added to the hot reaction solution followed by immediate precipitation of a black solid. The temperature was then increased to ~210°C where the precipitate redissolved, creating a clear solution. Stirring continued for ~5 minutes before the hotplate was shut off, the stir bar was removed, and the reaction was allowed to cool to room temperature on the hotplate. Crystals of $FASnI_{1.1}Br_{1.9}$ were then isolated as black crystals from the solution.

Synthesis of $FASnI_{0.7}Br_{2.3}$: 451 mg (2 mmol) of $SnCl_2 \cdot 2H_2O$ (Sigma-Aldrich; 98 wt.%) was massed out and placed into a 20 mL scintillation vial. 2.75 mL of HBr (Sigma-Aldrich; 48 wt.% in H_2O), 0.25 mL of HI (Sigma-Aldrich 57 wt.% in H_2O), and 0.75 mL of H_3PO_2 (Sigma-Aldrich; 50 wt.% in H_2O) was added to the vial along with a magnetic stir bar. $SnCl_2 \cdot 2H_2O$ was intended to be the limiting reagent during the reaction. The vial was heated on a hotplate (~120°C) under constant stirring until all solids dissolved creating a clear solution. 312 mg (3 mmol) of $FACH_3COO$ (TCI; >98 wt.%) was then added to the hot reaction solution followed by immediate precipitation of a red solid. The temperature was then increased to ~210°C where the precipitate redissolved, creating a clear solution. Stirring continued for ~5 minutes before the hotplate was shut off, the stir bar was removed, and the reaction was allowed to cool to room temperature on the hotplate. Crystals of $FASnI_{0.7}Br_{2.3}$ were then isolated as red crystals from the solution.

Synthesis of $FASnI_{0.4}Br_{2.6}$: 451 mg (2 mmol) of $SnCl_2 \cdot 2H_2O$ (Sigma-Aldrich; 98 wt.%) was massed out and placed into a 20 mL scintillation vial. 2.8 mL of HBr (Sigma-Aldrich; 48 wt.% in H_2O), 0.2 mL of HI (Sigma-Aldrich 57 wt.% in H_2O), and 0.75 mL of H_3PO_2 (Sigma-Aldrich; 50 wt.% in H_2O) was added to the vial along with a magnetic stir bar. $SnCl_2 \cdot 2H_2O$ was intended to be the limiting reagent during the reaction. The vial was heated on a hotplate (~120°C) under constant stirring until all solids dissolved creating a clear solution. 312 mg (3 mmol) of $FACH_3COO$ (TCI; >98 wt.%) was then added to the hot reaction solution followed by immediate precipitation of a red solid. The temperature was then increased to ~210°C where the precipitate redissolved, creating a clear solution. Stirring continued for ~5 minutes before the hotplate was shut off, the stir bar was removed, and the reaction was allowed to cool to room temperature on the hotplate. Crystals of $FASnI_{0.4}Br_{2.6}$ were then isolated as red-orange crystals from the solution.

Synthesis of FASnI$_{0.1}$Br$_{2.9}$: 451 mg (2 mmol) of SnCl$_2$·2H$_2$O (Sigma-Aldrich; 98 wt.%) was massed out and placed into a 20 mL scintillation vial. 2.9 mL of HBr (Sigma-Aldrich; 48 wt.% in H$_2$O), 0.1 mL of HI (Sigma-Aldrich 57 wt.% in H$_2$O), and 0.75 mL of H$_3$PO$_2$ (Sigma-Aldrich; 50 wt.% in H$_2$O) was added to the vial along with a magnetic stir bar. SnCl$_2$·2H$_2$O was intended to be the limiting reagent during the reaction. The vial was heated on a hotplate (~120°C) under constant stirring until all solids dissolved creating a clear solution. 312 mg (3 mmol) of FACH$_3$COO (TCI; >98 wt.%) was then added to the hot reaction solution followed by immediate precipitation of an orange-yellow solid. The temperature was then increased to ~210°C where the precipitate redissolved, creating a clear solution. Stirring continued for ~5 minutes before the hotplate was shut off, the stir bar was removed, and the reaction was allowed to cool to room temperature on the hotplate. Crystals of FASnI$_{0.1}$Br$_{2.9}$ were then isolated as orange-yellow crystals from the solution.

Synthesis of FASnBr$_3$: 451 mg (2 mmol) of SnCl$_2$·2H$_2$O (Sigma-Aldrich; 98 wt.%) was massed out and placed into a 20 mL scintillation vial. 3 mL of HBr (Sigma-Aldrich; 48 wt.% in H$_2$O) and 1 mL of H$_3$PO$_2$ (Sigma-Aldrich; 50 wt.% in H$_2$O) was added to the vial along with a magnetic stir bar. SnCl$_2$·2H$_2$O was intended to be the limiting reagent during the reaction. The vial was heated on a hotplate (~120°C) under constant stirring until all solids dissolved creating a clear solution. 312 mg (3 mmol) of FACH$_3$COO (TCI; >98 wt.%) was then added to the hot reaction solution followed by immediate precipitation of a yellow solid. The temperature was then increased to ~210°C where the precipitate redissolved, creating a clear solution. Stirring continued for ~5 minutes before the hotplate was shut off, the stir bar was removed, and the reaction was allowed to cool to room temperature on the hotplate. FASnBr$_3$ was then isolated as yellow crystals from the solution.

Diffuse Reflectance:

Dry, bulk materials were mechanically ground in a mortar and pestle inside a N_2 filled glovebox and then combined with varying amounts of barium sulfate ($BaSO_4$). $BaSO_4$ serves as the 100% reflectance standard for the measurements and dilutes the sample to reduce the overall absorbance such that the data could be collected in a reflection geometry. The optical diffuse reflectance data were collected on a Cary 5000 UV-Vis-NIR double beam spectrophotometer equipped with a monochromator and an integrating sphere detector. The room temperature data collection covered the range of 200 – 1100 nm. The collected data were then used to estimate the band gap of the material by first converting the reflectance data to absorption, through the use of the Kubelka-Munk transformation, and subsequently extrapolating the absorption edge of the curve.[1]

Scanning Electron Microscopy with Energy Dispersive X-ray Spectroscopy (SEM-EDS):

Scanning Electron Microscopy (SEM) analyses were performed using a Schotty field-emission SEM (JEOL JSM-7900FLV SEM) at 10 kV. Energy-dispersive X-ray spectroscopy was performed using an Oxford 65 EDS detector with a 65 mm^2 detection area.

Pair Distribution Function Calculations:

Pair distribution function analyses are a unique method allowing for a more direct understanding of the local structure of materials. Since both the Bragg reflections and diffuse scattering are weighted equally, long-range order is not a requirement unlike traditional diffraction techniques, making it ideal for structural insight into non-crystalline phases (glasses for example). PDF analyses can be crucial to understanding if perturbations in the chemical structure seen for a typical single crystal is representative of the bulk material. It can also be critical to understand distortions on a local level which are not captured in the average. The data collected for these analyses are high resolution X-ray diffraction powder diffraction patterns. The coherent part of the measured intensity $I_c(Q)$ is used to calculate the total scattering structure function for each compound $S(Q)$ (eq. 1).

$$S(Q) = \frac{I_c(Q) - \sum c_i |f_i(Q)|^2}{|\sum c_i f_i(Q)|^2} + 1 \qquad \text{eq.1}$$

Here the intensity is found by subtraction of the background from air and scattering from the glass vessel as well as accounting for several other effects. The data is also normalized against

the flux of the radiation source and number of atoms contained within the sample. Within eq. 1, c_i are the atomic concentration and $f_i(Q)$ is the X-ray atomic form factor for the atomic species of type i, and momentum transfer is determined through eq. 2.

$$Q = \frac{4\pi \sin\theta}{\lambda} \qquad \text{eq.2}$$

The atomic pair distribution function (PDF) is then obtained through a Fourier transformation of the expression $Q(S(Q)-1)$ (eq. 3)

$$G(r) = (2/\pi) \int_{Q_{min}}^{Q_{max}} Q(S(Q) - 1) \sin(Q \cdot r) dQ \qquad \text{eq.3}$$

The atomic PDF is also related to the average atomic number density (ρ_0) and the atomic pair-density ($\rho(r)$, which is a function of radial distance (r) typically in angstroms). This relation is calculated through eq. 4.

$$G(r) = 4\pi \cdot r(\rho(r) - \rho_0) \qquad \text{eq. 4}$$

$G(r)$ then provides information regarding the density of atoms residing in an infinitesimally small shell at a distance of r away from a designated reference atom. The experimental atomic PDF can then be refined against a theoretical PDF generated based on a structural model. Notably the higher the Q_{max} that can be used, the higher the resolution will be. In an ideal case $Q > 20$ Å^{-1} is desired but is entirely dependent on the structural features needed to be resolved compared to the real space resolution (δr) based on eq. 5. In this case, shorter wavelengths are more optimal based on eq. 2.

$$\delta r = \frac{2\pi}{Q_{max}} \qquad \text{eq.5}$$

Modeling of Local Structures:

The local structure of FASnI$_3$ and FASnBr$_3$ was obtained by relaxing the average crystal structure to P1 (only identity symmetry) and reducing each organic FA$^+$ cation to a centralized C atom with the same electron density. These models were then used as a starting point for refining the structure against the low r regions of the $G(r)$ curves which can be done through eq. 5.

$$G(r) + 4\pi \cdot r \cdot \rho_0 = \frac{1}{r}\sum_v \sum_\mu \frac{f(0)_v f(0)_\mu}{\langle f(0)\rangle^2} \delta(r - r_{v\mu}) \qquad \text{eq.5}$$

Refining of the local structure against the experimental PDF curve was then accomplished through PDFgui[2] by freely refining several corrective factors as well as the unit cell parameters and the positions of the atoms in the lower symmetry unit cell.
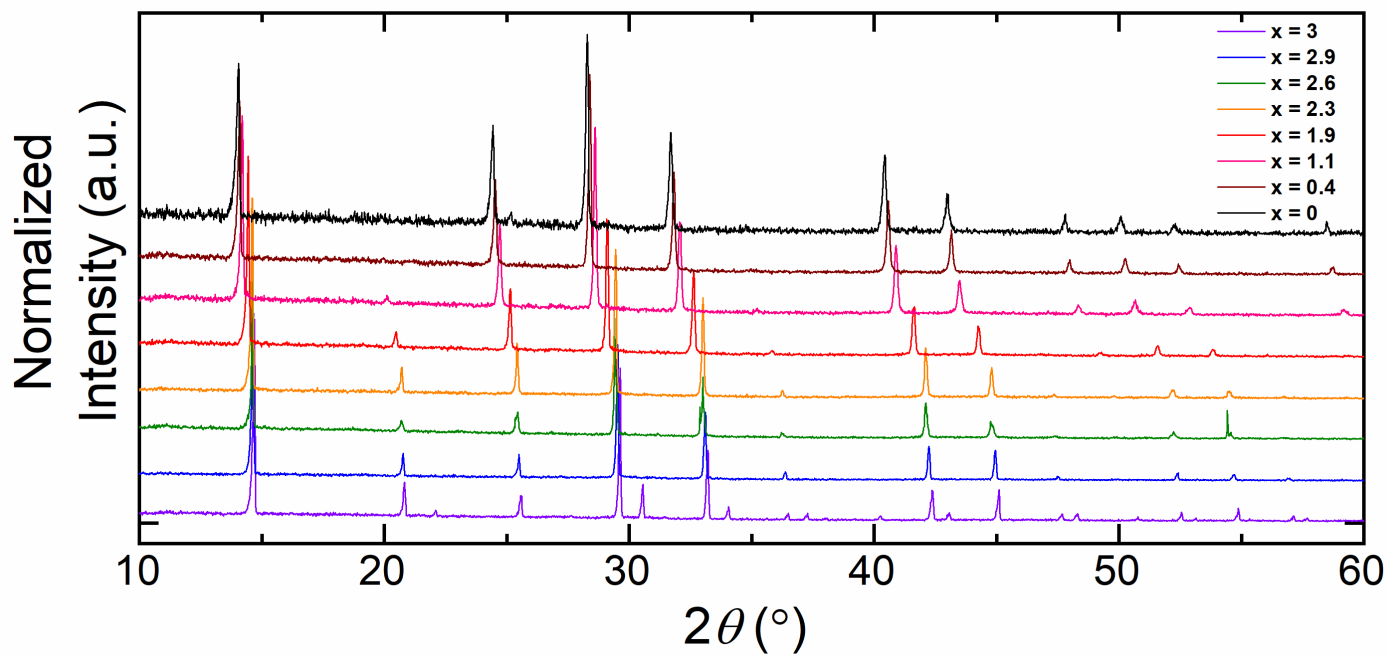
Figure S1: Selected experimental powder diffraction patterns for FASnI$_{3-x}$Br$_x$ ($x = 0 - 3$) compositions. The presented range was shortened to 10-60° 2θ due to air scattering at low angles.
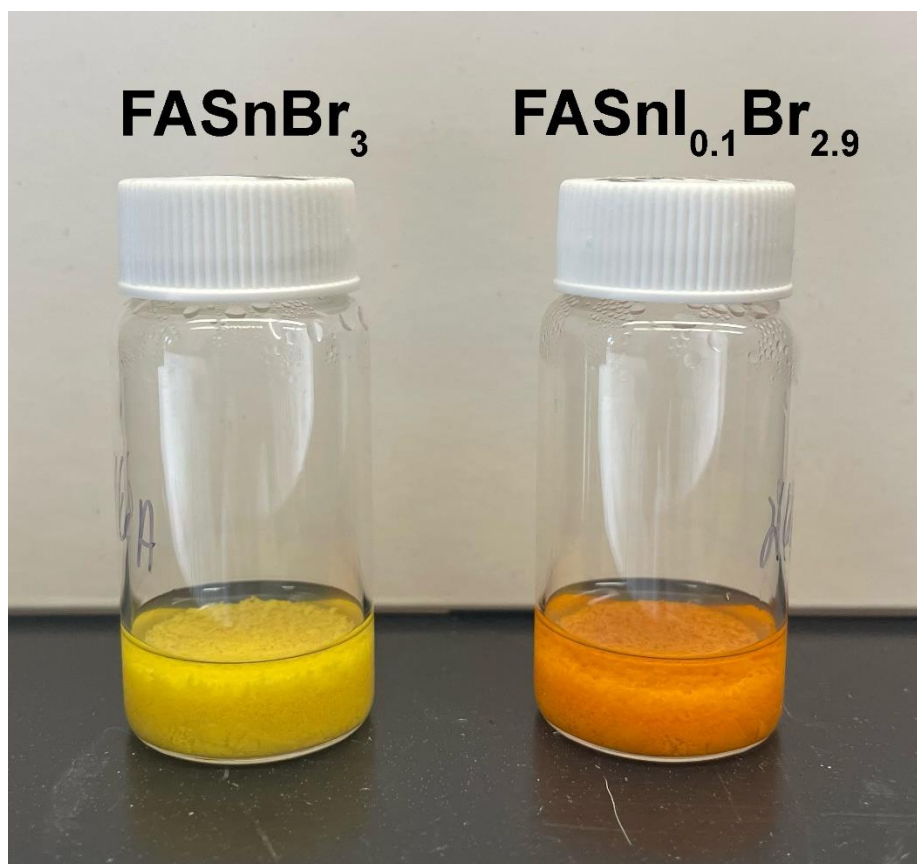
Figure S2: As synthesized crystallites of $FASnBr_3$ and $FASnI_{0.1}Br_{2.9}$. The compounds are shown on the left (yellow) and right (orange) respectively.
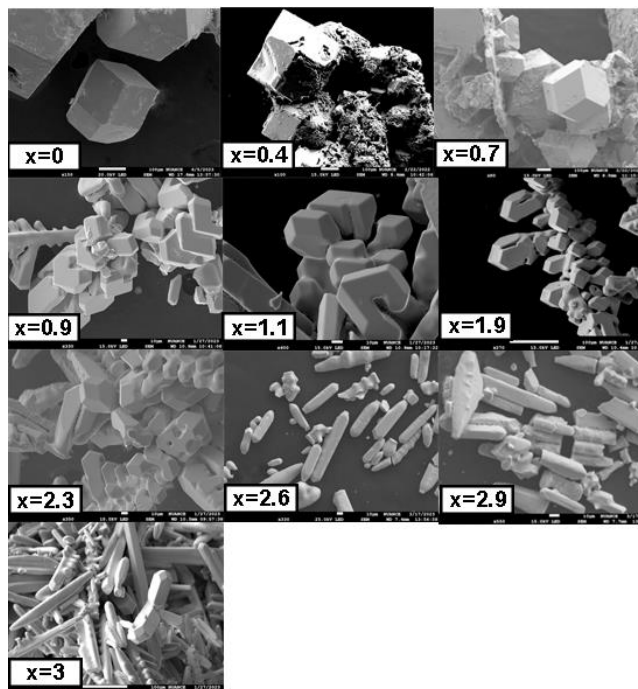
Figure S3: The crystal habit for each of the synthesized compounds in the FASnI$_{3-x}$Br$_x$ ($x = 0 - 3$) substitution range.
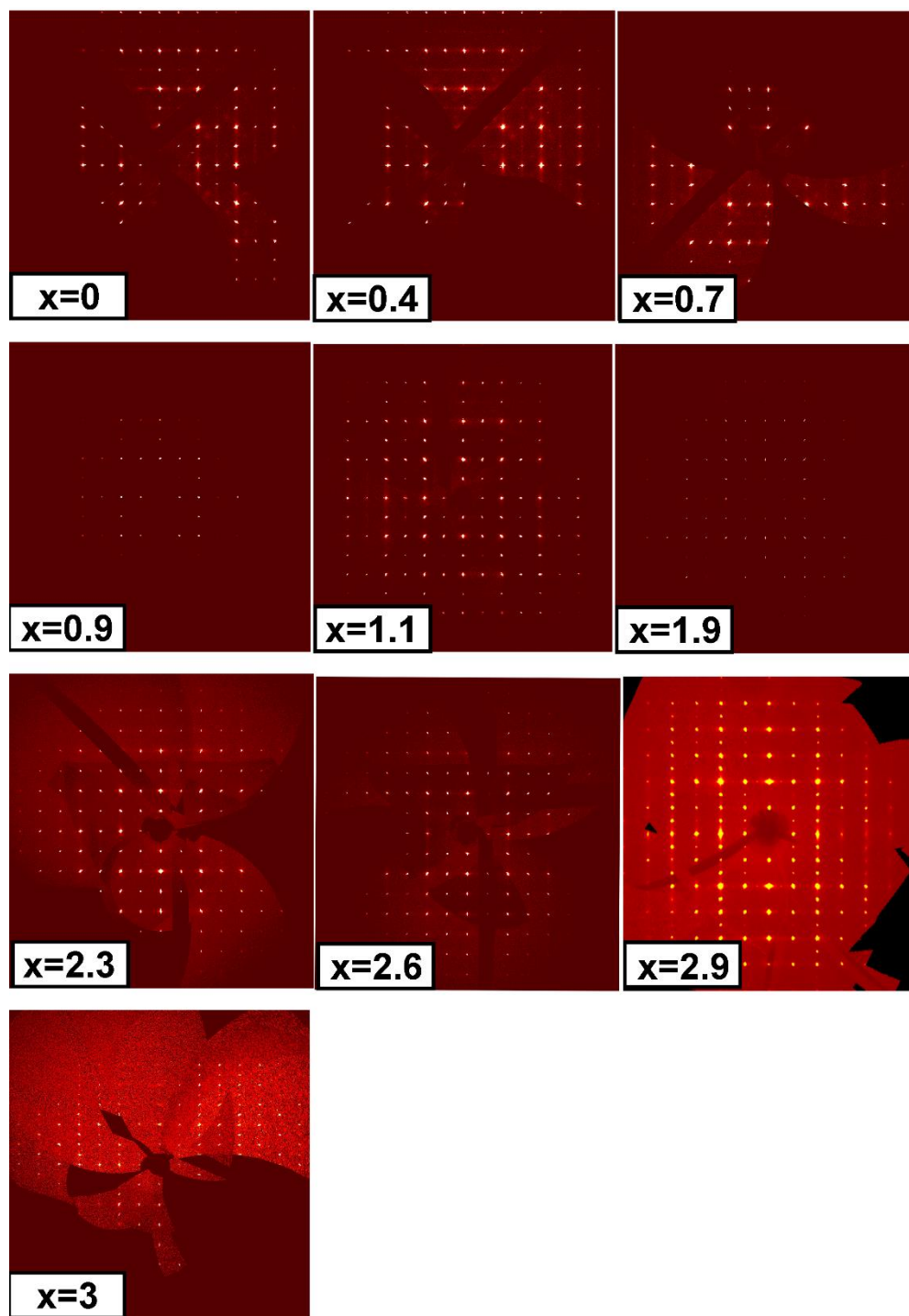
Figure S4: Precession images of reciprocal space for each of the synthesized compounds in the FASnI$_{3-x}$Br$_x$ (x = 0 − 3) family. The presence of additional reflections for the x = 2.9 and 3 compositions provides direct evidence for the structural change.
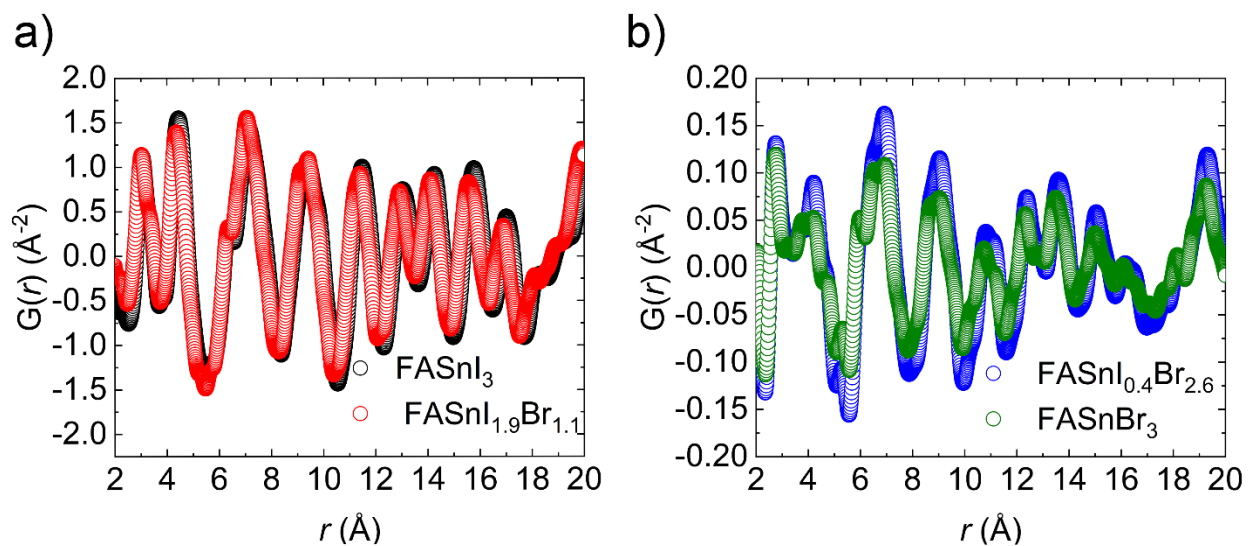
Figure S5: a) the PDF curve from 2 – 20 Å for FASnI$_3$ and FASnI$_{1.9}$ overlayed on one another and b) the PDF curve from 2 – 20 Å for FASnI$_{0.4}$Br$_{2.6}$ and FASnBr$_3$ overlayed on one another.
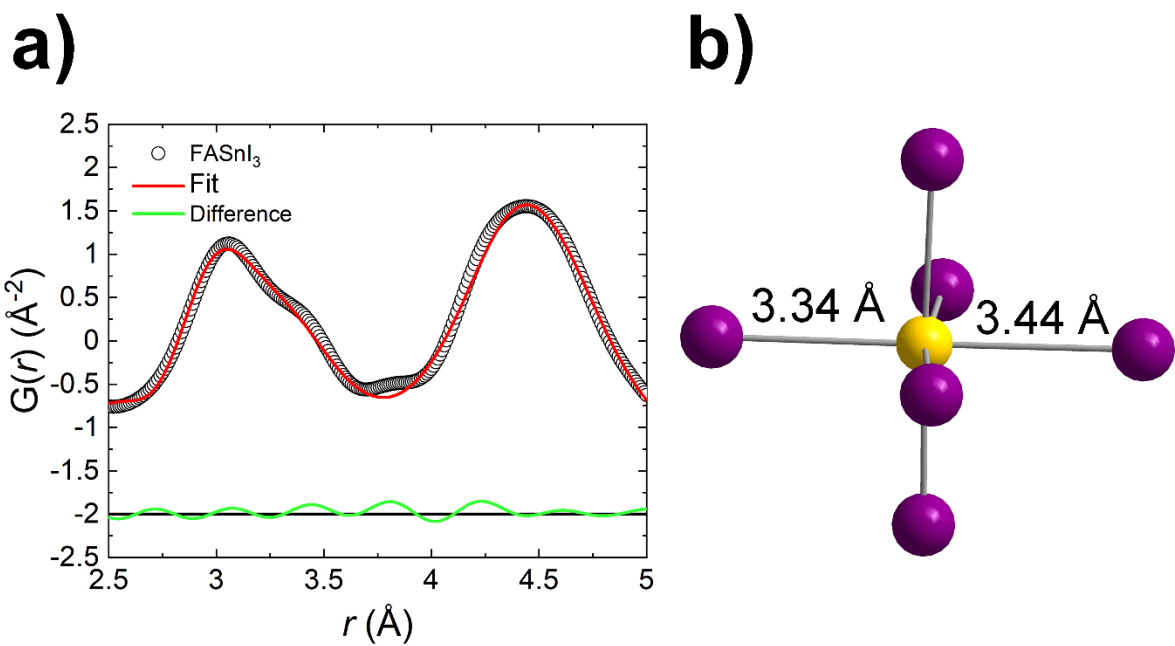
Figure S6: a) Experimental and theoretical $G(r)$ curves as well as the difference curve within the range of 2.5-5 Å. b) The SnI_6 octahedral unit based on refinements of the local structure against the $G(r)$. The off-centering of the Sn atom is highlighted by the bond distances of opposite Iodine atoms. The structrue was relaxed to P1 space group symmetry for modeling of the curve.
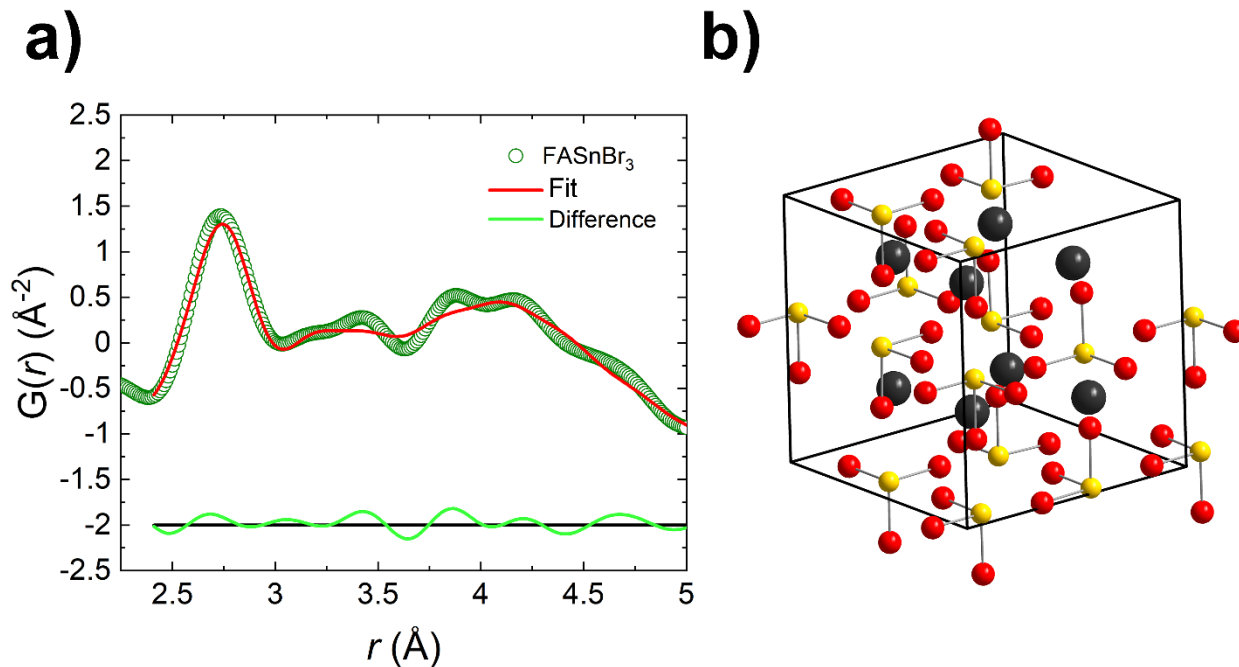
Figure S7: a) Experimental and theoretical $G(r)$ curves as well as the difference curve within the range of 2.5-5 Å. b) the refined local structure model of FASnBr$_3$. The space group symmetry was relaxed to P1 for the model.
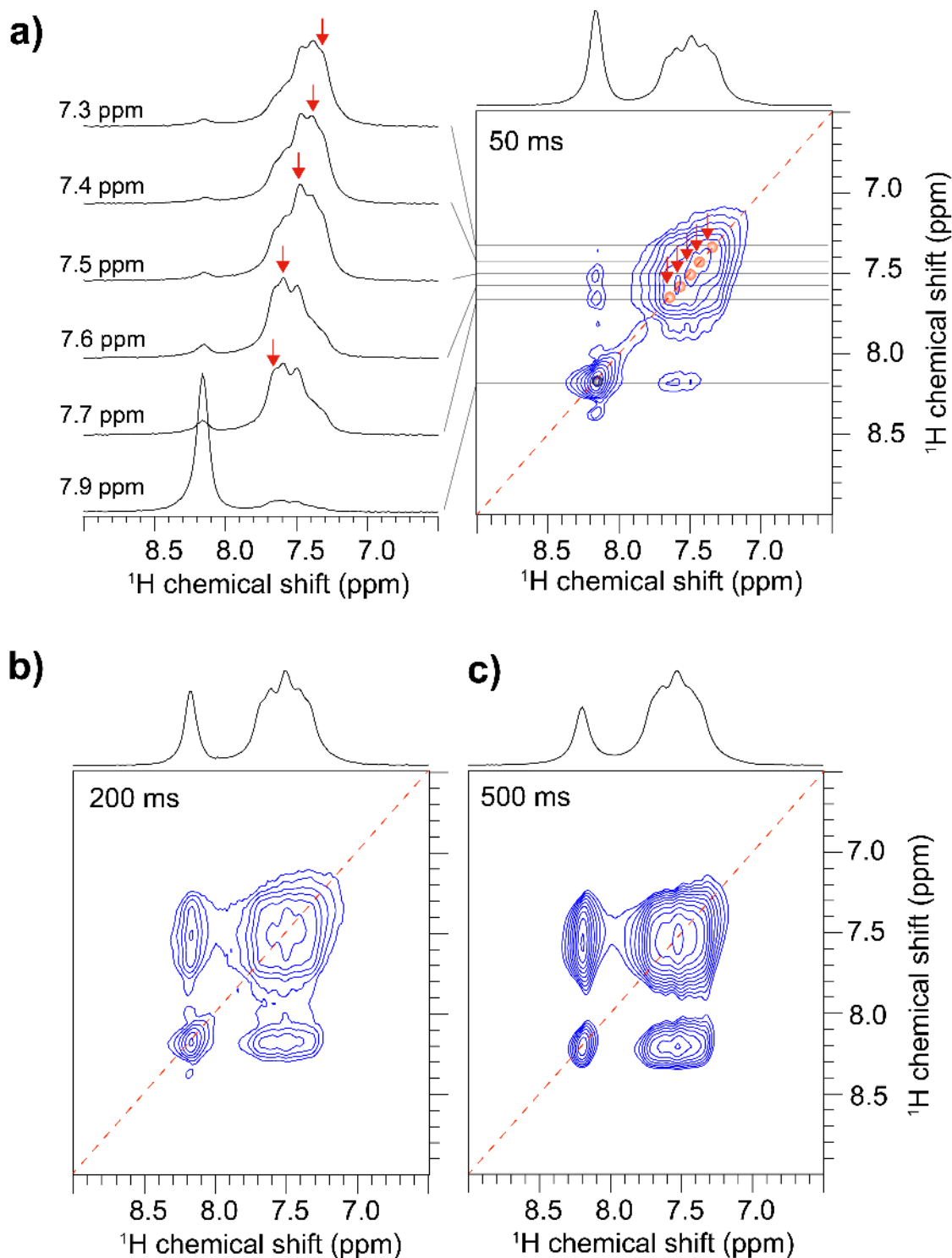
Figure S8: Solid-state (a) 2D ^1H-^1H spin-diffusion (SD) NMR spectrum acquired with 50 ms of mixing time together with the line-cut NMR spectra drawn at different chemical shifts as indicated. Identical 2D NMR spectra acquired with (b) 200 ms and (c) 500 ms of spin diffusion mixing times. All spectra were acquired at 18.8 T (^1H = 800.1 MHz) with 55 kHz MAS and at room temperature.
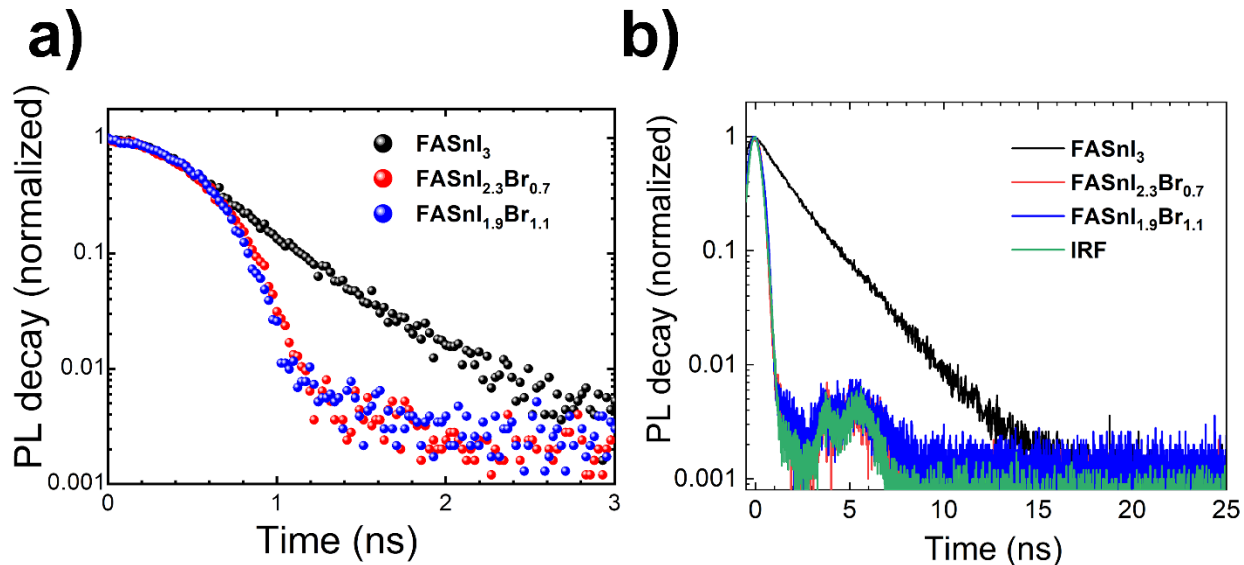
Figure S9: Time resolved photoluminescence a) for selected thin film samples for which PL intensity was observed and b) time resolved photoluminescence with the instrument response function plotted. Note that due to instrumental limitations at low lifetimes, the lifetime cannot be well resolved against the instrument response function (IRF) due to its width. The decay fitting does, however, give an approximation to the lifetime for the as synthesized thin film samples.
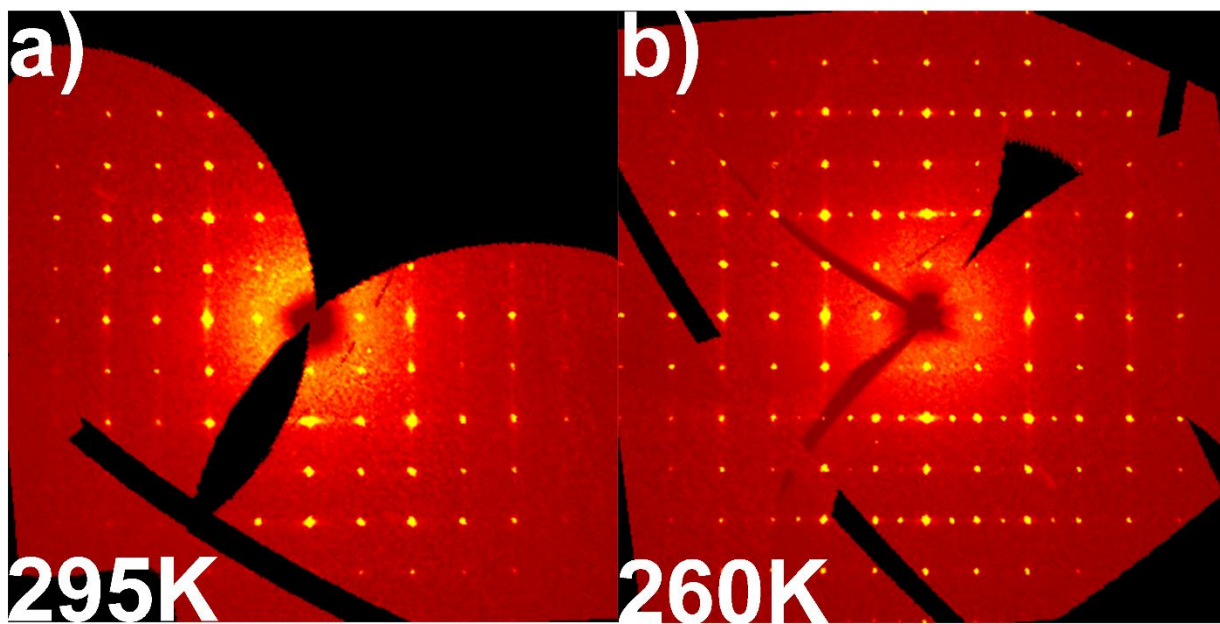
Figure S10: Precession images of reciprocal space for $FASnI_{0.4}Br_{2.6}$ at a) 295K and b) 260K. Data was collected on the same crystal to highlight the change in reflection conditions while leaving all other parameters constant. The presence of additional reflections at ½ *hkl* indicies at 260K provide evidence for this structural transition.

Figure S11: Light illumination of the related thin films was performed under 5000k white LED source (EverWatt, EW-HB-06-V-150W) with 100mW/cm^2 intensity in a nitrogen-filled glovebox. The samples were then taken out of the glovebox for measurement after 1-3-6-24 hours of illumination.

Figure S12: Sample holders containing FASnBr$_3$ (left) and FASnI$_3$ (right) prepared for Raman spectroscopy. The holders are quartz glass with glass wool inserted to beter compact the sample with epoxy being used to seal the narrow (~1 mm) width opening.
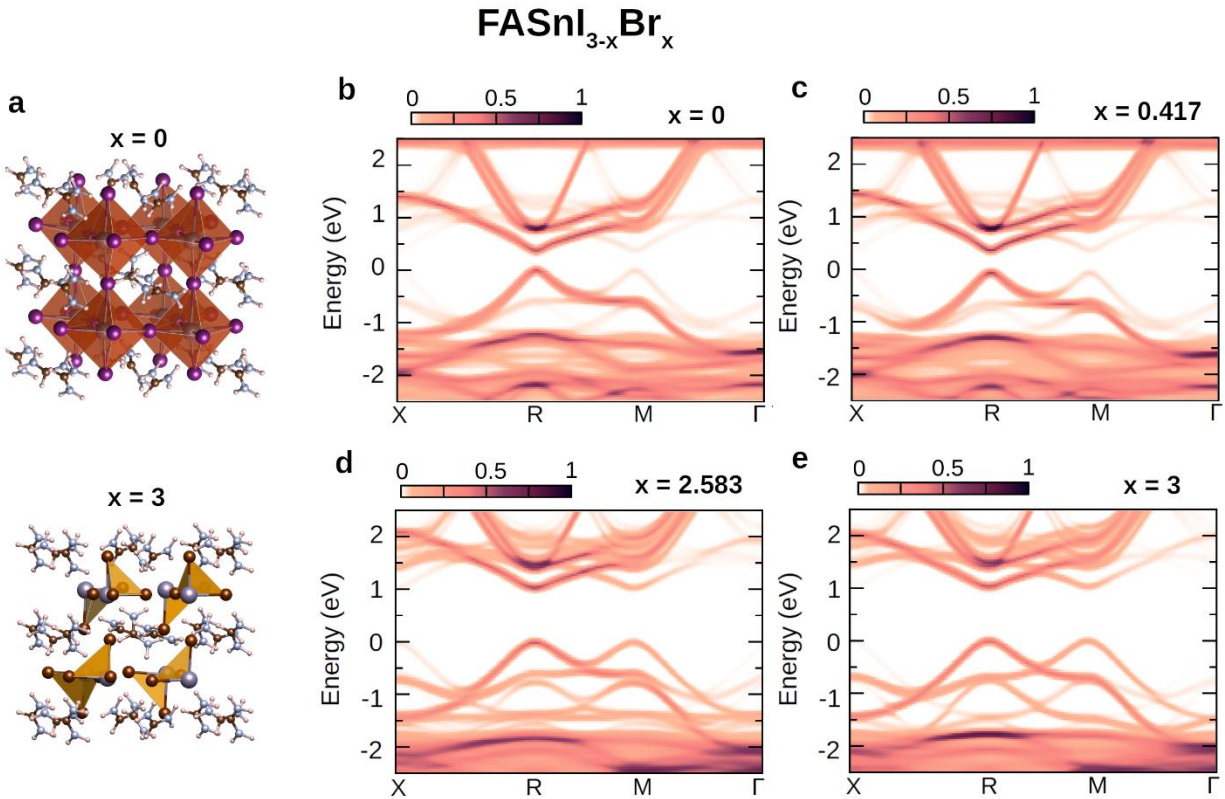
FASnI$_{3-x}$Br$_x$

Figure S13: Electron spectral functions of FASnI$_{3-x}$Br$_x$. (a) DFT optimized structures of cubic FASnI$_3$ ($x = 0$) and FASnBr$_3$ ($x = 3$) accounting for local disorder (polymorphism).[3, 4] (b-e) DFT electron spectral functions (color map) of FASnI$_{3-x}$Br$_x$ for $x = 0$ (b), $x = 0.417$ (c), $x = 2.583$ (d), and $x = 3$ (e) calculated using band structure unfolding[5, 6] and the PBEsol approximation.

Note S1: In Fig. S13a, we report the calculated structures of FASnI$_3$ (top) and FASnBr$_3$ (bottom). With respect to their idealized Pm$\overline{3}$m structures, we found energy stabilization of 87.3 meV/f.u. and 124.8 meV/f.u. for the distorted FASnI$_3$ and FASnBr$_3$, respectively, i.e. accounting for random local disorder for both, which leads to the expression of lone pairs (on average) for the latter. Figure S13b reports the calculated electron spectral function (color map) of cubic FASnI$_3$ which exhibits a band gap at the R point of 0.38 eV. Increasing the Br content in FASnI$_{3-x}$Br$_x$ further opens the band gap as shown in Figures S13c-e. In particular, our calculations for x = 0.417, x = 2.583, and $x = 3$ yield a direct band gap at the R point of 0.430, 1.043, and 1.039 eV, respectively. We observe that, while the typical pattern is to raise the band gap with an increase in the Br content, the slightly greater band gap for $x = 2.583$ compared to $x = 3$ can be attributed to the larger lattice constant when $x = 2.583$. We note that our calculations are performed at the DFT level and thus underestimation of all the band gaps is to be expected. A correction of around 1 eV due to the use

of a higher-level correlation functional has been reported previously.[3] Interestingly, raising the Br content also leads to the increase in the spectral weight (occupation probability) at the M point [see for example Fig. S13e]. The new states at the M point are replicas of the states at the R point emerging due to symmetry reduction of $FASnI_{3-x}Br_x$ upon Br substitution. The state at the M point is absent in the electron spectral function of the idealized $Pm\overline{3}m$ $FASnBr_3$ (Figure 13a), highlighting that its origin is the symmetry reduction induced by the stereochemical expression of Sn-5s lone pairs. Furthermore, Br substitution causes the enhancement of energy smearing and the increase of the effective masses.
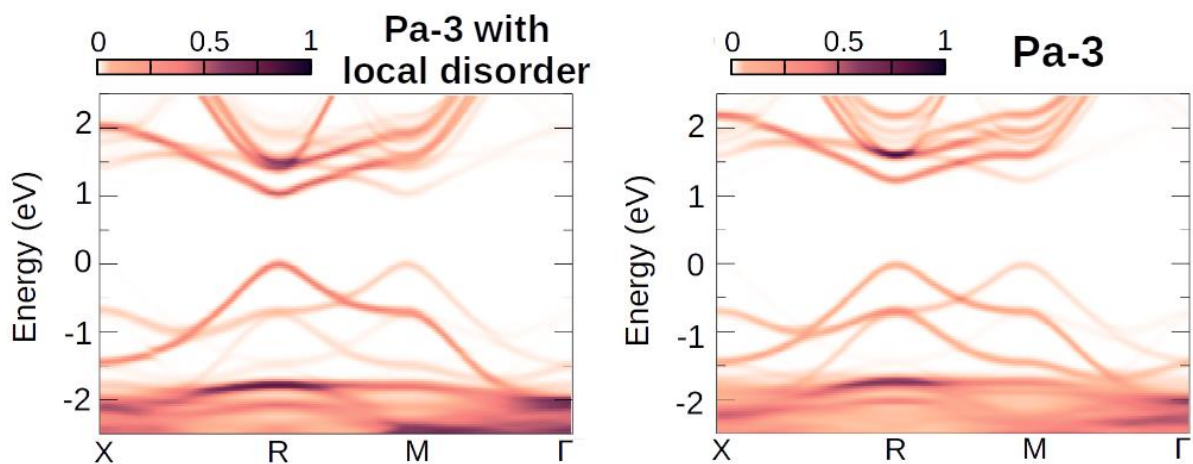
Figure S14: Effect of local disorder on the electronic band structure of FASnBr$_3$. DFT electron spectral functions (color map) of FASnBr$_3$ considering cubic P$a\overline{3}$ space group, calculated using band structure unfolding[5, 6] and the PBEsol approximation (left) accounting for local disorder (polymorphism)[3, 4] and (right) without, i.e. using experimental crystallographic data for the inorganic atomic positions.
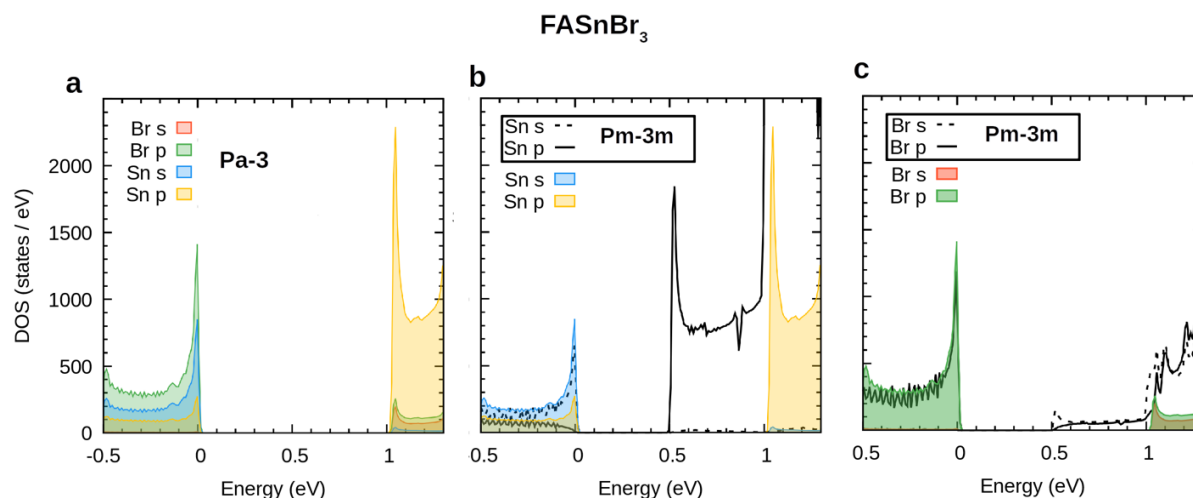
Figure S15: Projected density of states of FASnBr₃. (a) Projected density of states (PDOS) showing the contribution of Br-4s (red), Br-4p (green), Sn-5s (blue), and Sn-5p (yellow) orbitals to the formation of the band edges of the distorted (P$a\overline{3}$) FASnBr₃. (b) Projected density of states showing the contribution of Sn-5s (black dashed line) and Sn-5p (black solid line) orbitals to the formation of the band edges of the idealized P$m\overline{3}m$ FASnBr₃. (c) Projected density of states showing the contribution of Br-4s (black dashed line) and Br-4p (black solid line) orbitals to the formation of the band edges of the idealized P$m\overline{3}m$ FASnBr₃. In (b) and (c) the corresponding PDOS calculated for the distorted FASnBr₃ (colored) is shown for comparison. The energy axes are adjusted so that the VBM is set at zero energy.

Note S2: Figure S15a shows the projected density of states (PDOS) calculated for FASnBr₃ in the cubic P$a\overline{3}$ space group. As expected, the density of states varies proportionally to the square root of energy consistent with the parabolic band approximation. In comparison to the PDOS of the idealized P$m\overline{3}m$ FASnBr₃ (black lines in Figures S15b and c), the contributions from the Sn-5s and Br-4p orbitals to the valence band remain nearly unchanged, while the contribution from Sn-5p orbitals is significantly enhanced. Regarding the conduction band, the dominant contribution remains from the Sn-5p orbitals with small contributions arising from the Br-4p, Sn-5s, and Br-4s orbitals. From the comparison of the PDOS in Figs. S15b and c, it is also apparent that the structural distortion induced by the stereochemical expression of the Sn-5s lone pair leads to the energy broadening of the density of states.

Table S1: Selected Crystallographic information and refinement statistics for representative $FASnI_{3-x}Br_x$ ($x = 0 - 3$) compositions. $FASnI_3$ and $FASnBr_3$ were synthesized and measured independently of previous research efforts.

Formula	$FASnI_3$	$FASnI_{2.6}Br_{0.4}$	$FASnI_{2.3}Br_{0.7}$	$FASnI_{2.1}Br_{0.9}$	$FASnI_{1.9}Br_{1.1}$	$FASnI_{1.1}Br_{1.9}$	$FASnI_{0.7}Br_{2.3}$	$FASnI_{0.4}Br_{2.6}$	$FASnI_{0.1}Br_{2.9}$	$FASnBr_3$
Formula weight	525.41	518.74	508.41	495.72	488.67	452.02	432.28	418.19	402.62	398.45
Temperature (K)	295	295	295	295	295	295	295	295	300	290
Wavelength (Å)	0.71073	0.71073	0.71073	0.71073	0.71073	0.71073	0.71073	0.71073	0.56083	0.71073
Crystal system						Cubic				
Space group	$Pm\overline{3}m$	$Pm\overline{3}m$	$Pm\overline{3}m$	$Pm\overline{3}m$	$Pm\overline{3}m$	$Pm\overline{3}m$	$Pm\overline{3}m$	$Pm\overline{3}m$	$Pa\overline{3}$	$Pa\overline{3}$
$a/b/c$ (Å)	6.3064(3)	6.3099(2)	6.2824(2)	6.2525(5)	6.2449(1)	6.1354(2)	6.0915(2)	6.0443(2)	12.0637(15)	12.0303(5)
Volume (Å³)	250.81(4)	251.23(3)	247.96(2)	244.43(6)	243.54(1)	230.96(6)	226.03(2)	220.82(2)	1755.7(7)	1741.1(2)
Z	1	1	1	1	1	1	1	1	8	8
ρ_{calc} (g/cm³)	3.479	3.429	3.405	3.368	3.332	3.250	3.176	3.145	3.046	3.040
Absorption coefficient (mm⁻¹)	11.695	12.080	12.441	12.871	13.058	14.537	15.275	15.944	8.707	16.615
Independent reflections	91 [R_{int} = 0.0375]	172 [R_{int} = 0.0117]	166 [R_{int} = 0.0087]	103 [R_{int} = 0.0314]	160 [R_{int} = 0.0183]	68 [R_{int} = 0.0750]	95 [R_{int} = 0.0136]	113 [R_{int} = 0.0132]	688 [R_{int} = 0.0487]	641 [R_{int} = 0.0716]
Completeness	100% (θ = 25.242°)	100% (θ = 25.242°)	100% (θ = 25.242°)	100% (θ = 25.242°)	100% (θ = 25.242°)	100% (θ = 25.190°)	100% (θ = 25.242°)	100% (θ = 25.242)	100% (θ = 19.664)	100% (θ = 25.242)
Data / restraints / parameters	91 / 1 / 8	172 / 1 / 10	166 / 1 / 10	103 / 1 / 9	160 / 1 / 10	68 / 1 / 9	95 / 1 / 10	113 / 1 / 10	688 / 2 / 25	641 / 2 / 24
Goodness-of-fit	1.550	1.232	1.207	1.430	1.198	1.413	1.117	1.204	1.273	1.052
Final R indices [I > 2σ(I)]	R_{obs} = 0.0435, wR_{obs} = 0.01248	R_{obs} = 0.0231, wR_{obs} = 0.0766	R_{obs} = 0.0239, wR_{obs} = 0.0877	R_{obs} = 0.0429, wR_{obs} = 0.1006	R_{obs} = 0.0231, wR_{obs} = 0.0846	R_{obs} = 0.0292, wR_{obs} = 0.0950	R_{obs} = 0.0317, wR_{obs} = 0.1092	R_{obs} = 0.0479, wR_{obs} = 0.1540	R_{obs} = 0.0585, wR_{obs} = 0.1451	R_{obs} = 0.0419, wR_{obs} = 0.1011
R indices [all data]	R_{all} = 0.0556, wR_{all} = 0.1254	R_{all} = 0.0258, wR_{all} = 0.0786	R_{all} = 0.0273, wR_{all} = 0.0908	R_{all} = 0.0443, wR_{all} = 0.1070	R_{all} = 0.0247, wR_{all} = 0.0859	R_{all} = 0.0292, wR_{all} = 0.0950	R_{all} = 0.0317, wR_{all} = 0.1092	R_{all} = 0.0479, wR_{all} = 0.1540	R_{all} = 0.0849, wR_{all} = 0.1619	R_{all} = 0.0679, wR_{all} = 0.1139
Largest diff. peak/hole (e·Å⁻³)	0.869/-1.372	0.680/-0.836	1.229/-1.299	0.656/-0.944	0.814/-0.828	0.716/-0.4	0.636/-0.610	0.747/-1.260	0.952/-0.695	0.799/-0.643

$R = \Sigma||F_o|-|F_c|| / \Sigma|F_o|$, $wR = \{\Sigma[w(|F_o|^2 - |F_c|^2)^2] / \Sigma[w(|F_o|^4)]\}d^{1/2}$ and $w=1/[\sigma^2(Fo^2)+(0.0163P)^2+1.6916P]$ where $P=(Fo^2+2Fc^2)/3$

Table S2: Atomic Coordinates ($\times 10^4$) and equivalent isotropic displacement parameters ($\text{Å}^2 \times 10^3$) for the compositions in the $FASnI_{3-x}Br_x$ ($x = 0 - 3$) substitution range with standard deviations in parenthesis. The temperature of the data collection is also listed.

Label	x	y	z	Occupancy	U_{eq}*
FASnI$_3$ (295K)					
Sn	5000	5000	5000	1	42(1)
I	0	5000	5000	1	81(1)
C	0	0	0	1	110(20)
N	2170(30)	0	0	0.3334	170(40)
FASnI$_{2.6}$Br$_{0.4}$ (295K)					
Sn	5000	5000	5000	1	44(1)
I	0	5000	5000	0.854(17)	82(1)
Br	0	5000	5000	0.146(17)	82(1)
C	0	0	0	1	150(20)
N	2180(30)	0	0	0.3334	141(12)
FASnI$_{2.3}$Br$_{0.7}$ (295K)					
Sn	5000	5000	5000	1	48(1)
I	0	5000	5000	0.78(2)	87(1)
Br	0	5000	5000	0.22(2)	87(1)
C	0	0	0	1	220(40)
N	2100(30)	0	0	0.3334	185(14)
FASnI$_{2.1}$Br$_{0.9}$ (295K)					
Sn	5000	5000	5000	1	52(1)
I	0	5000	5000	0.69(3)	92(1)
Br	0	5000	5000	0.31(3)	92(1)
C	0	0	0	1	130(20)
N	2150(30)	0	0	0.3334	160(20)
FASnI$_{1.9}$Br$_{1.1}$ (295K)					
Sn	5000	5000	5000	1	56(1)
I	0	5000	5000	0.640(19)	98(1)
Br	0	5000	5000	0.360(19)	98(1)
C	0	0	0	1	180(20)
N	2130(30)	0	0	0.3334	203(19)
FASnI$_{1.1}$Br$_{1.9}$ (295K)					
Sn	5000	5000	5000	1	66(1)
I	0	5000	5000	0.38(3)	120(2)
Br	0	5000	5000	0.62(3)	120(2)
C	0	0	0	1	190(30)
N	2220(30)	0	0	0.3334	210(40)
FASnI$_{0.7}$Br$_{2.3}$ (295K)					
Sn	5000	5000	5000	1	66(1)
I	0	5000	5000	0.25(3)	131(2)
Br	0	5000	5000	0.75(3)	131(2)
C	0	0	0	1	190(40)
N	2240(30)	0	0	0.3334	210(40)
FASnI$_{0.4}$Br$_{2.6}$ (295K)					

Sn	5000	5000	5000	1	66(1)
I	0	5000	5000	0.13(4)	141(2)
Br	0	5000	5000	0.87(4)	141(2)
C	0	0	0	1	170(40)
N	2290(30)	0	0	0.3334	250(80)
$FASnI_{2.6}Br_{0.4}$ (260K)					
Sn	2529(1)	2529(1)	2529(1)	1	58(1)
Br	2550(5)	2572(5)	218(5)	0.842(11)	107(2)
I	2500(20)	2423(19)	-241(14)	0.158(11)	107(2)
C1	5000	0	0	1	150(190)
C2	0	0	0	1	200(200)
N1	4400(70)	-920(80)	390(120)	0.3333	250(50)
N2	-210(70)	830(100)	790(100)	0.3333	330(90)
$FASnI_{0.1}Br_{2.9}$ (300K)					
Sn	2430(1)	7430(1)	7570(1)	1	50(1)
Br	4695(2)	7397(3)	7613(4)	0.970(10)	93(1)
I	4790(40)	7680(60)	7140(80)	0.030(10)	93(1)
C1	5000	5000	5000	1	150(30)
C2	0	0	0	1	170(30)
N1	653(9)	653(9)	653(9)	1	360(40)
N2	4910(120)	5320(110)	3900(40)	0.3333	310(70)
$FASnBr_3$ (290K)					
Sn	7597(1)	2403(1)	7403(1)	1	47(1)
Br	5340(1)	2384(1)	7370(1)	1	90(1)
C1	5000	5000	5000	1	156(18)
C2	5000	0	5000	1	160(20)
N1	6114(16)	4940(30)	4900(40)	0.3333	200(20)
N2	9028(16)	5340(30)	4600(30)	0.3333	125(11)

[*]U_{eq} is defined as one third of the trace of the orthogonalized U_{ij} tensor.

Table S3: Selected Anisotropic displacement parameters ($Å^2 \times 10^3$) for compounds in the FASnI$_{3-x}$Br$_x$ ($x = 0 - 3$) family, with estimated standard deviations in parenthesis. The temperature of the data collection is also listed.

Label	U_{11}	U_{22}	U_{33}	U_{12}	U_{13}	U_{23}
			FASnI$_3$ (295K)			
Sn	42(1)	42(1)	42(1)	0	0	0
I	36(1)	104(2)	104(2)	0	0	0
			FASnI$_{2.6}$Br$_{0.4}$ (295K)			
Sn	44(1)	44(1)	44(1)	0	0	0
I	37(1)	104(1)	104(1)	0	0	0
Br	37(1)	104(1)	104(1)	0	0	0
			FASnI$_{2.3}$Br$_{0.7}$ (295K)			
Sn	48(1)	48(1)	48(1)	0	0	0
I	42(1)	109(1)	109(1)	0	0	0
Br	42(1)	109(1)	109(1)	0	0	0
			FASnI$_{2.1}$Br$_{0.9}$ (295K)			
Sn	52(1)	52(1)	52(1)	0	0	0
I	52(1)	113(2)	113(2)	0	0	0
Br	52(1)	113(2)	113(2)	0	0	0
			FASnI$_{1.9}$Br$_{1.1}$ (295K)			
Sn	56(1)	56(1)	56(1)	0	0	0
I	56(1)	119(1)	119(1)	0	0	0
Br	56(1)	119(1)	119(1)	0	0	0
			FASnI$_{1.1}$Br$_{1.9}$ (295K)			
Sn	66(1)	66(1)	66(1)	0	0	0
I	94(2)	133(2)	133(2)	0	0	0
Br	94(2)	133(2)	133(2)	0	0	0
			FASnI$_{0.7}$Br$_{2.3}$ (295K)			
Sn	66(1)	66(1)	66(1)	0	0	0
I	119(2)	137(2)	137(2)	0	0	0
Br	119(2)	137(2)	137(2)	0	0	0
			FASnI$_{0.4}$Br$_{2.6}$ (295K)			
Sn	66(1)	66(1)	66(1)	0	0	0
I	148(4)	138(3)	138(3)	0	0	0
Br	148(4)	138(3)	138(3)	0	0	0
			FASnI$_{0.4}$Br$_{2.6}$ (260K)			
Sn	58(1)	58(1)	58(1)	1(1)	1(1)	1(1)
Br	130(2)	126(3)	64(3)	-7(7)	-5(3)	-7(3)
I	130(2)	126(3)	64(3)	-7(7)	-5(3)	-7(3)
			FASnI$_{0.1}$Br$_{2.9}$ (300K)			
Sn	50(1)	50(1)	50(1)	0(1)	0(1)	0(1)
I	52(1)	112(2)	114(2)	-5(1)	-4(1)	12(2)
Br	52(1)	112(2)	114(2)	-5(1)	-4(1)	12(2)
			FASnBr$_3$ (290K)			
Sn	47(1)	47(1)	47(1)	1(1)	1(1)	-1(1)
Br	46(1)	106(1)	119(1)	5(1)	-2(1)	-8(1)

The anisotropic displacement factor exponent takes the form: $-2\pi^2[h^2a^{*2}U_{11} + ... + 2hka^*b^*U_{12}]$.

Table S4: Selected interatomic distances (Å) for compounds in the FASnI$_{3-x}$Br$_x$ ($x = 0 - 3$) family with estimated standard deviations in parenthesis. The temperature of each data collection is also listed.

Label	Distance
FASnI$_3$ (295K)	
Sn-I	3.15320(15)
FASnI$_{2.6}$Br$_{0.4}$ (295K)	
Sn-I/Br	3.15495(10)
FASnI$_{2.3}$Br$_{0.7}$ (295K)	
Sn-I/Br	3.14120(10)
FASnI$_{2.1}$Br$_{0.9}$ (295K	
Sn-I/Br	3.1263(3)
FASnI$_{1.9}$Br$_{1.1}$ (295K)	
Sn-I/Br	3.12245(5)
FASnI$_{1.1}$Br$_{1.9}$ (295K)	
Sn-I/Br	3.06770(10)
FASnI$_{0.7}$Br$_{2.3}$ (295K)	
Sn-I/Br	3.04575(10)
FASnI$_{0.4}$Br$_{2.6}$ (295K)	
Sn-I/Br	3.02215(10)
FASnI$_{0.4}$Br$_{2.6}$ (295K)	
Sn-I	2.681(17)
Sn-I	3.332(17)
Sn-Br	2.778(7)
Sn-Br	3.234(7)
FASnI$_{0.1}$Br$_{2.9}$ (300K)	
Sn-I	2.91(6)
Sn-I	3.22(5)
Sn-Br	2.733(2)
Sn-Br	3.307(3)
FASnBr$_3$ (290K)	
Sn-Br	2.7164(10)

Table S5: Average* atomic percentages based on scanning electron microscopy coupled with energy dispersive X-ray spectroscopy (SEM-EDS) with estimated standard deviations. The composition was then estimated normalizing the atomic percentages to that of Sn.

Compound	Sn (At. %)	I (At. %)	Br (At%)	Average Composition
$FASnI_3$	25.6 ± 046	74.34 ± 0.45	-------------	$FASnI_{2.91}$
$FASnI_{2.6}Br_{0.4}$	24.3 ± 0.96	69.72 ± 0.50	5.98 ± 0.89	$FASnI_{2.76}Br_{0.24}$
$FASnI_{2.3}Br_{0.7}$	25.2 ± 1.32	61.97 ± 3.6	12.8 ± 2.85	$FASnI_{2.48}Br_{0.51}$
$FASnI_{2.1}Br_{0.9}$	26.3 ± 0.45	45.8 ± 0.90	27.8 ± 0.81	$FASnI_{1.74}Br_{1.06}$
$FASnI_{1.9}Br_{1.1}$	25.7 ± 0.41	46 ± 1.1	28 ± 1.4	$FASnI_{1.80}Br_{1.10}$
$FASnI_{1.1}Br_{1.9}$	26.1 ± 0.99	30.9 ± 0.30	43 ± 1.3	$FASnI_{1.18}Br_{1.65}$
$FASnI_{0.7}Br_{2.3}$	26 ± 1.8	13.6 ± 0.44	61 ± 1.9	$FASnI_{0.53}Br_{2.3}$
$FASnI_{0.4}Br_{2.6}$	26 ± 2.3	9.6 ± 0.95	64 ± 3.3	$FASnI_{0.36}Br_{2.43}$
$FASnI_{0.1}Br_{2.9}$	24 ± 1.4	4.0 ± 0.24	72 ± 1.6	$FASnI_{0.16}Br_{2.96}$
$FASnBr_3$	26.2 ± 0.64	-------------	73.8 ± 0.64	$FASnBr_{2.82}$

*The average is compiled across 3-5 independent spectra

Table S6: Crystallographic information and refinement parameters for $(NH_4)_2SnBr_6$ and SnI_4 impurity phases.

Formula	$(NH_4)_2SnBr_6$	SnI_4
Formula weight (g/mol)	626.17	626.29
Temperature (K)	295	295
Wavelength (Å)	0.71073	0.71073
Crystal system	Cubic	Cubic
Space group	$Fm\bar{3}m$	$Pa\bar{3}$
$a/b/c$ (Å)	10.64150(10)	12.2493(4)
Volume ($Å^3$)	1205.06(3)	1837.95
Z	4	8
ρ_{calc} (g/cm^3)	3.451	4.527
μ (mm^{-1})	21.957	16.118
Independent reflections	206 [R_{int} = 0.0671]	905 [R_{int} = 0.0131]
Completeness to θ = 25.242°	100%	100%
Data / restraints / parameters	206 / 0 / 6	905 / 0 / 16
Goodness-of-fit	1.200	1.084
Final R indices [$I > 2\sigma(I)$]	R_{obs} = 0.0258, wR_{obs} = 0.0687	R_{obs} = 0.0266, wR_{obs} = 0.0568
R indices [all data]	R_{all} = 0.0310, wR_{all} = 0.0702	R_{all} = 0.0436, wR_{all} = 0.0618
Largest diff. peak and hole	0.832 and -0.567 e·Å^{-3}	0.505 and -0.560 e·Å^{-3}

$R = \Sigma||F_o|-|F_c|| / \Sigma|F_o|$, $wR = \{\Sigma[w(|F_o|^2 - |F_c|^2)^2] / \Sigma[w(|F_o|^4)]\}^{1/2}$ and $=1/[\sigma^2(Fo^2)+(0.0167P)^2+2.7543P]$ where $P=(Fo^2+2Fc^2)/3$

Note S3: The crystallographic refinement and unit cell parameters compare well with previous reports of these two compounds in the literature.[7, 8]

Table S7: Crystallographic information and refinement parameters for FASnI$_{0.4}$Br$_{2.6}$ at 260K with estimated standard deviations in parenthesis

Refined Formula	FASnI$_{0.5}$Br$_{2.5}$*
Formula weight (g/mol)	420.7
Temperature (K)	260
Wavelength (Å)	0.56083
Crystal system	Cubic
Space group	$Pa\overline{3}$
$a/b/c$ (Å)	12.018(4)
Volume (Å^3)	1735.9(10)
Z	8
ρ_{calc} (g/cm^3)	3.2197
μ (mm^{-1})	8.624
Independent reflections	302 [R$_{int}$ = 0.0931]
Completeness to θ = 26.48°	98
Data / restraints / parameters	302 / 2 / 28
Goodness-of-fit	1.59
Final R indices [I > 2σ(I)]	R$_{obs}$ = 0.0544, wR$_{obs}$ = 0.1039
R indices [all data]	R$_{all}$ = 0.0932, wR$_{all}$ = 0.1193
Largest diff. peak and hole	1.28 and -0.64 e·Å^{-3}

$R = \Sigma||F_o|-|F_c|| / \Sigma|F_o|$, $wR = \{\Sigma[w(|F_o|^2 - |F_c|^2)^2] / \Sigma[w(|F_o|^4)]\}^{1/2}$ and $=1/[\sigma^2(Fo^2)+(0.0167P)^2+2.7543P]$ where $P=(Fo^2+2Fc^2)/3$

* The refined formula differs from the true formula determined based on room temperature single crystal diffraction on the same crystal. For simplicity the formula FASnI$_{0.4}$Br$_{2.6}$ is adopted in the discussion of the material.

Table S8: PL peak position and peak shift under 1 sun light illumination

	0 Hours	1 Hour	3 Hours	6 Hours	24 Hours
FASnI$_3$ Peak Position (nm)	875	869	861	859	855
FASnI$_3$ Peak Shift (nm)	---------	6	14	16	20
FASnI$_{2.6}$Br$_{0.4}$ Peak Position (nm)	841	830	830	828	823
FASnI$_{2.6}$Br$_{0.4}$ Peak Shift (nm)	---------	11	11	13	18
FASnI$_{2.3}$Br$_{0.7}$ Peak Position (nm)	788	785	790	790	790
FASnI$_{2.3}$Br$_{0.7}$ Peak Shift (nm)	---------	3	2	2	2
FASnI$_{1.9}$I$_{1.1}$ Peak Position	732	734	741	746	750
FASnI$_{1.9}$Br$_{1.1}$ Peak Shift (nm)	---------	2	9	14	18

Table S9: The Full Width at Half Maximum (FWHM) of PL spectra for $FASnI_{2.3}Br_{0.7}$ thin film. by increasing the illumination time. The FWHM is increased under longer illumination time.

Illumination time at 1sun (hours)	FWHM of PL spectra for $FASnI_{2.3}Br_{0.7}$ thin films (nm)
0	62
1	70
3	75
6	79
24	86

References:

(1) Kortüm, G.; Braun, W.; Herzog, G. Principles and Techniques of Diffuse-Reflectance Spectroscopy. In *Angewandte Chemie International Edition in English*, 1963; Vol. 2, pp 333-341.
(2) Farrow, C. L.; Juhas, P.; Liu, J. W.; Bryndin, D.; Božin, E. S.; Bloch, J.; Proffen, T.; Billinge, S. J. L. PDFfit2 and PDFgui: computer programs for studying nanostructure in crystals. *Journal of Physics: Condensed Matter* **2007**, *19* (33), 335219. DOI: 10.1088/0953-8984/19/33/335219.
(3) Zacharias, M.; Volonakis, G.; Giustino, F.; Even, J. Anharmonic electron-phonon coupling in ultrasoft and locally disordered perovskites. *npj Computational Materials* **2023**, *9* (1), 153. DOI: 10.1038/s41524-023-01089-2.
(4) Zhao, X.-G.; Dalpian, G. M.; Wang, Z.; Zunger, A. Polymorphous nature of cubic halide perovskites. *Physical Review B* **2020**, *101* (15), 155137. DOI: 10.1103/PhysRevB.101.155137.
(5) Popescu, V.; Zunger, A. Extracting E versus k effective band structure from supercell calculations on alloys and impurities. *Physical Review B* **2012**, *85* (8), 085201. DOI: 10.1103/PhysRevB.85.085201.
(6) Zacharias, M.; Giustino, F. Theory of the special displacement method for electronic structure calculations at finite temperature. *Physical Review Research* **2020**, *2* (1), 013357. DOI: 10.1103/PhysRevResearch.2.013357.
(7) Ketelaar, J. A. A.; Rietdijk, A. A.; Van Staveren, C. H. Die Kristallstruktur von Ammonium-, Kalium-, Rubidium- und Cäsiumstannibromid. *Recueil des Travaux Chimiques des Pays-Bas* **1937**, *56* (9), 907-908. DOI: 10.1002/recl.19370560913.
(8) Reuter, H.; Pawlak, R. Zinnhalogenverbindungen. II. Die Molekül- und Kristallstrukturen von Zinn(IV)-bromid und -iodid. *Zeitschrift für Kristallographie - Crystalline Materials* **2001**, *216* (1), 34-38. DOI: doi:10.1524/zkri.216.1.34.18992 (acccessed 2023-06-07).